Università degli Studi di Napoli "FedericoII"

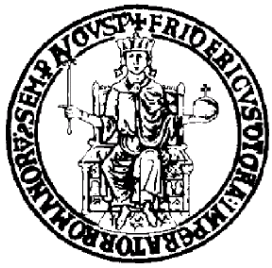

Dottorato di Ricerca in
Tecnologie Innovative per Materiali,
Sensori ed Imaging
- 26° ciclo -

Development of a Carbon Nanotubes Based Photodetector

Marco Cilmo

Coordinatore:
Prof. Antonio Cassinese

Relatori:
Prof. Giovanni La Rana
Dr. Giuseppe Osteria

Anno Accademico 2013-14

Contents

Introduction

The aim of my research activity has been the realization, characterization and modeling of a new generation of detectors based on Carbon NanoTubes (CNTs) for their application in Very High Energy Cosmic Ray Physics and in Cherenkov radiation detection for gamma-ray astronomy. My activity has been carried out in the framework of the following experiments: PARIDE (Pixel Array for Radiation Imaging DEtector), the Pierre Auger experiment and CTA (Cherenkov Telescope Array).

The Pierre Auger Observatory is a hybrid detector for ultra-high energy cosmic rays. It combines a surface array to measure secondary particles at ground level together with a fluorescence detector to measure the development of air showers in the atmosphere above the array. The fluorescence detector comprises 27 large telescopes specialized for measuring the nitrogen fluorescence caused by charged particles of cosmic ray air showers.

CTA is the next generation of very high energy gamma-ray telescope array, which is currently in the development phase. An array of many tens of telescopes will allow the detection of gamma-ray induced cascades over a large area on the ground, increasing the number of detected gamma rays dramatically, while at the same time providing a much larger number of views of each cascade.

For both experiments I investigated the possibility to enhance the detection quantum efficiency of fluorescence and Cherenkov light detection by means of a new photodetector based on Carbon Nanotubes grown on doped silicon substrates, that is the PARIDE target. Among the great variety of particle detectors for physics experiments, a great importance is attributed to radiation detectors for their capability to detect light emitted in particle interaction with matter. Cherenkov light, fluorescence radiation and scintillation signals must be detected with great accuracy for nature and energy particle assignment. Detectors with pixelated surface allow position or imaging information. Linearity and analog signal reconstruction allow information on energy loss in matter. Good time resolution is needed for time of flight or trigger purpose. High quantum efficiency is mandatory in all the wavelength range and field of operation, from Ultraviolet (UV) to near infrared (IR) wavelength region. Coating, aging and radiation robustness play a fundamental role in the apparatus operation and management. Accurate signal readout and front-end electronics complete the detector set-up and contribute to the measurement performances. The UV wavelength range from 300 to 400 nm is the most investigated for its large field of application

and its importance for high energy particle detection.

There are different ways of defining the structure of carbon nanotubes. One option is to consider that CNTs may be obtained by rolling a graphene sheet in a specific direction, maintaining the circumference of the cross-section. Since the structure of the CNTs is closely related to graphene, CNTs are frequently labeled in terms of graphene lattice vectors. In addition, the reference to graphene allows the theoretical derivation of many CNTs properties. Moreover, CNTs can be categorized in the following way: Single-wall Nanotubes (SWCNT), and Multi-Wall Nanotubes (MWCNT). Multi-wall nanotubes appear in the form of a coaxial assembly of SWCNT similar to a coaxial cable. MWCNT are easier to produce in high volume quantities than SWCNT. However, the structure of MWCNT is less understood because of its greater complexity and variety. Carbon nanotubes have been the subject of intensive research due to their intriguing electronic and structural properties, and have demonstrated great potential for future nano-electronic devices, and so much work has been done to fabricate and understand electronic devices made with CNTs. An area of research that is just moving its first steps is that of opto-electronics with CNTs, in particular optical-to-electrical transducers based on CNTs.

The research activity on the new detector started some years ago within the INFN program GINT (Gruppo INFN per le Nanotecnologie). It was demonstrated that a MWCNTs film generates a photocurrent when irradiated. Starting from these experimental observations, a new photodetector based on MWCNTs has been developed within the successive INFN programs SinPhoNIA (Single Photon Nanotechnology Innovative Approach) and PARIDE.

During my activity I realized and improved an acquisition system for automated measurements, and I studied dozens of MWCNT-based detectors with different growth parameters with the aim to characterize their behaviour in function of MWCNTs characteristics. In this thesis I report on prototype light detectors based on large area layers of MWCNTs deposited by Chemical Vapour Deposition (CVD) at different temperatures: the first with nanostructures grown at 700°C, the second at 500°C, and the third with a coating layer. These two temperatures have been reported in order to show differences in the structure and the length of the resulting carbon nano-systems, and consequently the difference in the ability to generate a photocurrent in the range from near ultraviolet to infrared.

The thesis is organized into five chapters.

In Chapter 1 is presented an essential review on the basic properties of semiconductors and junctions. This chapter describes the p-n junction characteristics: the p-n junction is the building block of most semiconductor

devices, and its theory serves as the foundation of the physics of semiconductor devices. Chapter 1 also considers the heterojunction, that is a junction formed between two dissimilar semiconductors, this topic is related to the heterojunction created between nanotubes and silicon.

Chapter 2 is devoted to a study of various solid-state photodetectors.

Chapter 3 reports on the atomic and the electronic structure of CNTs, establishing the basic concepts, in particular the strong coupling between CNT electronic properties and their geometrical structure.

In chapter 4, the first part reports on the characteristics of the photodetectors fabricated using carbon nanostructures grown on a doped silicon substrates. The second part treats results obtained when an electrically conductive coating layer is applied to MWCNTs film to avoid the nanotube detachment from the silicon substrate and uniformly transmit the electric field to the entire active surface. In the third part a modeling and simulation study on carbon nanostructures/silicon heterojunction is presented.

Chapter 5 reports on a set of Samples with MWCNTs growth on substrates manufactured with different structures in order to obtaining an effect of charge multiplication inside the Silicon substrate.

Chapter 1

Physics and properties of Semiconductors

This chapter presents a summary and review of the basic physics and properties of solids, semiconductors and junctions. The informations presented here represent only a small cross section of the vast literature; only those subjects pertinent to the work presented in this thesis are included.

1.1 Solids

Matter consists of atoms. These may be isolated, as in the case of a dilute atomic gas, or they may interact with neighboring atoms to form molecules and matter in the liquid or solid state. The motion of constituents of matter follow the laws of quantum mechanics [1] [2].

An isolated hydrogen atom has a potential energy that derives from the Coulomb law of attraction between the proton and the electron. The solution of the Schrödinger equation leads to an infinite number of discrete energy levels. The computation of the energy levels of more complex atoms is difficult, because of the interactions among the electrons and the effects of electron spin. All atoms have discrete energy levels with energy differences that typically lie in the optical region (up to several eV). Organic dye molecules are large and complex. They may undergo electronic, vibrational, and rotational transitions so that they typically have many energy levels. The important point is that both isolated atoms and isolated molecules exhibit discrete energy levels. In the case of solids, the atoms, ions, or molecules lie in close proximity to each other (in the ideal case they join together into a periodic arrangement comprising a crystal lattice) and cannot be considered as simple collections of isolated atoms, but they must be treated as a many-body sys-

tem. The strength of the forces holding the atoms together in order to form a solid, has approximately the same magnitude as the forces that combine together atoms into molecules. Consequently, the energy levels of solids are determined not only by the potentials associated with individual atoms, but also by potentials associated with neighboring lattice atoms.

An individual atom in a collection of identical isolated atoms has an identical set of discrete energy levels. As these atoms are brought into proximity to form a solid, exchange interactions (that follow the requirements of quantum mechanics), along with the presence of fields of varying strengths from neighboring atoms, become increasingly important. The initially sharp energy levels associated with the valence electrons of isolated atoms gradually broaden into collections of numerous densely spaced energy levels that form energy bands. This process is illustrated in figure 1.1, where electron energy levels are illustrated schematically for two isolated atoms (a), for a molecule containing two such atoms (b), and for a rudimentary one-dimensional lattice comprising five such atoms (c). The lowest-lying energy level remains sharp

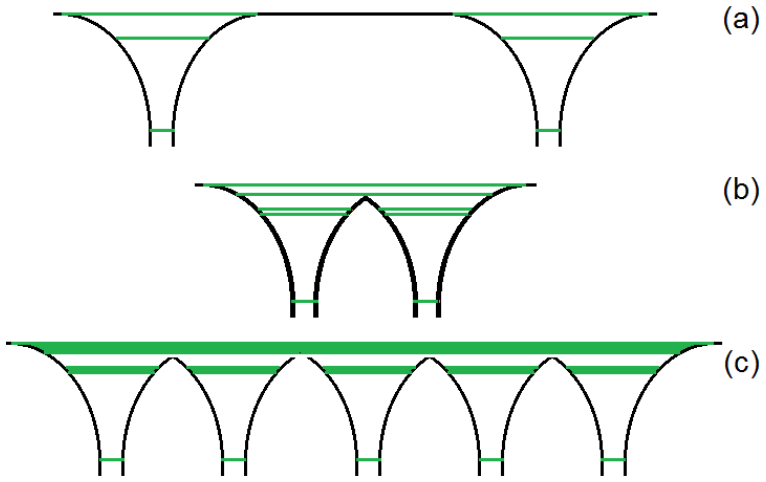

Figure 1.1: *Schematic energy levels: (a) two isolated atoms; (b) a diatomic molecule; (c) five atoms forming 1D crystal.*

because the electrons in the inner subshells are shielded from the influence of nearby atoms while the sharp energy levels associated with the outer atomic become bands as the atoms enter into close proximity.

Solids can be classified on the basis of the geometrical symmetries of their crystal structures. Thus within each of the seven crystal systems one can find solids exhibiting the full range of electrical, mechanical, and optical properties. There is another classification scheme, which is not based on symmetry,

but emphasizes physical properties. The scheme is based on the configuration of the valence electrons. The most important distinction determined by the valence electrons the one between metals and insulators. The difference between metals and insulators depends on whether there are (metals) or are not (insulators) any partially filled energy bands. In perfect crystals at zero temperature, provided that the independent electron approximation is valid, this is a completely rigorous criterion, leading to two unambiguous categories. Electrons in a completely filled band can carry no current. Within the independent electron model this result is the basis for the distinction between insulators and metals: in the ground state of an insulator all bands are either completely filled or completely empty; in the ground state of a metal at least one band is partially filled. We can characterize insulators by the energy gap, E_g, between the top of the highest filled band(s) and the bottom of the lowest empty band(s).

Figure 1.2 illustrates a simple scheme with three generic solids with different electrical properties: metal, semiconductor, insulator. The lower energy

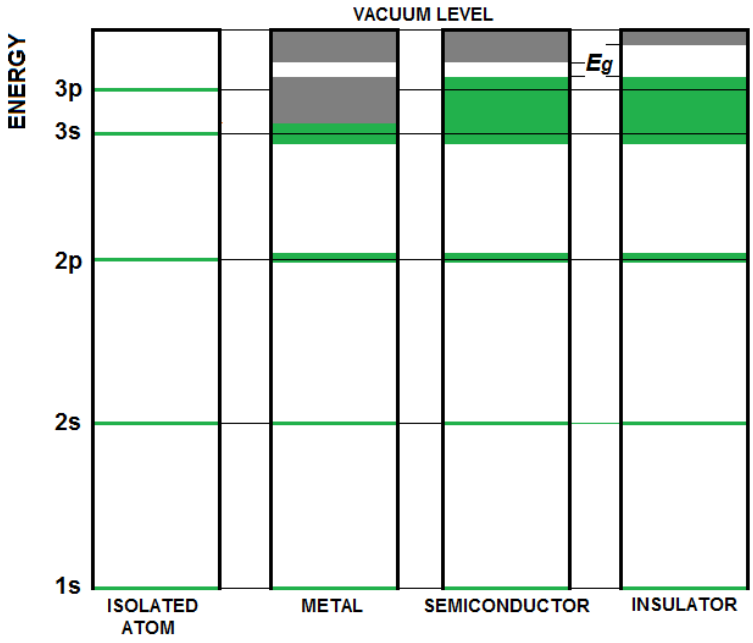

Figure 1.2: *Schematic illustration of discrete energy levels enlargement of an isolated atom into energy bands when atoms in close proximity form a solid. Fully occupied bands are green, unoccupied bands are gray, partially occupied bands are both green and gray,the forbidden bands are white.*

levels in the solids (denoted 1s, 2s, and 2p levels in this example) are simi-

lar to those of the isolated atom. They are not broadened because they are filled by core atomic electrons that are well shielded from the external fields produced by neighboring atoms. In contrast, the energies of the higher-lying discrete atomic levels split into closely spaced discrete levels and form bands. The highest partially occupied band is called the conduction band; the valence band lies below it. They are separated by the energy bandgap. The lowest-energy bands are filled first.

Electrons in a completely filled band cannot transport current. In the framework of the independent electron model this result is the origin for the difference between insulators and metals: in the ground state of an insulator all bands are either completely filled or completely empty; in the ground state of a metal at least one band is partially filled. We can characterize insulators by the energy gap between the top of the highest filled band(s) and the bottom of the lowest empty band(s). A solid with an energy gap will be nonconducting at T = 0. However, when the temperature is not zero there is a probability that some electrons will be thermally excited across the energy gap into the lowest unoccupied bands, called the conduction bands, leaving behind unoccupied levels in the highest occupied bands, called valence bands. The thermally excited electrons are able of conducting, and hole-type conduction can occur in the valence band. Whether such thermal excitation leads to appreciable conductivity depends critically on the size of the energy gap: with an energy gap of 4eV at room temperature essentially electrons are not excited across the gap; with an E_g of 0.25eV, measurable conduction will occur. Solids that are insulators at $T = 0$, but whose energy gaps are of such a size that thermal excitation can lead to observable conductivity at temperatures below the melting point, are known as semiconductors. The difference between a semiconductor and an insulator is not a sharp one. In most important semiconductors the energy gap is less than 2eV and frequently as low as a few tenths of an electron volt. Typical room temperature resistivities of semiconductors are between 10^{-3} and 10^{9} Ωcm (in contrast to metals, where ρ is about 10^{-6} Ωcm, and good insulators, where rho can be as large as 10^{22} Ωcm).

Since the number of electrons excited thermally into the conduction band (and therefore the number of holes they leave behind in the valence band) varies exponentially with 1/T, the electrical conductivity of a semiconductor should be a very rapidly increasing function of temperature. This is in striking contrast to the case of metals. The conductivity of a metal declines with increasing temperature, for the density of carriers n is independent of temperature, and all temperature dependence comes from the relaxation time τ which generally decreases with increasing temperature because of the increase in electron-phonon scattering. The relaxation time in a semiconductor

will also decrease with increasing temperature, but this effect (typically described by a power law) is quite overwhelmed by the very much more rapid increase in the density of carriers with increasing temperature.

Thus the most striking feature of semiconductors is that, unlike metals, their electrical resistance declines with rising temperature; i.e., they have a negative coefficient of resistance. It was this property that first brought them to the attention of physicists in the early nineteenth century. By the end of the nineteenth century a considerable body of semiconducting knowledge had been amassed; it was observed that the thermopowers of semiconductors were anomalously large compared with those of metals (by a factor of 100 or so), that semiconductors exhibited the phenomenon of photoconductivity, and that rectifying effects could be obtained at the junction of two unlike semiconductors. Early in the twentieth century, measurements of the Hall effect were made confirming the fact that the temperature dependence of the conductivity was dominated by that of the number of carriers, and indicating that in many substances the sign of the dominant carrier was positive rather than negative. Phenomena such as these were a source of considerable mystery until the full development of band theory many years later. Within the band theory they find simple explanations.

1.2 Semiconductors

Materials can be categorised into conductors, semiconductors or insulators by their ability to conduct electricity.

In normal conditions, insulators do not conduct electricity because their valence electrons are not free to wander throughout the material. In fact they are free to move around, however, in an insulator there are as many electrons as there are energy levels for them to occupy. If an electron swaps place with another electron no change is made since electrons are indistinguishable. There are higher energy levels, but to promote the electrons to these energy levels requires more energy than is usually practical.

Metals conduct electricity easily because the energy levels between the conduction and valence band overlap, or there are more energy levels available than there are electrons to fill them so very little energy is required to find new energies for electrons to occupy. The resistivity of a material is a measure of how difficult it is for a current to flow. Semiconductors have a resistivity between $10^{-4} < \rho < 10^{8}$ although these are rough limits. The band theory of materials explains qualitatively the difference between these types of materials. Electrons occupy energy levels from the lowest energies upwards. However, some energy levels are forbidden because of the wave like

properties of atoms in the material. The allowed energy levels tend to form bands. The highest filled level at $T = 0$ K is known as the valence band. Electrons in the valence band do not participate in the conduction process. The first unfilled level above the valence band is known as the conduction band. In metals, there is no forbidden gap; the conduction band and the valence band overlap, allowing free electrons to participate in the conduction process. Insulators have an energy gap that is far greater than the thermal energy of the electron, while semiconductor materials the energy gap is typically around $1eV$.

Elemental semiconductors

Elemental semiconductors are semiconductors where each atom is of the same type such as Ge and Si. These atoms are bound together by covalent bonds, so that each atom shares an electron with its nearest neighbour, forming strong bonds. Compound semiconductors are made of two or more elements. Common examples are GaAs or InP. These compound semiconductors belong to the III-V semiconductors so called because first and second elements can be found in group III and group V of the periodic table respectively. In compound semiconductors, the difference in electro-negativity leads to a combination of covalent and ionic bonding. Ternary semiconductors are formed by the addition of a small quantity of a third element to the mixture, for example $Al_xGa_{1-x}As$. The subscript x refers to the alloy content of the material, what proportion of the material is added and what proportion is replaced by the alloy material. The addition of alloys to semiconductors can be extended to include quaternary materials such as $Ga_xIn_{(1-x)}As_yP_{(1-y)}$ or GaInNAs and even quinternary materials such as GaInNAsSb. Once again, the subscripts denote the proportion elements that constitute the mixture of elements. Alloying semiconductors in this way allows the energy gap and lattice spacing of the crystal to be chosen to suit the application.

Intrinsic semiconductors

Intrinsic semiconductors are essentially pure semiconductor materials. The semiconductor material structure should contain no impurity atoms. Elemental and compound semiconductors can be intrinsic semiconductors. At room temperature, the thermal energy of the atoms may allow a small number of the electrons to participate in the conduction process, unlike metals, where the resistance of the material decreases with temperature, in semiconductors, as the temperature increases, the thermal energy of the valence electrons increases, allowing more of them to breach the energy gap into the

conduction band. When an electron gains enough energy to escape the electrostatic attraction of its parent atom, it leaves behind a vacancy which may be filled be another electron. The vacancy produced can be thought of as a second carrier of positive charge. It is known as a hole. As electrons flow through the semiconductor, holes flow in the opposite direction. If there are n free electrons in an intrinsic semiconductor, then there must also be n holes. Holes and electrons created in this way are known as intrinsic charge carriers. The carrier concentration, or charge density, defines the number of charge carriers per unit volume. This relationship can be expressed as $n = p$ where n is the number of electrons and p the number of holes per unit volume. The variation in the energy gap between different semiconductor materials means that the intrinsic carrier concentration at a given temperature also varies.

Extrinsic semiconductors

An extrinsic semiconductor can be formed from an intrinsic semiconductor by adding impurity atoms to the crystal in a process known as doping. To take the most simple example, consider Silicon. Since Silicon belongs to group IV of the periodic table, it has four valence electrons. In the crystal form, each atom shares an electron with a neighbouring atom. In this state it is an intrinsic semiconductor. B, Al, In, Ga all have three electrons in the valence band. When a small proportion of these atoms, (less than 1 in 10^6), is incorporated into the crystal the dopant atom has an insufficient number of bonds to share bonds with the surrounding Silicon atoms. One of the Silicon atoms has a vacancy for an electron. It creates a hole that contributes to the conduction process at all temperatures. Dopants that create holes in this manner are known as acceptors. This type of extrinsic semiconductor is known as p-type as it creates positive charge carriers. Elements that belong to group V of the periodic table such as As, P, Sb have an extra electron in the valence band. When added as a dopant to intrinsic Silicon, the dopant atom contributes an additional electron to the crystal. Dopants that add electrons to the crystal are known as donors and the semiconductor material is said to be n-type.

Doping of compound semiconductors

Doping of compound semiconductors is slightly more complicated. The effect of the dopant atom depends on the site occupied by the atom in the lattice. In III-V semiconductors, atoms from group II act as a acceptors when occupying the site of a group III atom, while atoms in group VI act as donors when they replace atoms from group V. Dopant atoms from group IV have the property

that they can act as acceptors or donors depending on whether they occupy the site of group III or group V atoms respectively. Such impurities are known as amphoteric impurities.

Semimetals

According to electronic band theory, there are other elements in the solid classification: semimetals. Semimetals should not be confused with semiconductors. A pure semimetal at $T = 0$ is a conductor: there are partially filled electron and hole bands. A semiconductor, however, conducts only because carriers are either thermally excited or introduced by impurities. A pure semiconductor at $T = 0$ is an insulator. Metals have a partially filled conduction band. A semimetal is a material with a very small overlap between the bottom of the conduction band and the top of the valence band. A semimetal thus has no band gap and a negligible density of states at the Fermi level. A metal, by contrast, has an appreciable density of states at the Fermi level because the conduction band is partially filled.

1.3 Junctions

Junctions are of great importance both in modern electronics applications and in the detectors manufacturing processes, in our case we will focus on light detectors. The basic p-n junction theory is the foundation of the physics of semiconductor devices. The basic p-n junctions theory was carried out by Shockley [3] [4], and then extended by Sah, Noyce, and Shockley [5], and by Moll [6].

A p-n junction is a two-terminal device and can perform various terminal functions depending on the doping profile, device geometry, and biasing condition. Junctions between differently doped regions of a semiconductor material are called **homojunctions**. An important example is the p-n junction, which is discussed in this subsection. The chapter closes with a discussion on the heterojunctions, which are junctions formed between dissimilar semiconductors (e.g., n-type GaAs on p-type AlGaAs).

1.3.1 The P-N junction

A p-n junction is a homojunction between a p-type and an n-type semiconductor. A p-n junction consists of a p-type and an n-type section of the same semiconducting materials in metallurgical contact with each other. The p-type region has an abundance of holes (majority carriers) and few mobile

electrons (minority carriers); the n-type region has an abundance of mobile electrons and few holes (figure 1.3). Both charge carriers are in continuous

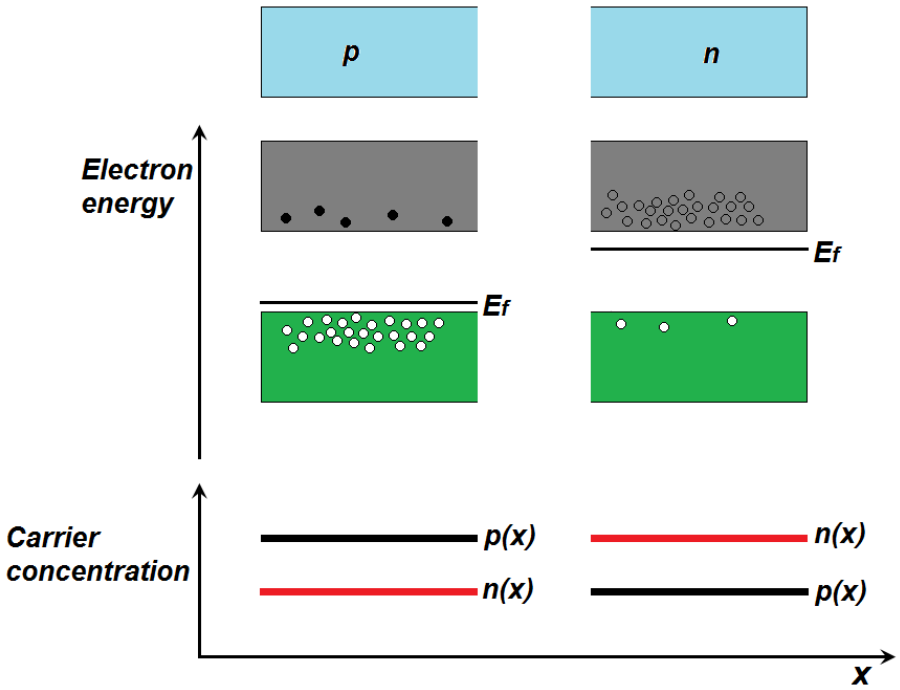

Figure 1.3: *Energy levels and carrier concentrations of a p-type and an n-type isolated semiconductor.*

random thermal motion in all directions. When the two regions are brought into contact (figure 1.4), the following sequence of events takes place. First, electrons and holes diffuse from areas of high concentration toward areas of low concentration. Thus electrons diffuse away from the n-region into the p-region, leaving behind positively charged ionized donor atoms. In the p-region the electrons recombine with the abundant holes. Similarly, holes diffuse away from the p-region, leaving behind negatively charged ionized acceptor atoms. In the n-region the holes recombine with the abundant mobile electrons. This diffusion process cannot continue indefinitely, however, because it causes a disruption of the charge balance in the two regions.

Second, As a result, a narrow region on both sides of the junction becomes almost totally depleted of mobile charge carriers. This region is called the depletion layer. It contains only the fixed charges (positive ions on the n-side and negative ions on the p-side). The thickness of the depletion layer in each region is inversely proportional to the concentration of dopants in the region.

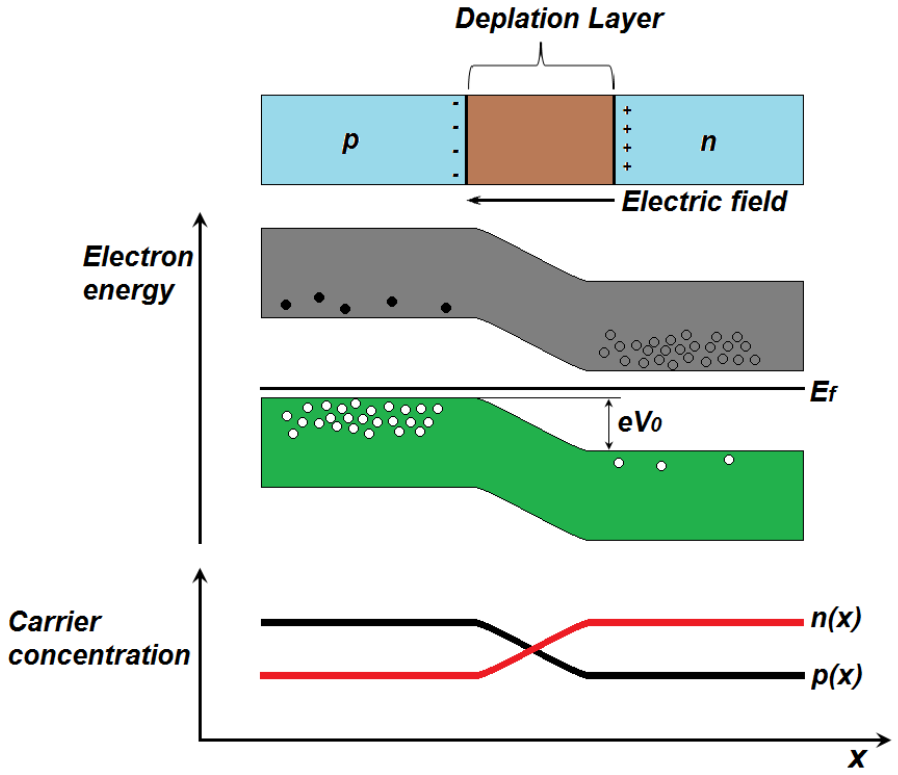

Figure 1.4: *A p-n junction in thermal equilibrium at $T > 0K$. The depletion-layer, energy-band diagram, and concentrations (on a logarithmic scale) of mobile electrons $n(x)$ and holes $p(x)$ are shown as functions of position x. The built-in potential difference V_0 corresponds to an energy eV_0, where e is the magnitude of the electron charge.*

Third, the fixed charges create an electric field in the depletion layer which points from the n-side toward the p-side of the junction. This built-in field obstructs the diffusion of further mobile carriers through the junction region.

Fourth, an equilibrium condition is established that results in a net built-in potential difference V_0 between the two sides of the depletion layer, with the n-side exhibiting a higher potential than the p-side.

Fifth, the built-in potential provides a lower potential energy for an electron on the n-side relative to the p-side. As a result, the energy bands bend as shown in in thermal equilibrium there is only a single Fermi function for the entire structure so that the Fermi levels in the p- and n-regions must align.

Sixth, no net current flows across the junction. The diffusion and drift currents cancel for the electrons and holes independently. An externally applied potential will alter the potential difference between the p- and n-regions. If the junction is forward biased by applying a positive voltage V to the p-region (figure 1.5), its potential is increased with respect to the n-region, so that an electric field is produced in a direction opposite to that of the built-in field. The presence of the external bias voltage causes a departure from

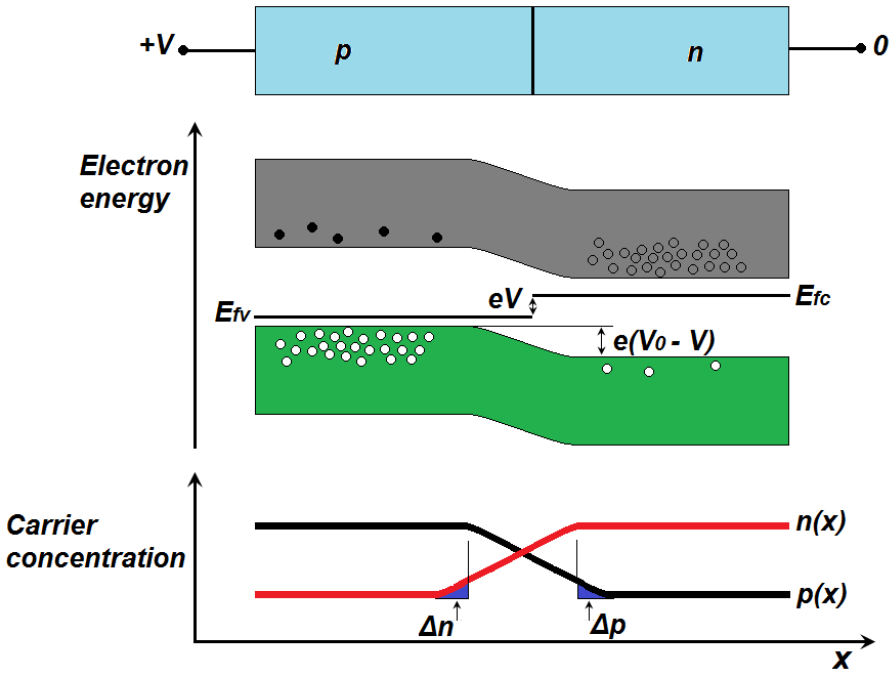

Figure 1.5: *Energy-band diagram and carrier concentrations in a forward-biased p-n junction. Δn and Δp are the excess electrons and the excess holes, respectively.*

equilibrium and a misalignment of the Fermi levels in the p- and n-regions, as well as in the depletion layer. The presence of two Fermi levels in the depletion layer, E_{fc} and E_{fv} represents a state of quasi-equilibrium. The net effect of the forward bias is a reduction in the height of the potential-energy hill by an amount eV. The majority carrier current turns out to increase by an exponential factor $exp(eV/kT)$ so that the net current becomes $i = i_s exp(eV/kT) - i_s$, where i_s is a constant. The excess majority carrier holes and electrons that enter the n- and p-regions, respectively, become minority carriers and recombine with the local majority carriers. Their concentration therefore decreases with distance from the junction as shown in figure 1.5,

this process is known as minority carrier injection. If the junction is reverse biased by applying a negative voltage V to the p-region, the height of the potential-energy hill is increased by eV. This impedes the flow of majority carriers. The corresponding current is multiplied by the exponential factor $exp(eV/kT)$, where V is negative; i.e., it is reduced. The net result for the current is $i = i_s exp(eV/kT) - i_{s'}$ so that a small current of magnitude $\approx i_s$ flows in the reverse direction when $|V| \gg kT/e$.

A p-n junction therefore acts as a diode with a current-voltage (I-V) characteristic

$$i = i_s \left[e^{\left(\frac{eV}{kT}\right)} - 1 \right] \tag{1.1}$$

as illustrated in figure 1.6. The response of a p-n junction to a dynamic

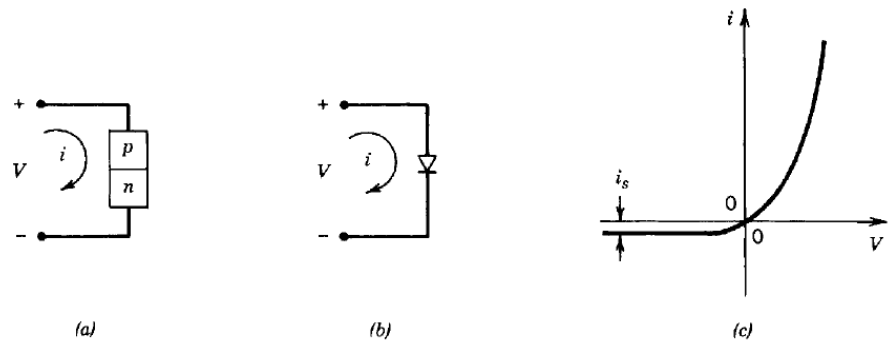

Figure 1.6: *(a) Voltage and current in a p-n junction. (b) Circuit representation of the p-n junction diode. (c) Current-voltage characteristic of the ideal p-n junction diode.*

(ac) applied voltage is determined by solving the set of differential equations governing the processes of electron and hole diffusion, drift (under the influence of the built-in and external electric fields), and recombination. These effects are important for determining the speed at which the diode can be operated. They may be conveniently modeled by two capacitances, a junction capacitance and a diffusion capacitance, in parallel with an ideal diode. The junction capacitance accounts for the time necessary to change the fixed positive and negative charges stored in the depletion layer when the applied voltage changes. The thickness l of the depletion layer turns out to be proportional to $(V_0 - V)^{1/2}$; it therefore increases under reverse-bias conditions (negative V) and decreases under forward-bias conditions (positive V). The junction capacitance $C = \epsilon A/l$ (where A is the area of the junction) is therefore inversely proportional to $(V_0 - V)^{1/2}$. The junction capacitance

of a reverse-biased diode is smaller (and the RC response time is therefore shorter) than that of a forward-biased diode.

Minority carrier injection in a forward-biased diode is described by the diffusion capacitance, which depends on the minority carrier lifetime and the operating current.

1.3.2 The p-i-n junction

A p-i-n diode is made by inserting a layer of intrinsic (or lightly doped) semiconductor material between a p-type region and an n-type region (figure 1.7). Because the depletion layer extends into each side of a junction by a distance inversely proportional to the doping concentration, the depletion layer of the p-i junction penetrates deeply into the i-region. Similarly, the depletion layer of the i-n junction extends well into the i-region. As a result, the p-i-n diode can behave like a p-n junction with a depletion layer that encompasses the entire intrinsic region. The electron energy, density of fixed charges, and the electric field in a p-i-n diode in thermal equilibrium are illustrated in figure 1.7.

One advantage of using a diode with a large depletion layer is its small junction capacitance and its consequent fast response. For this reason, p-i-n diodes are favored over p-n diodes for use as semiconductor photodiodes. The large depletion layer also permits an increased fraction of the incident light to be captured, thereby increasing the photodetection efficiency (this effect will be treated in section 2.4.1).

1.4 Heterojunctions

A heterojunction is a junction formed between two dissimilar semiconductors, or in other word, junctions between materials of different bandgap.

A first study of this structure was proposed by Shockley [17].

Heterojunctions are used in novel bipolar and field-effect transistors, and in optical sources and detectors. They can provide substantial improvement in the performance of electronics and optoelectronics devices. Their development has been made possible by modern material growth techniques. An example of heterojunction is that created between Silicon and carbon nanotubes, details will be discussed in chapter 4.

When semiconductors of different band gaps, work functions, and electron affinities are brought together to form a junction, we expect discontinuities in the energy bands as the Fermi levels line up at equilibrium. The behaviour of a semiconductor junction depends crucially on the alignment of the energy

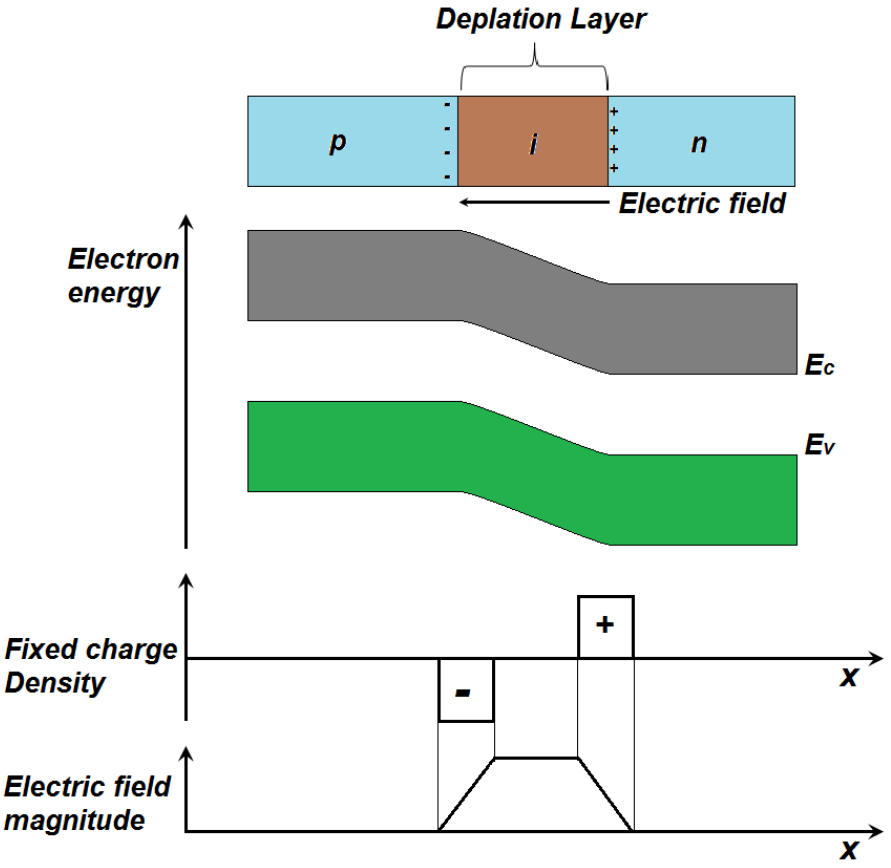

Figure 1.7: *Electron energy, fixed-charge density, and electric field magnitude for a diode in thermal equilibrium.*

bands at the interface. Various models exist to predict the band alignment. The simplest (and least accurate) model is Anderson's rule [16], or electron affinity rule, which predicts the band alignment based on the properties of vacuum-semiconductor interfaces (in particular the vacuum electron affinity). The main limitation is its neglect of chemical bonding. The discontinuities in the conduction band ΔE_C and the valence band ΔE_V accommodate the difference in band gap between the two semiconductors ΔE_g. In an ideal case, ΔE_C would be the difference in electron affinities $q(\chi_2 - \chi_1)$, and E_v would be found from $E_g - E_C$.

To draw the band diagram for a heterojunction accurately, we must not only use the proper values for the band discontinuities but also account for the band bending in the junction. To do this, we must solve Poisson's equation across the heterojunction, taking into account the details of doping and space

charge, which generally requires a computer solution. We can, however, sketch an approximate diagram without a detailed calculation. Given the

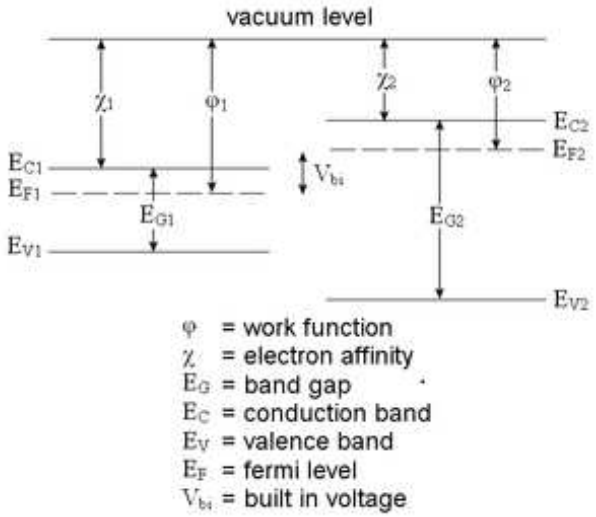

Figure 1.8: *Anderson's rule is used for the construction of energy band diagrams of the heterojunction between two semiconductor materials. The rule states that when constructing an energy band diagram, the vacuum levels of the two semiconductors on either side of the heterojunction should be aligned..*

experimental band offsets (figure 1.8) ΔE_V and ΔE_C, we can proceed as follows:

1. Align the Fermi level with the two semiconductor bands separated. Leave space for the transition region.

2. The metallurgical junction (x = 0) is located near the more heavily doped side. At x = 0 put ΔE_V and ΔE_C, separated by the appropriate band gaps.

3. Connect the conduction band and valence band regions, keeping the band gap constant in each material.

Steps 2 and 3 of this procedure are where the exact band bending is important and must be obtained by solving Poisson's equation. In step 2 we must use the band offset values ΔE_V and ΔE_C for the specific pair of semiconductors in the heterojunction.

1.4.1 Isotype heterojunction

When two semiconductors have the same type of conductivity, the junction is called an **isotype** heterojunction. Anderson [18] proposed (based on the previous work of Shockley) the first energy-band model of an idealized anisotype abrupt heterojunction.

Figures 1.9 shows the energy-band diagrams of a heterojunction formed between two semiconductors of opposite types, obtained following the Anderson's rule. In this case, the narrow-bandgap material is n-type. The two semiconductors are assumed to have different bandgaps E_g, different permittivities ϵ_s, different work functions ϕ_m, and different electron affinities χ. The difference in energy of the conduction-band edges in the two semiconductors is represented by ΔE_C, and that in the valence-band edges by ΔE_V. When

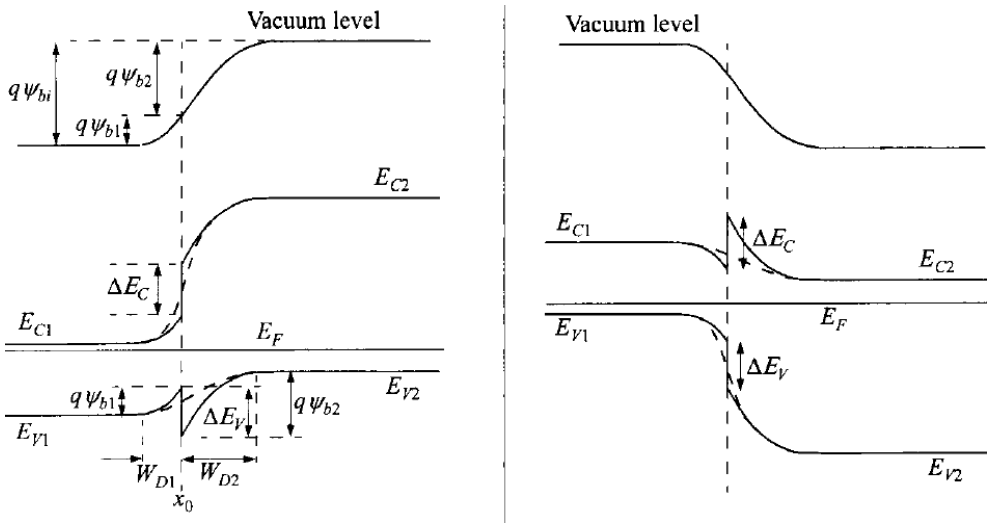

Figure 1.9: *Schematic energy-band diagrams for two semiconductors of opposite types and different E_g (of which the smaller bandgap is n-type, on the left) and their idealized anisotype heterojunction at thermal equilibrium. On the right, the smaller bandgap is p-type, the dashed lines across the junctions represent graded composition.*

a junction is formed between these semiconductors, the energy-band profile at equilibrium is as shown in figure 1.9 for an n-p anisotype heterojunction where, in this example, the narrow-bandgap material is n-type.

In the proposed model, the difusion currents are similar to a regular p-n junction but with the appropriate parameters in place. The electron and

hole diffusion currents are:

$$J_n = \frac{qD_{n2}n_{i2}^2}{L_{n2}N_{A2}}\left[e^{\left(\frac{qV}{kT}\right)} - 1\right] \tag{1.2}$$

$$J_p = \frac{qD_{p1}n_{i1}^2}{L_{p1}N_{D1}}\left[e^{\left(\frac{qV}{kT}\right)} - 1\right] \tag{1.3}$$

Note that the band offsets ΔE_C and ΔE_V are not present, and also that each diffusion current component depends on the properties of the receiving side only, as in the case of a homojunction. The total current is given by

$$J = J_n + J_p = \left(\frac{qD_{n2}n_{i2}^2}{L_{n2}N_{A2}} + \frac{qD_{p1}n_{i1}^2}{L_{p1}N_{D1}}\right)\left[e^{\left(\frac{qV}{kT}\right)} - 1\right] \tag{1.4}$$

1.4.2 Anisotype heterojunction

When two semiconductors have different type of conductivity, the junction is called an **anisotype** heterojunction. The following energy band diagrams are obtained applying Anderson's rule.

Left side of figure 1.10 shows the idealized equilibrium energy-band diagram for n-n heterojunctions, and right side of the same figure shows the diagram for p-p heterojunctions.

In a n-n heterojunction, since the work function of the wide-bandgap semiconductor is smaller, the energy bands will be bent oppositely to those for the n-p case.

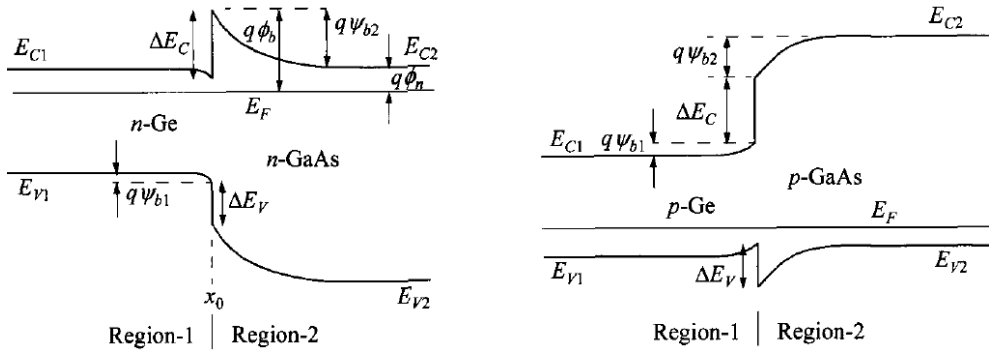

Figure 1.10: *Energy-band diagrams for ideal (left side) n-n and (right side) p-p isotype heterojunctions.*

The model yields the current-voltage relationship

$$J = J_0\left[e^{\left(\frac{qV}{kT}\right)} - 1\right] \tag{1.5}$$

The reverse current J_0 never saturates but increases linearly with voltage at large $-V$, and is given by

$$J_0 = \frac{q\psi_{bi}A^*T}{k}\left(1 - \frac{V}{\psi_{bi}}\right)e^{\left(\frac{-q\psi_{b1}}{kT}\right)}e^{\left(\frac{-q\phi_b}{kT}\right)} \tag{1.6}$$

1.4.3 Device applications

Heterojunctions have found use in a variety of specialized applications.

Solar cells with heterojunction contacts are able to achieve particularly high electrical voltages. This takes advantage of the fact that materials with larger band gaps have lower minority charge carrier concentrations and therefore recombination at the metal/semiconductor interface of these areas is minimized. Consequently, in contrast to what is usual in standard homojunction solar cells, contacting can therefore be combined with passivation. For crystalline silicon wafers this combination of contacting and passivation as an absorber material is very efficiently accomplished with layers of amorphous silicon, which has a significantly larger band gap than crystalline silicon. At present, the maximum efficiency of this solar cell is in the range of 22-23%.

Heterostructure photodiodes, formed from two semiconductors of different bandgaps, can exhibit advantages over p-n junctions fabricated from a single material. A heterounction comprising a large band gap material ($E_s > h\nu$), for example, can make use of its transparency to minimize optical absorption outside the depletion region. The large band gap material is then called a window layer. The use of different materials can also provide devices with a great deal of flexibility. Several material systems are of particular interest:

- $Al_xGa_{1-x}/GaAs$ is useful in the wavelength range 0.7 to 0.87 μm.
- $In_{0.53}Ga_{0.47}/InP$ operates at 1.65 μm in the near infrared ($E_g = 0.75$eV). Typical values for the responsivity and quantum efficiency of detectors fabricated from these materials are 0.7 A/W and 0.75, respectively. The gap wavelength can be compositionally tuned over the range of interest for fiber-optic communication, 1.3-1.6 μm.
- $Hg_xCd_{1-x}Te/CdTe$ is a material that is highly useful in the middle-infrared region of the spectrum. This is because HgTe and CdTe have nearly the same lattice parameter and can therefore be lattice matched at nearly all compositions. This material provides a compositionally tunable band gap that operates in the wavelength range between 3 and 17 μm.

- Quaternary materials, such as $In_{1-x}Ga_xAs_{1-y}P_y/InP$ and $Ga_{1-x}Al_xAs_ySb_{1-y}/GaSb$, which are useful over the range 0.92 to 1.7 μm, are of particular interest because the fourth element provides an additional degree of freedom that allows lattice matching to be achieved for different compositionally determined values of E_g.

Chapter 2

Solid state photodetectors

Today the technology that allows detection of light is a fundamental tool that provides deeper understanding of more sophisticated phenomena. Light measurement offers exclusive opportunities, due to the fact that light can be used to measure directly or indirectly a wide variety of physical phenomena. In particular, such advanced fields as technological and scientific measurements, medical diagnosis and treatment, etc., require photosensitive devices that exhibit extreme performances. Measurements using light can be divided in two types: active and passive methods. In the case of active methods, an object is illuminated with a light source and then the light is detected as reflected, transmitted or scattered light, etc. On the other hand, in the passive methods, the detected light is emitted from the physical process under investigation.

Photonics is the science which studies and controls the flow of photons, as electronics is the science which study and controll the flow of charge carriers (electrons and holes). These two sciences join together in semiconductor optoelectronics: photons can generate and control charge carriers, and carriers can generate and control the flow of photons. Semiconductor optoelectronic devices serve as photon sources (light-emitting diodes (LED), and laser diodes), amplifiers, detectors, waveguides, modulators, sensors, and nonlinear optical elements. The compatibility of semiconductor optoelectronic devices and electronic devices has encouraged the development of both fields. Semiconductor photodetectors and semiconductors photon sources are inverse devices. Detectors convert an incident photon flux into an electric current; sources do the opposite.

The development of novel radiation detectors is important for future experiments and it opens the field to new investigations. The availability of a cheap, wide area, highly pixelated radiation detectors represents a goal of primary importance for researchers. The ultra-violet wavelength range is the

most investigated for its large field of application and its importance for particle detection. For space physics and for astroparticle physics envisaged for the next decade it will be indispensable to develop UV sensitive detectors, high pixelated and with high quantum efficiency, as described in the Cosmic Vision 2015-2025 plan for the ESA science programme that cites: "The proposed mission will be based on large openings and large field-of-view optics with high throughput, as well as on large area, highly pixelled, fast and high detection efficiency near-UV camera".

Although the practical short wavelength limit for silicon is approximately 250 nm, silicon photodetectors can be used at wavelengths as short as 190 nm (figure 2.1). UV radiation, however, readily damages silicon detectors.

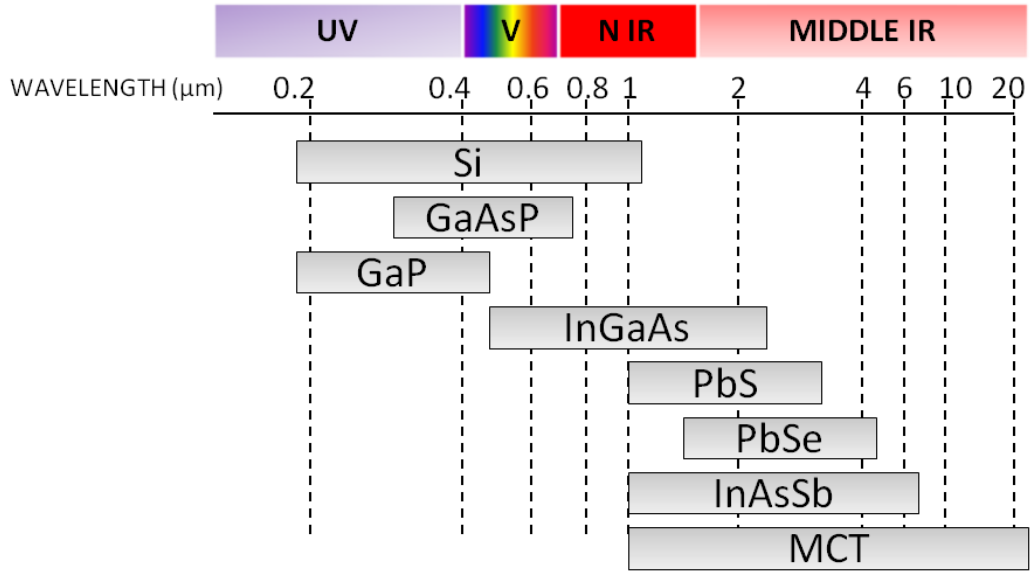

Figure 2.1: *Wavelength range covered by solid-state photodetectors.*

Degradation in responsivity occurs after only a few hours of ultraviolet exposure and makes the devices unusable for precision measurements.

This chapter is devoted to a study of various solid-state photodetectors [20] [19]. We begin with a discussion of the external and internal photoeffect and we set their fundamental properties, including quantum efficiency, responsivity, response time, and noise.

Then we focus our attention on four types of semiconductors photodetectors: photoconductors, photodiodes, avalance photodiodes, and Silicon Photomultipliers (SiPMs), respectively.

2.1 Photodetectors

Photonic devices are those in which the light particle (the photon) plays a key role. They can detect, geneate and convert optical energy to electrical energy, or vice versa. Photonic devices can be divided into three groups:

1. Devices as light sources that convert electrical energy into optical radiation: the LED and the diode LASER (Light Amplification by Stimulated Emission of Radiation).

2. Devices that convert optical radiation into electrical enegy: the photovoltaic device or solar cell.

3. Devices that detect optical signals: photodetectors.

The third group is considered in this chapter. In general, the operation of a photodetector includes three processes:

- carrier generation by incident light;
- carrier transport and/or multiplication by current-gain mechanism if present;
- extraction of carriers to provide the output signal.

Photodetectors or photosensors can be generally classified by their operating principle into three classes:

- external photoelectric effect,
- internal photoelectric effect,
- thermal types.

In the *external photoelectric effect* electrons are emitted from atoms when they absorb energy from light. Infact, if the energy of a photon illuminating a material in vacuum is sufficiently large, the excited electron can escape over the potential barrier af the surface of the material and be liberated into the vacuum as a free electron. This proces is illustrated in figure 2.2 for a metal. An incident photon of energy $h\nu$ releases a free electron from whithin the partially filled conduction band. Energy conservation requires that electrons emitted from below the Fermi level, where they are pletiful, have a maximum kinetic energy given by Einstein's photoemission equation:

$$E_{max} = h\nu - W \tag{2.1}$$

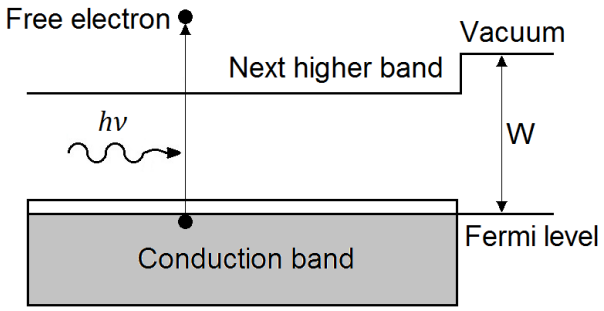

Figure 2.2: *Photoelectric emission from a metal. W is the photoelectric work function.*

where W is the photoelectric work function, which is the energy difference between the vacuum level and the Fermi level of the metal. Only if the electron is initially lies at the Fermi level can it receive the maximum kinetic energy specified in 2.1; the removal of a deeper-lying electron requires additional energy to transport it to the Fermi level, thereby reducing the kinetic energy of the liberated electron. The lowest work function for a metal (Cs) is about $2eV$, so that optical detectors based on the external photoelectric effect from pure metals are useful in the visible and ultraviolet regions of the spectrum.

In the case of photoelectric emission from an intrinsic semiconductor, the formula is similar to 2.1:

$$E_{max} = h\nu - W = h\nu - (E_g - \chi) \tag{2.2}$$

where E_g is the bandgap energy and χ is the electron affinity of the material (the energy difference between the vacuum level and the bottom of the conduction band). Photoelectric emission from an intrinsic semiconductor is schematically shown in figure 2.3. The energy $E_g + \chi$ can be small as $1.4eV$ for certain materials (e.g. multialkali compound NaKCsSb, which forms the basis for the so-colled S-20-type photocatode), so that semiconductor photoemissive detectors can operate in the near infrared, as well as in the visible and ultraviolet regions of the spectrum. In their simplest form, photodetectoros based on photoelectric emission are the vacuum photodiodes or phototubes. On the other side, photomultiplier tubes (PMT) have gain mechanism and are superior in response speed and sensitivity (low-light-level detection).

Most modern photodetectors are based on the *internal photoelectric effect*, in which the photoexcited carriers remain within the material. For example, the absorbtion of a photon by an intrinsic semiconductor results in

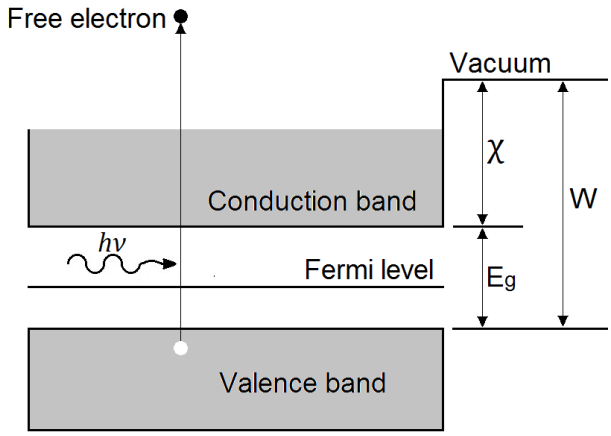

Figure 2.3: *Photoelectric emission from an intrinsic semiconductor. E_g is the bandgap energy, χ the electron affinity and W the photoelectric work function.*

the generation of a free electron excited from the valence band to the conduction band (figure 2.4) Detectors based on this effects are further divided

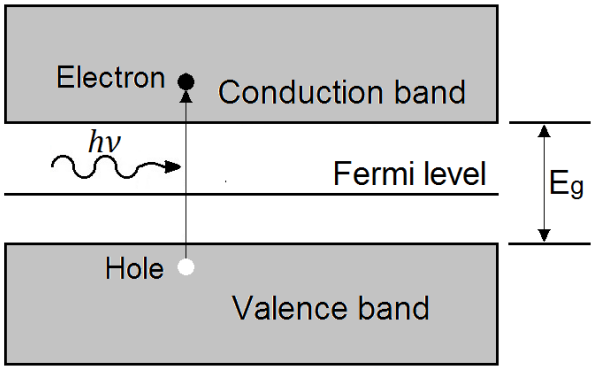

Figure 2.4: *Electro-hole photogeneration in a semiconductor.*

into photovoltaic and photoconductive types. In the photovoltaic effects the incident light causes a voltage to appear at the output of the device; in the photoconductive case the incident light changes the internal resistance of the material.

Thermal type photosensors are further divided in electromotive forces types that convert heat into electromotive forces; conductive types that convert heat into conductivity; surface charge types that convert heat into a surface charge. An example of these devices are the pyroelectric detectors.

These kind of photosensors have a sensitivity not dependent on the wavelength, but there are drawbacks in response speed and detection capability.

2.2 Properties of solid-state photodetectors

Certain general features are associated with all semiconductor photodetectors. Before considering the details of specific devices of our interest, we look over the quantum efficiency, responsivity, response time, and noise of photoelectric devices from a general point of view.

2.2.1 Quantum efficiency

The quantum efficiency η is defined as the probability that a single photon incident on the device will generate a photocarrier pair that contributes to the detector current. When many photons are incident, η becomes the flux of generated electron-hole pairs that contribute to the detector current divided by the flux of incident photons. This quantity ranging from 0 to 1, and sometimes is expressed in percent (%).

Not all incident photons produce electron-hole pairs because not all of them are absorbed. As illustrated in figure 2.5, some of the photons are reflected at the surface of the detector while others fail to be absorbed because the material does not have sufficient thickness. Furthermore, some

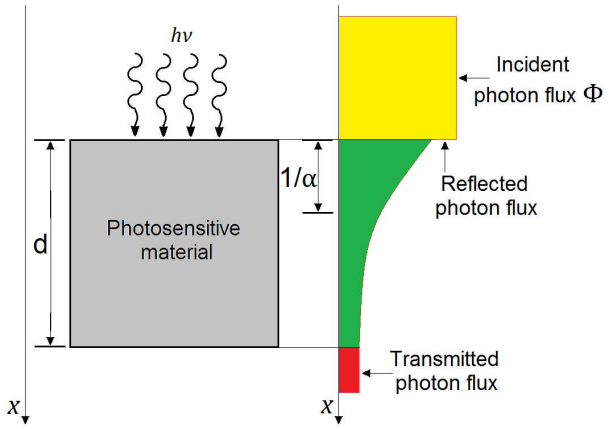

Figure 2.5: *Effect of surface reflection and incomplete absorbtion on the detector quantum efficiency.*

electron-hole pairs produced near the surface of the detector quickly recom-

bine because of the abundance of recombination centers at the surfaces, and are therefore not avaible to cotribute to the photodetector current.

The quantum efficincy can be therefore written as

$$\eta = (1 - \mathcal{R})\,\xi\left[1 - e^{(-\alpha d)}\right] \tag{2.3}$$

where

- $\mathcal{R}$ is the optical power reflectance at the surface,
- ξ the fraction of electron-hole pairs that successfully contribute to the detector current,
- α the absorbtion coefficient of the material,
- d the photodetector depth.

This definition of quantum efficiency [2.3] is the product of three factors:

- $(1 - \mathcal{R})$ represents the effect of reflection at the surface of the device (some definition of quantum efficiency η exclude this quantity, which must then be considered separately).
- ξ is the fraction of electron-hole pairs that successfully avoid recombination at the material surface and contribute to the useful photocurrent.
- $\left[1 - e^{(-\alpha d)}\right]$ represents the fraction of the photon flux absorbed in the bulk of the material. A large value of d is desiderable, in order to maximize this factor.

Of course, additional loss occurs if the light is not properly focussed onto the active area of the detector.

The quantum efficiency is wavelength dependent, principally because the absorbtion coefficient α is a function of wavelength. The characteristics of the semiconductor thus determine the spectral window whitin which η is sufficiently greater than zero. For large values of the incident light wavelength λ, the quantum efficiency is small because absorbtion cannot occur when

$$\lambda \geq \lambda_g = hc/E_g \tag{2.4}$$

where λ_g is the cut-off wavelength of the material. In this way the photon energy is smaller then the bandgap energy and so the material is transparent. The cut-off wavelength λ_g is thus the long-wavelength limit of the semiconductor. For example, for Silicon we have $E_g = 1.12$ eV, $\lambda_g = 1.11\ \mu m$, and for Germanium $E_g = 0.66$ eV, $\lambda_g = 1.88\ \mu m$. For sufficiently small values of λ, the quantum efficiency also decrease because most photons are absorbed near the surface of the device. Infact, for $\alpha = 10^4$ cm^{-1}, most of the photons are absorbed within a distance $1/\alpha = 1\mu m$

2.2.2 Responsivity

The responsivity of a photodetector is related to the current i_p flowing in the device circuit to the optical power P incident on it. If every photon generates a photocarrier pair in the device, a photon flux Φ (photons per second) would produce an electron flux Φ (electrons per second) in the photodetector circuit, corresponding to a short-circuit electric current $i_p = e\Phi$. Thus, an optical power $P = h\nu\Phi$ (watts) at a given frequency ν would give rice to an electric current $i_p = eP/h\nu$.

Since the fraction of photons producing detected electrons is η rather than unity, the electric current is

$$i_p = \eta e\Phi = \frac{\eta eP}{h\nu} \equiv \Re P \tag{2.5}$$

The proportionality factor between the electric current and the optical power, $\Re = i_p/P$, has units A/W and is called the photodetector responsivity:

$$\Re = \frac{\eta e}{h\nu} = \eta\frac{\lambda}{1.24}\ (A/W) \tag{2.6}$$

From this equation is evident that the responsivity is linearly proportional to both the quantum efficiency and the wavelength, this is shown in 2.6. An appreciation for the order of magnitude of the responsivity is gained by setting $\eta = 1$ and $\lambda = 1.24$ μm in [2.6], and then $\Re = 1$ A/W $= 1$ nA/nW. The proportionality of $\Re$ vs λ arises beacause the responsivity is

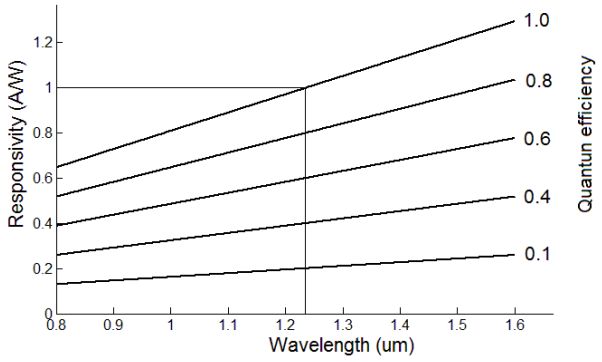

Figure 2.6: *Responsivity $\Re$ (A/W) vs wavelength λ, with the quantum efficiency η as parameter. For $\eta = 1$, $\Re = 1$ A/W at $\lambda = 1.24$ μm.*

defined on the basis of optical power, whereas most photodetectors generate currents proportional to the incident photon flux Φ. For a given photon flux

$\Phi = P/h\mu = P\lambda/hc$ (corresponding to a given photodetector current i_p), the product $P\lambda$ is fixed so that an increase in λ requires a decrease in P, thereby leading to an increase in the responsivity. For this reason thermal detectors (like piezoelectric sensors) are responsive to optical power rather then to photon flux, causing $\Re$ to be indipendent of λ.

The region over which $\Re$ increase with λ is limited, however, inasmuch the wavelength dependence of quantum efficiency comes into play at both long and short wavelengts. The responsivity can also be degraded if the detector is illuminated with a huge optical power. This condition, known as *detector saturation*, limits the linear dynamic range of the device, which is the range over which it responds linearly to the incident optical power.

The gain

The presented fomulas are predicted on the assumption that each photocarrier produces a charge e in the device circuit. However, many photodetectors produce a charge q in the circuit that differs from e. Such devices are said to exibit gain. The gain G is defined as the average number of circuit electrons generated per photocarrier pair

$$G \equiv \frac{Q}{e} \tag{2.7}$$

It can be either grater or less than unity. In fact, in the presence of gain, the formulas [2.5] and [2.6] must be modified. Substituting $q = Ge$ in [2.5] we obtain

$$i_p = \eta q \Phi = \eta G e \Phi = \frac{\eta e P G}{h\nu} \tag{2.8}$$

and substituting $q = Ge$ in [2.6] we obtain

$$\Re = \frac{\eta e G}{h\nu} = \eta G \frac{\lambda}{1.24} \; (A/W) \tag{2.9}$$

The gain of the photodetector must be distinguished from the efficiency, which is the probability that an incident photon produces a detectable photocarrier pair.

2.2.3 Response time

If we apply a constant electric field E to a semiconductor (or metal), free charge carriers are accelerated. During their motion, the carriers enconter frequent collision with lattice ions moving about their equilibrium positions via thermal motion, and also with cristal lattice imperfection associated with

impurity ions. These collisions cause the carriers to suffer random decelerations; the result is a motion at an average speed rather than at a constant acceleration.

The mean carriers speed is given by $v = a\tau_{col}$, where $a = eE/m$ is the acceleration due to the presence of the constant electric field, and τ_{col} is the mean time between collisions, which serves as a relaxation time. The results is that the carriers drift in the direction of the electric field with a mean drift speed $v = e\tau_{col}E/m$, which can written as

$$v = \mu E \tag{2.10}$$

where $\mu = e\tau_{col}/m$ is the carrier mobility.

The motion of the carriers in the device generates a current in its external circuit. To establish the magnitude of the current $i(t)$, we consider an electron-hole pair generated (for example, by absorbtion of a photon) at an arbitrary position x direction in a semiconductor of length W, where a voltage V is applied, as shown in figure 2.7. Now, we consider only the motion in the x direction, and use an energy argument. If a carrier of charge Q (an electron of charge $Q = -e$ or a hole of charge $Q = +e$) moves a distance dx in the time dt, under an electric field of magnitude $E = V/W$, the work is given by

$$-QEdx = -Q\frac{V}{W}dx \tag{2.11}$$

This expression must be equal to the energy provided by the external circuit, $i(t)Vdt$. Thus, we obtain

$$i(t)Vdt = -Q\frac{V}{W}dx \tag{2.12}$$

from which

$$i(t) = -\frac{Q}{W}\frac{dx}{dt} = -\frac{Q}{W}v(t) \tag{2.13}$$

A carrier moving with a drift speed $v(t)$ im the x direction generates a current in the external circuit given by Ramo's theorem

$$i(t) = -\frac{Q}{W}v(t) \tag{2.14}$$

Assuming that the electron moves with speed v_e to the right, and hole moves with speed v_h to the left, from equation [2.14] we obtain that the electron current is

$$i_e = e\frac{v_e}{W} \tag{2.15}$$

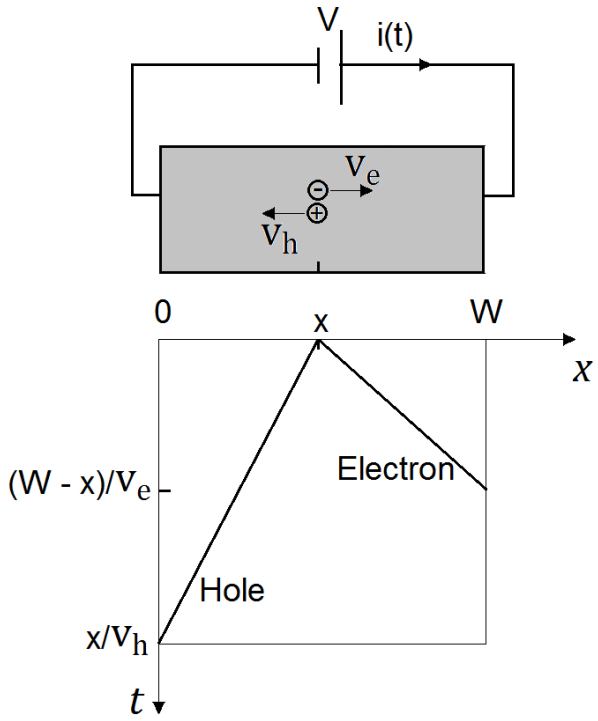

Figure 2.7: *An electron-hole pair is generated at the position x. The electron drifts to the right with speed v_e, and the hole drifts to the left position with speed v_h the process terminates when the carriers reach the electrodes. The total charge induced in the external circuit per carrier pair is e.*

and hole current is

$$i_h = e\frac{v_h}{W} \tag{2.16}$$

Each carrier contributes to the current as long as it is moving. If the carriers continue their motion until they reach the edges of the semiconductor, the electron moves for a time $(W - x)/v_e$ and the hole for a time x/v_h. Generally, in semiconductors $v_e > v_h$, so that the full width of the response is x/v_h. In this way, we define the **transit-time spread** the finite duration of the current. It is an importat limiting factor for speed of operation of all semiconductor photodetectors.

At first glance one may think that the charge observed in the external circuit should be $2e$, because a photon generates an electron-hole pair. But if we calculate the total charge q induced in the external circuit as the sum

of the areas under i_e and i_h we have

$$q = e\frac{v_h}{W}\frac{x}{v_h} + e\frac{v_e}{W}\frac{W-x}{v_e} = e\left(\frac{x}{W} + \frac{W-x}{W}\right) = e \tag{2.17}$$

If we have an uniform charge density ϱ, the total charge in the semiconductor is ϱAW, where A is the cross-section area.

From equation [2.14] we obtain

$$i(t) = -\frac{\varrho AW}{W}v(t) = -\varrho Av(t) \tag{2.18}$$

and now the current density in the x direction is

$$J(t) = \frac{i(t)}{A} = -\varrho v(t) \tag{2.19}$$

The well-known vector form of this equation is

$$\mathcal{J} = \varrho v \tag{2.20}$$

For charge carried by a homogeneous conductive material, $\mathcal{J} = \varrho v$ can be written as

$$i = \frac{\varrho A}{W}EW = \frac{\varrho A}{W}V = GV = \frac{V}{R} \tag{2.21}$$

where G and R are the conductance and the resistance of the material, respectively. This is the well now Ohm's law.

The resistance R and the capacitance C of the photodetector give rise to another response time called RC time constant

$$\tau_{RC} = RC \tag{2.22}$$

The impulse response function in the presence of the transit-time and the RC time-constant spread is determined by convolving the current $i(t)$ with exponential function $(1/RC)exp(-t/RC)$.

It is worthy of note that photodetectors of different types may exhibit other specific limitations on their speeds response, which we consider on a case-by-case basis. As a final point, we mention that photodetectors of a given material and structure often exhibit a fixed gain-bandwidth product. Increasing the gain results in a decrease of the bandwidth, and vice versa. This trade-off between sensitivity and frequency response is associated with the time required for the gain process to take place

2.2.4 Noise

Apart from a large signal, low noise is also important as it will ultimately determine the minimum detectable signal strength. That is why we often speak of signal-to-noise ratio. There are many factors that contribute to noise. The dark current is the leakage current when the photodetector is under bias but not exposed to the light source. One limitation on the device operation is temperature so the thermal energy should be smaller than the photon energy ($kT < h\nu$). Another source of noise is from background radiation, such as black-body radiation from the detector housing at room temperature if not cooled. Internal device noise includes thermal noise (Johnson noise), which is related to the random thermal agitation of carriers in any resistive device. The shot noise is due to the discrete single events of the photoelectric effect, and the statistical fluctuations associated with them. This is especially important for low light intensity. The third is due to flicker noise, otherwise known as $1/f$ noise. This is due to random effects associated with surface traps and generally has l/f characteristics that are more pronounced at low frequencies. The generation-recombination noise comes from the fluctuations of these generation and recombination events. Generation noise can originate from both optical and thermal processes. Since all the noises are independent events, they can be added together as the total noise. A related figure-of-merit is the noise-equivalent power (NEP) that corresponds to the incident rms optical power required to produce a signal-to-noise ratio of one in a 1-Hz bandwidth. At first order, this is the minimum detectable light power. Finally, the detectivity D* is defined as

$$D^* = \frac{\sqrt{AB}}{NEP}\, cmHz^{1/2}/W \tag{2.23}$$

where A is the area and B is the bandwidth. This is also the signal-to-noise ratio when one watt of light power is incident on a detector of area 1 cm^2, and the noise is measured over a l-Hz bandwidth. The parameter is normalized to the area since the device noise is generally proportional to the square root of area. The detectivity depends on the detectors sensitivity, spectral response, and noise. It is a function of wavelength, modulation frequency, and bandwidth, and is recommended to be expressed as $D^*(\lambda, f, B)$.

2.3 Photoconductors

The simplest solid-state photodetector is the photoconductor (or photoresistor), it is a resistor whose resistance decreases with increasing incident light

intensity. It consists of a slab of semiconductor, in bulk or thin-film form, with ohmic contacts affixed to the opposite ends (figure 2.8). When incident

$$i(t)Vdt = -Q(V/W)dx \tag{2.24}$$

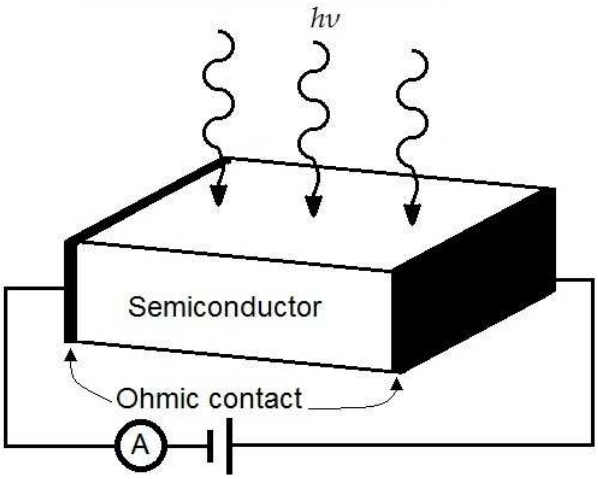

Figure 2.8: *Schematic diagram of a photoconductor and its operation circuit. An ohmic contact is set at each end of the device. In darkness, the photoconductor resistance is high, when a voltage is applied the ammeter shows only a small dark current, when light is incident on the photoconductor, a current flows.*

light falls on the surface of the photoconductor, carriers are generated either by band-to-band transitions (intrinsic) or by transitions involving forbidden gap energy levels (extrinsic), resulting in an increase in conductivity. The processes of intrinsic and extrinsic photoexcitations of carriers are shown in figure 2.9. The wavelength cutoff is given by equation (2.4). For shorter wavelength, the incident radiation is absorbed by the semiconductor and electron-hole pairs are generated.

Assuming a constant photon flux impinging homogeneously on the surface of a photoresistor with area $A = WL$, the number of photons at the surface level is $P_{op}/h\nu$ per unit time (where P_{op} is the incident optical power, and $h\nu$ is the photon energy). At the equilibrium, the carriers generation rate G_e must be equal to the recombination rate. If the thickness D of the photoconductor is much larger than the penetration depth of light $1/\alpha$, so that the total light power is absorbed, the total steady state generation and

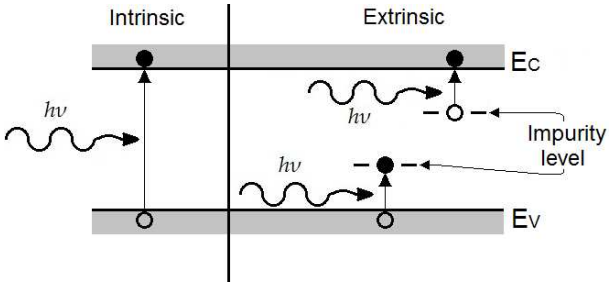

Figure 2.9: *Processes of intrinsic photoexcitation from band to band, and extrinsic photoexcitation between impurity level.*

recombination rates of carriers per unit volume are

$$G_e = \frac{n}{\tau} = \frac{\eta(P_{opt}/h\nu)}{WLD} \tag{2.25}$$

where

- τ is the carrier lifetime,
- η is the quantum efficiency (number of carriers generated per photon),
- n is the excess carrier density.

The carrier lifetime is given by

$$n(t) = n(0)e^{\frac{-t}{\tau}} \tag{2.26}$$

If the photoconductor is made of an intrinsic semiconductor, the photocurrent flowing between the electrodes is given by

$$I_p = \sigma EWD = (\mu_n + \mu_p)nqEWD \tag{2.27}$$

Where E is the electric field inside the photoconductor, and $n = p$. Substituting n of equation 2.25 into equation 2.27, we have

$$I_p = q\left(\eta\frac{Popt}{h\nu}\right)\frac{(\mu_n + \mu_p)\tau E}{L} \tag{2.28}$$

Now, if we define the primary photocurrent in the follow way

$$I_{ph} \equiv q\left(\eta\frac{P_{opt}}{h\nu}\right) \tag{2.29}$$

From equation (2.28) we have the photocurrent gain G_a

$$G_a = \frac{I_p}{I_{ph}} = \frac{(\mu_n + \mu_p)\tau\mathcal{E}}{L} = \tau\left(\frac{1}{t_{rn}} + \frac{1}{t_{rp}}\right) \tag{2.30}$$

where

- t_{rn} = is the electron transit time across the electrodes,
- t_{rp} = is the hole transit time across the electrodes.

The gain is a critical parameter in photoconductors and from equation [2.30] we can see that it depends upon the ratio of carrier lifetimes to the transit time. The gain of a photoconductor ranges from 1 to 10^6. For high gain ($\sim 10^6$), the lifetime should be long $\sim 10^{-3}$; for low gain (~ 1), the lifetime should be $\sim 10^{-8}$. So there is a trade-off between gain and speed.

Now, if we consider an optical signal intensity modulated with the following law

$$P_\omega = P_{opt}\left[1 + me^{j\omega t}\right] \tag{2.31}$$

where

- P_{opt} is the average optical-signal power,
- m is the modulation index,
- ω is the modulation frequency.

The average current Ip arising from the light is given by equation [2.28]. For the modulated optical signal, the rms optical power is $mP_{opt}/\sqrt{2}$ and the rms signal current is given by [14]

$$i_p \simeq \left(\frac{q\eta m P_{opt} G_a}{\sqrt{2}h\nu}\right)\frac{1}{\sqrt{1+\omega^2\tau^2}} \tag{2.32}$$

At low frequencies this equation becomes equation (2.28). On the other hand, at high frequencies the response is proportional to $1/f$.

Referring to the figure 2.10 (where an equivalent circuit for a photoconductor is shown) the conductance G consists of the contributions from the dark current, the average signal current, and the background current. The resulting thermal noise (generated by the thermal agitation of the charge carriers) is given by

$$\left\langle i_G^2 \right\rangle = 4kTGB_w \tag{2.33}$$

where B_w is the bandwidth.

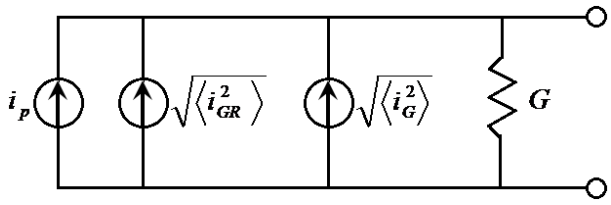

Figure 2.10: *Photoconductor equivalent circuit.*

The shot noise [15] (which originates from the discrete nature of electric charge) is given by

$$\left\langle i_{GR}^2 \right\rangle = \frac{4qI_pB_wG_a}{1+\omega^2\tau^2} \tag{2.34}$$

where Ip is the steady-state light-induced output current.

Now, the signal-to-noise ratio is obtained from equations (2.32), (2.33) and (2.34):

$$\left|\frac{S}{N}\right|_{power} = \frac{i_p^2}{\langle i_G^2\rangle + \langle i_{GR}^2\rangle} = \frac{\eta m^2(P_{opt}/h\nu)}{8B_w}\left[1+\frac{kT}{qG_a}(1+\omega^2\tau^2)\frac{G}{I_p}\right]^{-1} \tag{2.35}$$

The noise-equivalent power (NEP) (i.e., $mP_{opt}\sqrt{2}$) can be obtained from equation (2.35) by setting $S/N = 1$ and $B = 1$. For infrared detectors the most used figure of merit is the detectivity D^* which has been defined by

$$D^* = \frac{\sqrt{AB_w}}{NEP} \tag{2.36}$$

where A is the area and B_w is the bandwidth.

2.4 Photodiodes

Silicon photodiodes are semiconductor devices responsive to charged particles and photons. Photodiodes operate by absorption of photons or charged particles [13] and generate a flow of current in an external circuit, proportional to the incident power. Photodiodes can be used to detect the presence or absence of minute quantities of light and can be calibrated for extremely accurate measurements from intensities below 1 pW/cm^2 to intensities above 100 mW/cm^2. Silicon photodiodes are utilized in such diverse applications as spectroscopy, photography, analytical instrumentation, optical position sensors, beam alignment, surface characterization, laser range finders, optical com- munications, and medical imaging instruments.

A photodiode is a p-n junction similar to a standard diode, except that it must be exposed or packaged with a window to allow light to reach the sensitive part of the device. They are photosensors whose reverse current increases when it absorbs photons.

As mentioned above, this photodetector is designed to operate in reverse bias, and in this condition a depleted region with a high electric field is generated. When a photon of a given energy strikes the diode and reaches the depletion region (figure 2.11), there is a probability (depending on the wavelength) to create an electron-hole pair. Whenever a photon is absorbed, an electron-hole pair is generated, but only where an electric field is present can the charge carriers be separated and transported in a particular direction. If the pair is crated inside the depleted semiconductor region, the high electric field separates the photogenerated electron-hole pair, thus holes move toward the anode, and electrons toward the cathode, and a voltage is produced. Since

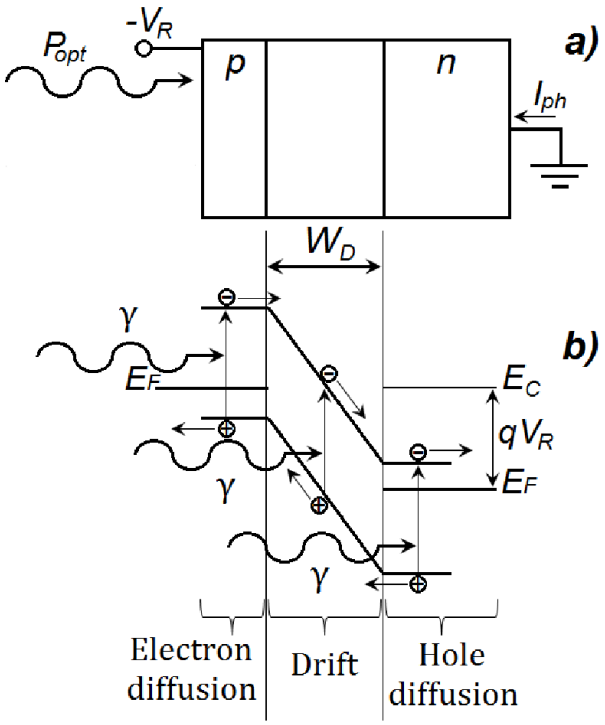

Figure 2.11: *Operation of photodiode. (a) Cross-sectional view of p-n diode. (b) Energy-band diagram under reverse bias and carriers generation.*

a p-n junction has a strong electric field only in the deplation layer, this is the region in which it is desiderable to generate photocarriers.

There are three possible locations where electron-hole pairs can be created:

1. Pairs generated inside the deplation region quickly drift in opposite directions under the influence of the strong electric field. Since the electric field always points from n region to the p region, electrons move to the n side and holes to the p side.

2. Pairs generated outside the deplation region, but in its vicinity, have a probability to entering the depletion region by random diffusion. An electron coming from the p side is quickly transported across the junction and therefore contributes a charge e to the external circuit. A hole coming from the n side has a similar effect.

3. Pairs generated away from the deplation region cannot be transported because of the absence of the electric field. They wander randomly until they are annihilated by recombination. They do not contribute to the signal in the external circuit.

Although these devices are generally faster than photoconductors, they do not exibit gain. The photodiode can be classified as p-n, p-i-n, heterojunction, and metal-semiconductor (Schottky barrier) photodiode.

Current vs voltage characteristics

As a common diode (equation 1.1), a photodiode has a voltamperometric characteristic given by

$$i = i_s \left[e^{\frac{eV}{kT}} - 1 \right] - i_p \tag{2.37}$$

as illustrated in figure 2.12. This is the I-V characteristic of a p-n junction with an added photocurrent $-i_p$ proportional to the photon flux. The voltamperometric characteristic of a Si photodiode in dark state, is similar to the curve of a conventional rectifier diode as shown in figure 2.12. When the photodiode is exposed to the light, the curve at 1 shifts to 2, and increasing the incident light level this characteristic curve shifts to position 3 in parallel.

A photodiode can operate in three modes:

1. open circuit (photovoltaic),

2. short-circuit,

3. reverse biased (photoconductive).

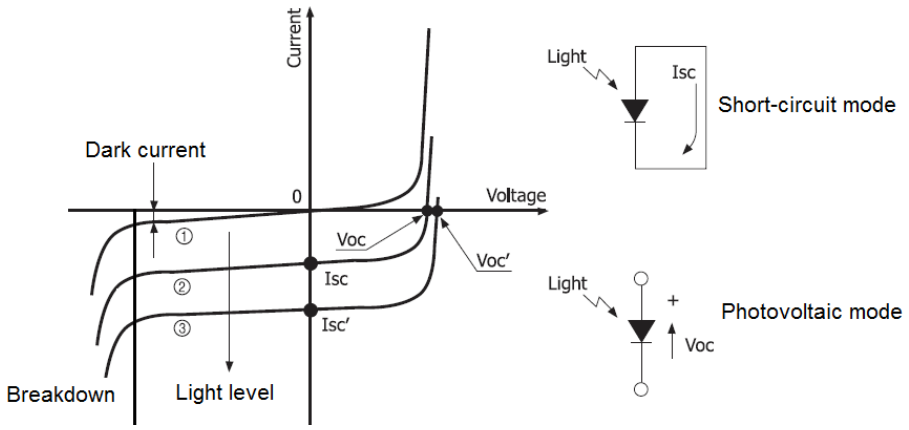

Figure 2.12: *Generic photodiode I-V characteristics. Photovoltaic operation, Short-circuit operation and Reverse-biased operation.*

In the **open-circuit mode** ($I = 0$), the light generates electron-hole pairs in the depletion region. The additional electrons freed on the n side of the layer recombine with holes on the p side, and vice versa. The net result is an increase in the electric field, which produces a photovoltage V_{oc} across the device that increases ($V_{oc'}$) with increasing the photon flux, and $V_{oc'}$ will be generated with the positive polarity at the anode. V_{oc} changes logarithmically with linear changes in the light level. This operation mode is strong temperature dependent, making it unsuitable for measurements of light levels. This mode of operation is used, for example, in solar cells. The responsivity of a photovoltaic photodiode is measured in V/W rather than in A/W.

In the **short-circuit** ($V = 0$) mode the current is simply the photocurrent I_{sc}, which changes linearly respect the light level.

Finally, a photodiode may be operated in its **reverse-biased** ($V < 0$) or "photoconductive" mode,

Spectral response

Quantum efficiency η is the number of electron-hole pairs that can be extracted as photocurrent per incident photons, and the responsivity $\Re$ is the associated physical quantity, which is the ratio of the photocurrent to the optical power, and from equation 2.6 we can express the quantum efficiency with the following relation

$$\eta = \frac{1.24\Re}{\lambda} \ (\mu m) \tag{2.38}$$

Therefore, for a given quantum efficiency, the responsivity increases linearly with wavelength. For an ideal photodiode ($\eta = 1$), $\Re = \lambda/1.24$ (A/W) where λ is expressed in microns. We have seen that the optical absorption coefficient α is a strong function of the wavelength, and so for a given semiconductor the wavelength range in which appreciable photocurrent can be generated is limited. Since most photodiodes use band-to-band photoexcitation (except for photoexcitation over the barrier in metal-semiconductor photodiodes), the long-wavelength cut-off λ_c, is established by the energy gap of the semiconductor, for example about 1.100 μ m for Si and 1.700 μm for Ge. λ_c can be expressed by equation

$$\lambda_c = \frac{1.24}{E_g} \ (\mu m) \tag{2.39}$$

In the case of Si and Ge at room temperature, the cutoff wavelengths are 1.100 μm and 1.88 μm, respectively. For wavelengths longer than λ_c, the values of α are too small to give appreciable absorption.

For short wavelengths the degree of light absorption within the surface diffusion layer becomes very large. In other word, the short-wavelength cutoff of the photoresponse comes about because the values of α are very large ($\leq 10^5$ cm^{-1}), and the radiation is absorbed very near the surface where recombination is more likely. The photocarriers thus recombine before they are collected in the p-n junction. Therefore, the thinner the diffusion layer is and the closer the $p-n$ junction is to the surface, the higher the sensitivity will be. For normal Si photodiodes, the cutoff wavelength in the short wavelength region is 320 nm, whereas it is 190 nm for UV-enhanced Si photodiodes. The cutoff wavelength in the near UV region is also determined by the spectral transmittance of the light input window material, if present. For borosilicate glass and plastic resin coating, wavelengths below about 300 nm are absorbed. If these materials are used as window, the short-wavelength sensitivity will be lost. When detecting wavelengths shorter than 300 nm, Si photodiodes with quartz windows are used. Measurements limited to the visible light region use a visual-sensitive compensation filter that allows only visible light to pass through it.

Figure (5.34) shows spectral responses for various types of Si photodiodes manufactured by Hamamatsu.

In the near-infrared region, silicon photodiodes with antireflection coating can reach 100% quantum efficiency near 0.8 to 0.9 μm. In the 10- to 1.6μm region, germanium photodiodes, III-V ternary photodiodes (e.g., InGaAs), and III-V quaternary photodiodes (e.g., InGaAsP) show high quantum efficiencies. For longer wavelengths, photodiodes are cooled (e.g., 77 K) for high-efficiency operation.

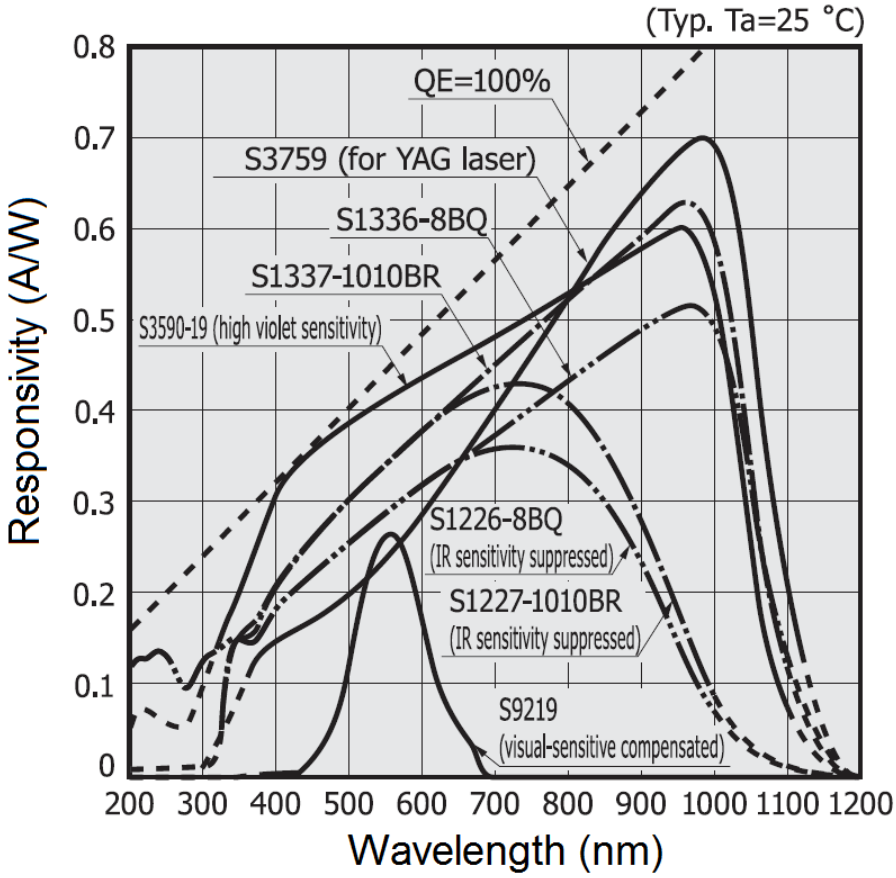

Figure 2.13: *Spectral response versus wavelength for various Si photodiodes. (From Hamamatsu catalog).*

Response time

The response time of a photodiode is a measure of how fast the generated carriers are extracted to an external circuit as output current, and it is generally expressed as the rise time or cutoff frequency. The rise time is the time required for the output signal to change from 10% to 90% of the peak output value. The response time is limited by a combination of three factors:

1. drift time in the depletion region,

2. diffusion of carriers,

3. time constant of terminal capacitance and load resistance.

The drift time in the depletion region is related to the eletctron-hole pairs generated inside the deplation region, and this is the best condition of operation. The transit speed (v_d) at which the carriers travel in the depletion layer is expressed by $v_d = \mu E$, where μ is the carrier traveling rate, and E the avearge electric field in the depletion layer. The average electric field is given by $E = V_R/d$, where V_R is the reverse voltage applied to the junction, and d depletion layer width. Now, the drift time in the depletion region t_{dd} can be approximated by the following equation

$$t_{dd} = \frac{d}{v_d} = \frac{d^2}{\mu v_R} \tag{2.40}$$

To shorten t_{dd}, the distance traveled by carriers should be short or the reverse voltage higher. Since the carrier traveling rate is inversely proportional to the resistivity, t_{dd} becomes slower as the resistivity is increased.

The response time component due to the diffusion of carriers (t_{dc}) is related to the carriers generated outside the depletion layer, but sufficiently close to it. This is a relatively slow process in comparison with drift.

The capacitance of the device C is the sum of the package capacitance and the junction capacitance (Cj). t_{RC} is given by equation

$$t_{RC} = 2.2RC \tag{2.41}$$

where R is the load resistance. To shorten t_{RC}, the design must be such that C and R are made smaller. C is nearly proportional to the active area and inversely proportional to the second to third root of the depletion layer width. Since the depletion layer width is proportional to the product of the reverse voltage and the electrical resistivity (ρ) of the substrate material So, to shorten t_{RC}, a photodiode with a small area and large ρ should be used with an higher reverse voltage. However, this is advisable in cases where t_{RC} is a predominant factor affecting the response speed. Furthermore, applying a higher reverse voltage also increases dark current, so caution is necessary for use in low-light-level detection.

The above three factors determine the rise time of a photodiode. The rise time t_r is approximated by equation

$$t_r = \sqrt{t_{dd}^2 + t_{dc}^2 + t_{RC}^2} \tag{2.42}$$

As can be seen from equation (2.42), the factor that is slowest among the three factors becomes predominant. As stated above, t_{RC} and t_{dd} contain the factors that contradict each other. Making one faster inevitably makes the other slower, so it is essential to create a well-balanced design that matches

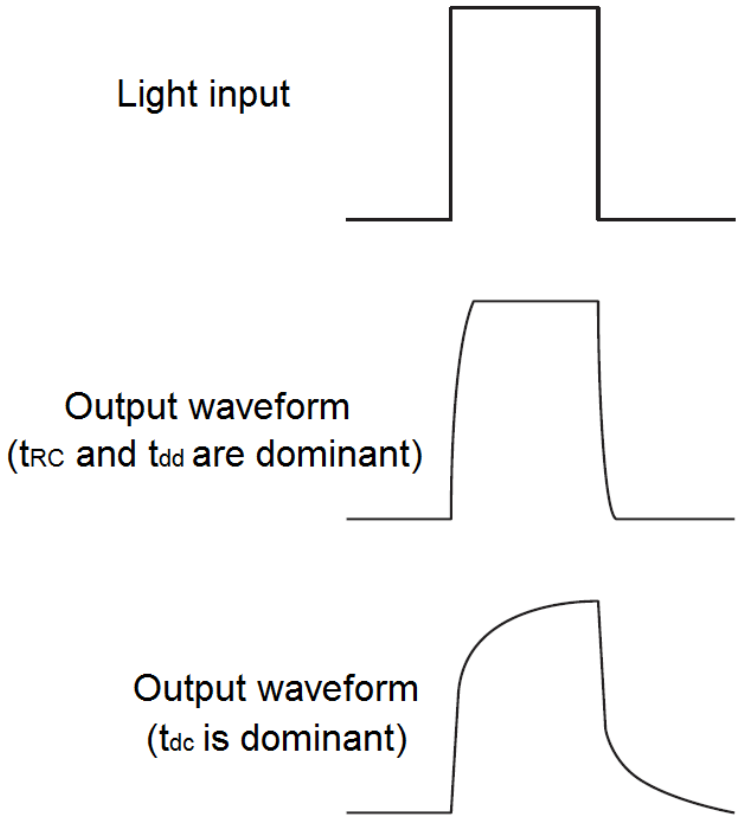

Figure 2.14: *Examples of response waveforms.*

the application. Figure 2.14 shows examples of the response waveforms and frequency characteristic for typical Si photodiodes.

When a photodiode receives sine wave-modulated light emitted from a laser diode, etc., the cutoff frequency f_c is defined as the frequency at which the photodiode output drops by 3 dB relative to the 100% output level which is maintained while the sine wave frequency is increased. This is roughly approximated from the rise time t_r by equation

$$f_c = \frac{0.35}{t_r} \tag{2.43}$$

Noise

Like other types of photosensors, the lower limits of light detection for photodiodes are determined by their noise characteristics. The photodiode noise current I_n is the sum of three main terms

1. the thermal noise current (or Johnson noise current) I_J,
2. the shot noise current I_{SD} resulting from the dark current,
3. the shot noise current I_{SL} resulting from the photocurrent.

Johnson noise is the electronic noise generated by the thermal agitation of the charge carriers inside an electrical conductor at equilibrium, which happens regardless of any applied voltage. Johnson noise is given by

$$I_J = \sqrt{\frac{4kTB_w}{R_{sh}}} \tag{2.44}$$

where k is the Boltzmann's constant, T the photodiode absolute temperature, B_w the bandwidth.

Shot noise consists of additional current fluctuations that occur when a voltage is applied and a macroscopic current starts to flow. When a reverse voltage is applied to the photodiode, there is always a dark current, and so, the shot noise I_{SD} of the dark current is given by

$$I_{SD} = \sqrt{2qI_DB_w} \tag{2.45}$$

where q is the electron charge, ID the dark current. B_w the bandwidth. When a photocurrent I_L is generated by incident light, In this case, the shot noise is given by the following relation

$$I_{SL} = \sqrt{2qI_lB_w} \tag{2.46}$$

At this point, the total photodiode noise current is given by

$$I_n = \sqrt{I_{SL}^2 + I_{SD}^2 + I_J^2} \tag{2.47}$$

The amplitudes of these noise sources are each proportional to the square root of the noise bandwidth so that they are expressed in units of $A/\sqrt{Hz}$ normalized by B_w.

The lower limit of light detection for photodiodes is usually expressed as the intensity of incident light required to generate a current equal to the noise current as expressed in equation (2.44) or (2.45), which is termed the noise equivalent power (NEP)

$$NEP = \frac{I_n}{\Re} \tag{2.48}$$

where $\Re$ is the responsivity.

2.4.1 The p-i-n photodiode

The p-i-n photodiode is a special case of the p-n junction photodiodes, and is one of the most-common photodetectors, because the depletion-region thickness (the intrinsic layer) can be tailored to optimize the quantum efficiency and frequency response. A p-i-n diode is a p-n junction with an intrinsic, usually lightly doped, layer sandwiched between the p and n layers (the "i" layer). This intrinsic structure serves to extend the width of the region supporting an electric field, in effect widening the depletion layer. It may be operated under the variety of bias conditions discussed in the preceding section.

In figure 1.7 the energy-band diagram, charge distribution, and electric field distribution for a p-i-n diode are illustrated.

The p-i-n photodiodes offer several advantages. The increased width of the depletion layer (where the generated carriers can be transported by drift) increases the area available for capturing light. Increasing the width of the depletion layer reduces the junction capacitance and thereby the RC time constant. On the other hand, the transit time increases with the width of the depletion layer. Reducing the ratio between the diffusion length and the drift length of the device results in a greater proportion of the generated current being carried by the faster drift process.

2.5 Avalanche photodiode

An avalanche photodiode (APD) is a solid-state device that generates electron-hole pairs upon exposure to light. An APD operates by converting each detected photon into a cascade of moving carrier pairs. APDs are high-speed, high-sensitivity photodiode that internally multiplies photocurrent. The mechanism by which carriers are generated inside an APD is the same as in a photodiode, but the APD has a function to multiply the generated carriers. Infact, the device is a strongly reverse-biased photodiode in which the junction electric field is large (reverse bias of 100 to 1000 V is placed on the PN junction). The charge carriers therefore accelerate, acquiring enough energy to excite new carriers by the process of impact ionization. When the electrons collide with the crystal lattice, they generate electron-hole pairs. This process cascades, amplifying the initial signal by a factor of 50 or more.

Now, we analyse in detail this process. When electron-hole pairs are generated in the depletion layer of an APD with a reverse voltage applied to the $p-n$ junction, the electric field created across the PN junction causes the electrons to drift toward the $n+$ side and the holes to drift toward the $p+$ side. The drift speed of these electron-hole pairs or carriers depends on the electric

field strength. However, when the electric field is increased, the carriers are more likely to collide with the crystal lattice so that the drift speed of each carrier becomes saturated. If the reverse voltage is increased even further, some carriers that escaped collision with the crystal lattice will have a great deal of energy. When these carriers collide with the crystal lattice, ionization takes place in which electron-hole pairs are newly generated. These electron-hole pairs then create additional electron-hole pairs in a process just like a chain reaction. This is a phenomenon known as **avalanche multiplication**.

The number of electron-hole pairs generated during the time that a carrier moves a unit distance is referred to as the ionization rate. Usually, the ionization rate of electrons is defined as α_e and that of holes as α_h. These ionization rates are important factors in determining the multiplication mechanism. In the case of silicon, the ionization rate of electrons is larger than that of holes, so the electrons contribute more to the multiplication. These ionization rates are important factors in determining the multiplication mechanism. α_e and α_h are called **ionization coefficients**, and they represent the ionization probabilities per unit length (rates of ionization, cm^{-1}); the inverse coefficients, $1/\alpha_e$ and $1/\alpha_h$ represent the average distances between consecutive ionizations. The ionization coefficients increase with the depletion-layer electric field (since it provides the acceleration) and decrease with increasing device temperature. The latter occurs because increasing temperature causes an increase in the frequency of collisions, diminishing the opportunity a carrier has of gaining sufficient energy to ionize. The simple theory considered here assumes that α_e and α_h are constants that are independent of position and carrier history. An important parameter for characterizing the performance of an APD is the **ionization ratio**, which is defined as the ratio of the ionization coefficients

$$\mathcal{K} = \frac{\alpha_h}{\alpha_e} \tag{2.49}$$

In the case of silicon, the ionization rate of electrons is larger than that of holes, so the electrons contribute more to the multiplication, for this reason $\mathcal{K} \ll 1$ The avalanching process then proceeds principally from the p side to the n side. It terminates some time later when all the electrons arrive at the n side of the depletion layer. If electrons and holes both ionize appreciably ($\mathcal{K} \simeq 1$), on the other hand, those holes moving to the left create electrons that move to the right, which, in turn, generate further holes moving to the left, in a possibly unending circulation. Although this feedback process increases the gain of the device (i.e., the total generated charge in the circuit per photocarrier pair q/e), it is nevertheless undesirable for several reasons:

- it is time consuming and therefore reduces the device bandwidth,

- it is random and therefore increases the device noise,
- it can be unstable, thereby causing avalanche breakdown.

It is therefore desirable to fabricate APDs from materials that permit only one type of carrier (either electrons or holes). If electrons have the higher ionization coefficient, for example, optimal behavior is achieved by injecting the electron of a photocarrier pair at the p edge of the depletion layer and by using a material whose value of $\mathcal{K}$ is as low as possible. If holes are injected, the hole of a photocarrier pair should be injected at the n edge of the depletion layer and $\mathcal{K}$ should be as large as possible.

2.5.1 Spectral response

Spectral response characteristics of APDs are almost the same as those of normal photodiodes if a strong reverse voltage is not applied. When a strong reverse voltage is applied, the spectral response curve will change. The depth to which light penetrates in the silicon depends on the wavelength. The depth to which shorter-wavelength light can reach is shallow, so carriers are generated near the surface. In contrast, longer-wavelength light generates carriers at deeper positions. The avalanche multiplication occurs when the carriers pass through the high electric field near the p-n junction. In the case of silicon, the ionization rate of electrons is high, so it must have a structure that injects the electrons to the avalanche layer.

2.6 Silicon photomultiplier

About 1990, russian physicists developed a new type of photon detector [21]. Their idea was to use the binary output of avalanche photodiodes in quenched geiger mode and to arrange them as cells in a matrix with a common anode. They invented what we know today as silicon photomultiplier or SiPM for short. Depending on the manufacturer these devices may be called multi pixel photon counter (MPPC) or geiger mode avalanche photon detector (GAPD). In this text, silicon photomultiplier is used.

SiPMs are photon counting devices made up of multiple small APD pixels (each cell has an area ranging from 20×20 to $100\times100\mu m^2$, see figure 2.15) operated in Geiger mode. Each APD pixel of the SiPM outputs a pulse signal when it detects one photon. The signal output from the SiPM is then the total sum of the outputs from all APD cells.

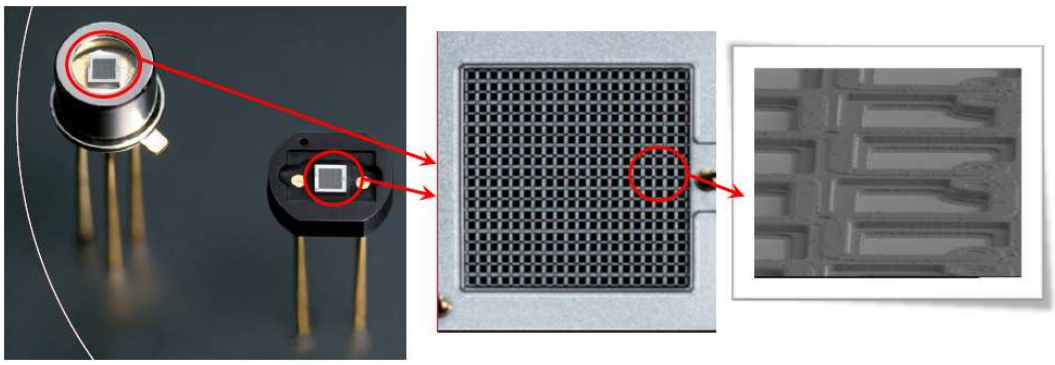

Figure 2.15: *Left, two commercial SiPM with an effective active area of* $1 \times 1mm^2$*; center, the* $1 \times 1mm^2$ *active area; right, close-up view of APD micropixels. (From Hamamatsu catalog).*

Operating principle

When the reverse voltage applied to an APD is set higher than the breakdown voltage (figure 2.16), the internal electric field becomes so high that a huge gain (10^5 to 10^6) can be obtained. Operating an APD under this condition is called "Geiger mode" operation. During Geiger mode, a very large pulse

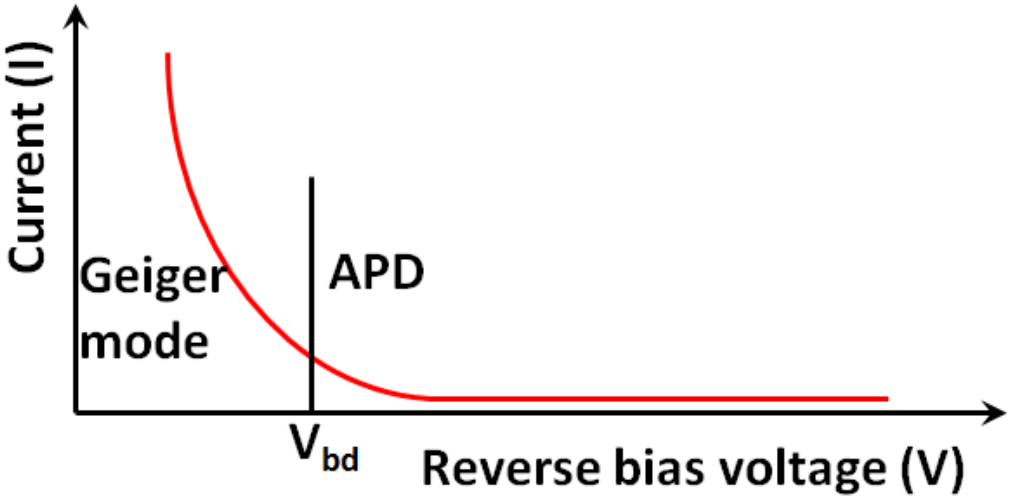

Figure 2.16: *Schematic view of the reverse voltage applied to an APD.*

is generated when a carrier is injected into the avalanche layer by means

of incident photons. One pixel consists of a Geiger mode APD to which a quenching resistor is connected. A SiPM is made up to of an array of these pixels. The output sum from each pixel forms the SiPM output, which allows the photon to be counted.

Each APD micropixel independently works in limited Geiger mode with an applied voltage a few volts above the breakdown voltage (V_{BD}). When a photoelectron is produced, it induces a Geiger avalanche. The avalanche is passively quenched by a resistor integral to each pixel. The output charge Q from a single pixel is independent of the number of produced photoelectrons within the pixel, and can be written as

$$Q = C\dot{(}V_R - V_{BR}) \tag{2.50}$$

where V is the applied voltage and C is the capacitance of the pixel. Combining the output from all the pixels, the total charge from a SiPM is quantized to multiples of Q and proportional to the number of pixels that underwent Geiger discharge ("fired"). The number of fired pixels is proportional to the number of injected photons if the number of photons is small compared to the total number of pixels.

For the SiPM, the operation voltage V is a few volts above the breakdown voltage and well below 100 V.

Theoretically the gain of an avalanche breakdown is infinite. Only the availability of charge carriers limits the charge output. A silicon photomultipier cell with a quenching resistor can be seen as parallel-plate capacitor. When the p-n junction is discharging, the avalanche stops when arriving at the breakdown voltage. Therefore the charge output is given by (2.50). which explains that the charge output is proportional to the reverse bias voltage over the breakdown voltage and the capacitance C of the depleted region. A parallel plate capacitor has a capacitance which is proportional to $C \sim A/d$ The surface area A of a cell is therefore proportional to its gain. Its high field region thickness d is determined by the extent of the depletion zone. The pixel capacitance C is on the order of $10 - 100$fF, giving a gain of $10^5 - 10^6$. These features enable us to read out the signal from the SiPM with simple electronics. In addition, because the thickness of the amplification region is a few μm, it is insensitive to an applied magnetic field and the response is fast.

Photon detection efficiency

In order to measure a photon, three parameters are important in a silicon photomultiplier. First, the photon has to land on the sensitive area, the probability to do so is called geometric efficiency $P_{geometry}$, or fill factor.

Second, the photon excites an electron into the conduction band, creating an electron hole pair, this happens with the quantum efficiency $\eta(\lambda)$ of a single cell. Third, the electron-hole pair induces an avalanche breakdown with the geiger probability $P_{geiger}V_{over}(V,T))$. This probability depends on the relative overvoltage V_{over} which is the voltage above the breakdown voltage $V_{break}(T)$ in units of the bias voltage V

$$V_{over}(V,T) = \frac{V - V_{break}(T)}{V} \tag{2.51}$$

which in turn is strongly dependent on the temperature T. This is why the relative overvoltage of silicon photomultipliers has to be stabilised either thermally or with the operating voltage and a negative feedback. The Geiger probability saturates at about 15% relative overvoltage. It is actually the only parameter which can be changed during operation. All these probabilities are independent and can be multiplied to get the photon detection efficiency PDE

$$PDE = \eta \times P_{geometry} \times P_{geiger} \tag{2.52}$$

Inserting theoretical values for each parameter, one can see that SiPMs potentially achieve photon detection efficiencies of up to 70%. They also achieve a wider spectral sensitivity, which is blue sensitive for the p-on-n type and red sensitive for the n-on-p type. The big challenge is how to produce silicon photomultipliers with such a high photon detection efficiency.

Noise

A **thermal dark rate** in silicon photomultipliers originates from the finite temperature in experimental conditions. Any semiconductor has a certain fraction of electrons in the conduction band for a given temperature T. The occupation of these levels is dependent on the band gap δE_{gap} and obeys Boltzmann statistics

$$P_{conduction} \propto e^{-\frac{\delta E_{gap}}{kT}} \tag{2.53}$$

From this equation it is expected that cooling the SiPM helps reducing the thermal dark rate. In practice, the rate halves roughly every $8K$. Thermally induced electron-hole pairs generate spurious signals.

Afterpulses in SiPMs are pseudo signal pulses following the true signal output pulse. This indicates a phenomenon that produces pulses other than signals when the generated carriers are trapped by crystal defects and then released at a certain time delay. The lower the temperature, the higher the probability that carriers may be trapped by crystal defects, so afterpulses

will increase. Their decay probability $P_{decay}(t)$ in a time dt, depending on the the energy level of the intermediate state ΔE_{trap}, is

$$P_{decay}(t)dt = A\frac{e^{-t/\tau}}{\tau}dt \tag{2.54}$$

where τ is the decay constant given by

$$\tau = Ce^{-\frac{\Delta E_{trap}}{kT}} \tag{2.55}$$

Different intermediate states can be introduced by the doping process. The design of the quenching resistor in advanced designs is such as to delay recharging until after the intermediate states have decayed. By studying the time between pulses, these states may be identified. Unfortunately, equation (2.55) implies that when cooling them to get low thermal dark noise (equation (2.53)), the trap decay constant increases. This increases the probability of afterpulses after recharging the silicon photomultiplier.

For every electron passing through the junction, there is a probability to emit a photon isotropically with an energy higher than the band gap of $\sim 2\times10^5$. Applied to a gain 10^6 device this means that about 20 photons are produced and some of them cause a neighbouring cell to fire. This **optical cross-talk** is a main source of noise in SiPMs. The result is a higher excess noise factor. Cross-talk is triggered by direct photons, by reflections from the bottom of the wafer and by photon induced charge carriers diffusing into neighbouring cells.

2.6.1 Application and comparison with other detectors

Low-light photon detectors constitute the enabling technology for a diverse and rapidly growing range of applications: Nuclear medical imaging, radiation detection, fluorescence analysis, spectroscopy, quality control or meteorology all require detectors that serve to quantify and/or time stamp light signals with anywhere from 1 to about 1000 photons per event. The ideal detector provides a response proportional to the incident photon flux and incorporates an internal gain mechanism, yielding signals of sufficient magnitude to be easily processed. It should offer sub-nanosecond response times and broad spectral sensitivity, be robust, easy to operate and only generate manageable amounts of noise or dark count rates.

Solid state devices have many practical advantages over the PMT, and this led to the PIN diode being used in applications where PMTs were too bulky or delicate, or where high voltages were not possible. However, PIN diodes are severely limited by their complete lack of internal gain. The

Avalanche Photodiode is a more recent technology, an extension of the simple PIN diode. Here the reverse bias is raised to a point where impact ionization allows for some internal multiplication, but is below the breakdown bias where the Geiger mode would take over. In this way, a gain of around a 100 is achieved for a bias of 100-200V. With special manufacture, it is possible for gains of several thousand to be reached using an HV bias of >1500V. Whilst the gain may be lower than that of a PMT, APDs have the advantage of a PDE which can be >65% and also a compact size, ruggedness and insensitivity to magnetic fields. Their main drawbacks are their excess noise (associated with the stochastic APD multiplication process) and in an important trade-off: the capacitance increases with increasing device area and decreasing thickness, whereas the transit times of the charge carriers increase with increasing thickness, implying a performance trade-off between noise and timing. They are limited in size to about 10mm diameter.

The SiPM has high gain and moderate PDE, very similar to the PMT, but has the physical benefits of compactness, ruggedness and magnetic insensitivity in common with the PIN and APD. In addition, the SiPM achieves its high gain (10^6) with very low bias voltages (about 30V) and the noise is almost entirely at the single photon level. Because of the high degree of uniformity between the microcells the SiPM is capable of discriminating the precise number of photoelectrons detected as distinct, discrete levels at the output node. The ability to measure a well resolved photoelectron spectrum is a feature of the SiPM which is generally not possible with PMTs due to the variability in the gain, or excess noise. Despite the fact that the SiPM is sensitive to single photons, its dark count rate of about 100kHz/mm^2 at room temperature renders it unsuitable for use for applications at very low light levels. However, with the application of cooling a two order of magnitude reduction in the dark count rate is readily achievable. the main characteristics of the photodetectors are summarized in Table 2.1.

Summarizing one can say that the SiPM has become widely accepted as a promising photon detector for a wide range of applications.

The SiPM is intrinsically very fast due to very small width of depletion region and extremely short Geiger-type discharge (a few hundreds picoseconds). Therefore, the subnanosecond timing of SiPM together with the other features such as insensitivity to magnetic field, single photoelectron detection with a good signal to noise ratio, good photon detection efficiency in the wide spectral range and position-sensitive (1mm^2) capability look very promising for the application in the field of modern imaging Cherenkov detectors and Time of Propagation (TOP) Cherenkov detector.

A major challenge in the future is the increase of photon detection efficiency over a large range of wavelength (300 nm to 600 nm). Increasing the

	PIN	APD	PMT	SiPM
Gain	1	10^2	10^6	10^6
Operational Bias	Low	High	High	Low
Temp. Sensitivity	Low	High	Low	Medium
Mechanical Robustness	High	Medium	Low	High
Ambient light exposure?	OK	OK	NO	OK
Form factor	Compact	Compact	Bulky	Compact
Large area available?	No	No	Yes	No
Sensitive to magnetic fields?	No	No	Yes	No
Noise	Low	Medium	Low	High
Rise time	Medium	Slow	Fast	Fast

Table 2.1: Photodetectors comparison.

detection efficiency at wavelengths below 400nm seems particularly difficult due to the extreme short absorption lengths of the photons in silicon.

The current stage of development is sufficient for some applications but still far from optimal for applications in which sensors with larger areas paired with much higher photon detection efficiencies especially in the blue wavelength region are required. It should be mentioned that the principle of operation allows the construction of a large variety of configurations in terms of device area, cell size, dead area separation, tuned spectral sensitivity, minimal allowed dark counts, acceptable crosstalk, operation voltage, etc.

Chapter 3

Physics and properties of Carbon Nanotubes

Nanotechnology (sometimes shortened to "nanotech") is the manipulation of matter on a near atomic or molecular scale to produce new structures, materials, and devices. Nanotechnology offers the promise of unprecedented scientific advancement for many sectors (e.g. medicine, consumer products, energy, materials, manufacturing, etc.). Nanotechnology has the power not only to create new technologies, but also to enhance the efficiency of the existing devices. Nano-structures are used to study a range of interesting effects that occur when electrons are confined to very small geometries.

Nanotechnology has emerged at the forefront of science and technology development. Carbon nanotubes (CNTs) are an example of this new technology. Due to their unique combination of electronic, thermal and mechanical properties, the interest of the scientific community in potential applications of CNTs in composites, electronics, computers, sensors, medicine and many other areas has rapidly grown. Indeed, NASA is developing materials using CNTs aiming for space applications, seeking to take advantage of their superior stiffness and strength. It is strongly believed that carbon nanotube based composites could offer strength/weight ratio beyond any material currently available.

Since the discovery of carbon nanotubes, researchers have taken interest in their unique structure and physical properties and this interest is still continuing at present. Most reports on the literature attribute the discovery of these nanometric-sized tubes composed of carbon to the work of Iijima, published in 1991 [7], whereas the SWCNTs concept was first reported in 1993 in two independent papers published by Nature, one by Iijima et al. [8] and the other by Bethune et al. [9]. However, a much older paper, published by Oberlin et al. in 1976 [10], presents a figure illustrating a nanotube,

perhaps a SWCNT, but the authors did not state that it was a nanotube structure.

3.1 Structure and geometric properties

There are different ways of defining the structure of carbon nanotubes. One option is to consider that CNTs may be obtained by rolling a graphene sheet in a specific direction, maintaining the circumference of the cross-section. Since the structure of the CNTs is closely related to graphene, CNTs are frequently labeled in terms of graphene lattice vectors. In addition, the reference to graphene allows the theoretical derivation of many CNTs properties. As shown in figure 3.1, if we start from the graphite, we can see that it is formed by a parallel stacking of two-dimensional planes, called graphene sheets. The

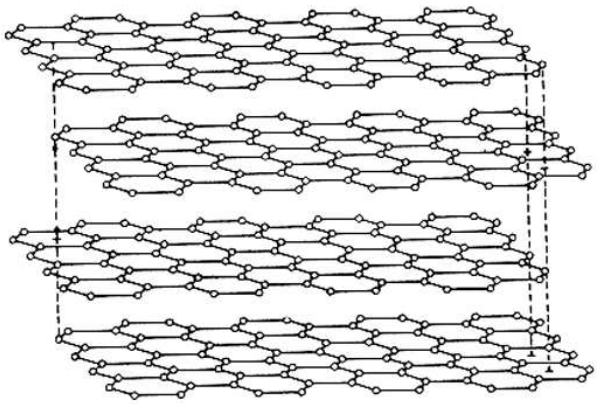

Figure 3.1: *Schematic view of the graphite structure, showing the parallel stacking of two-dimensional planes: the graphene sheets.*

sheets are held together by Van der Waals forces and are separated from each other by a distance of 0.335 nm. Graphene is a single sheet of carbon atoms arranged in a regular hexagonal pattern (figure 3.2).

Graphene is an allotrope of carbon and can be seen as a monolayer of carbon atoms sp2-bonded that are densely packed in a honeycomb crystal lattice. The structural flexibility of graphene is reflected in its electronic properties. The sp^2 hybridization between one s orbital and two p orbitals leads to a trigonal planar structure with a formation of bond between carbon atoms that are separated by 1.42 Å. The band is responsible for the robustness of the lattice structure in all allotropes. Due to the Pauli principle, these bands have a filled shell and, hence, form a deep valence band. The

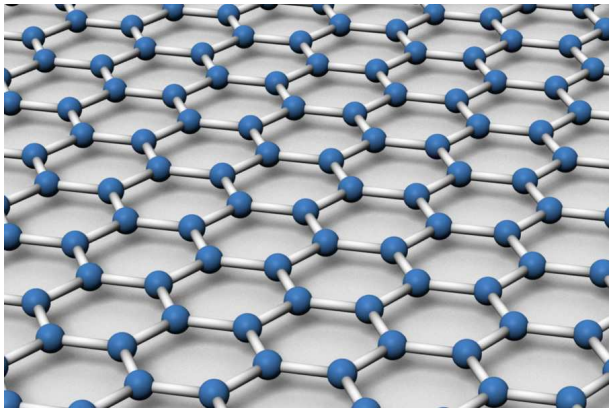

Figure 3.2: *A 3d model of a perfect graphene lattice. Graphene is an atomic-scale honeycomb lattice made of carbon atoms.*

unaffected p orbital, which is perpendicular to the planar structure, can bind covalently with neighboring carbon atoms, leading to the formation of a π band. Since each p orbital has one extra electron, the π band is half filled. Now, an ideal carbon nanotube can be considered as a graphene sheet rolled-up to make a seamless cylinder with a diameter as small as 0.4 nm, length of up to a few centimeters, and half of a fullerene molecule in each extremity, as shown in figure 3.3.

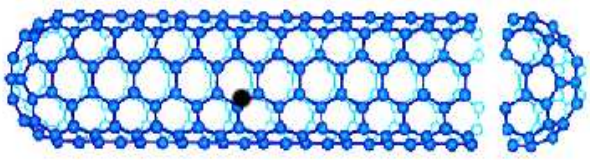

Figure 3.3: *An ideal carbon nanotube.*

The graphene lattice (figure 3.4) is generated by the basis vectors (or lattice vectors)

$$\mathbf{a}_1 = a\left(\sqrt{3}, 0\right) \mathbf{a}_2 = a\left(\frac{\sqrt{3}}{2}, \frac{3}{2}\right) \tag{3.1}$$

where $a = 0.142nm$ is the carbon-carbon bond length. Any point on the lattice can be reached using the combination of the two lattice vectors

$$\mathbf{C}_k = n\mathbf{a}_1 + m\mathbf{a}_2 \tag{3.2}$$

where n and m are integers (they represent the number of steps along the zig-zag carbon bonds of the hexagonal lattice).

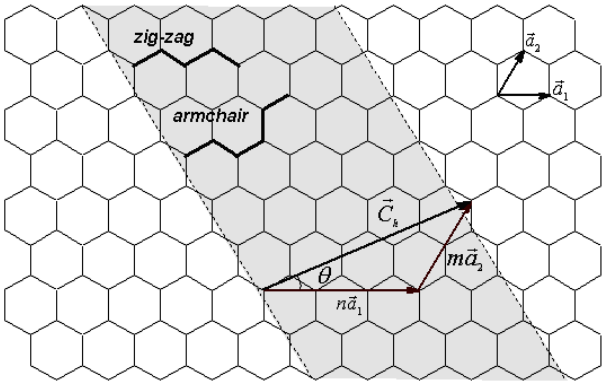

Figure 3.4: *Schematic diagram showing how a hexagonal sheet of graphite is "rolled" to form a carbon nanotube.* a_1 *and bf* a_2 *are the lattice vectors . A wrapping vector* $ma^1 + na^2$ *is shown. The shaded area of graphene will be rolled into a tube so that the wrapping vector encircles the waist of the CNT. The chiral angle is measured between a1 and the wrapping vector.*

The angle θ is called chiral angle, and it determines the degree of "twisting" of the tube. It is defined as the angle between the vectors $\mathbf{C_k}$ and $\mathbf{a_1}$, which varies in the $0° \leq \theta \leq 30°$ range. In terms of the integers (n, m), θ can be described by the set of equations below

$$cos\theta = \frac{2n+m}{2\sqrt{m^2+n^2+nm}} \tag{3.3}$$

$$sin\theta = \frac{\sqrt{3}m}{2\sqrt{m^2+n^2+nm}} \tag{3.4}$$

$$tan\theta = \frac{\sqrt{3}m}{2n+m} \tag{3.5}$$

In cutting the rectangular strip, one defines a circumferential vector

$$\mathbf{C}_k = n\mathbf{a}_1 + m\mathbf{a}_2 \tag{3.6}$$

from which the CNT radius is given by

$$R = \frac{C}{2\pi} = \frac{\sqrt{3}a}{2\pi}\sqrt{m^2+n^2+nm} \tag{3.7}$$

There are many possible CNT geometries, depending on how the graphene sheet is rolled into a cylinder (figure 3.5): when the circumferential vector

lies purely along one of the two basis vectors, the CNT is said to be of the zigzag type; when the circumferential vector is along the direction exactly between the two basis vectors ($n = m$), the CNT is said to be of armchair type. In other word, based on the geometry of the carbon bonds around the circumference of the tube, there are two limiting cases, corresponding to the a chiral tubes, known as armchair with $\theta = 30°$ (it is called armchair because the edge, after rolling, looks like an armchair as shown in figure 3.5, this requires some imagination!) and zig-zag ($\theta = 0°$). In addition, when $0° < \theta < 30°$, the nanotube is called chiral. In terms of the chiral vector, a nanotube is armchair for (n, m) and zigzag for $(n, 0)$. The parameters n, m and θ play important roles in describing the electronic properties of CNTs.

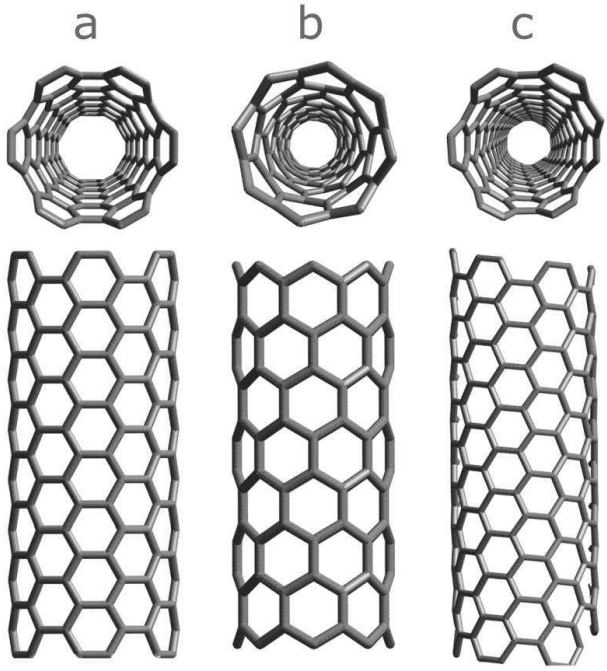

Figure 3.5: *Schematic model of (a) an armchair nanotube, (b) a zig-zag nanotube, and (c) a chiral nanotube.*

Carbon Nanotubes can be categorized in the following way:

- Single-wall Nanotubes (SWCNT);
- Multi-wall Nanotubes (MWCNT).

The previous description applies to SWCNT. Multi-wall nanotubes appear in the form of a coaxial assembly of SWCNT similar to a coaxial cable (figure 3.6). The diameters of MWCNT are typically in the range of $5nm$ to $50nm$. The interlayer distance in MWCNT is close to the distance between graphene layers in graphite. MWCNT are easier to produce in high volume quantities than SWCNT. However, the structure of MWCNT is less understood because of its greater complexity and variety. Regions of structural imperfection may reduce its desirable material properties.

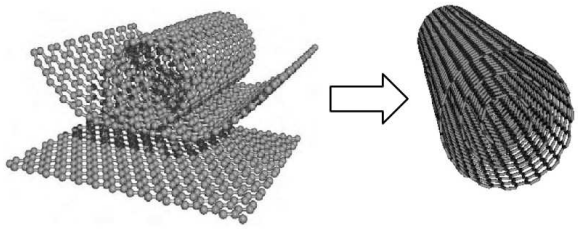

Figure 3.6: *MWNTs are simply several layers of graphite which are then rolled into a cylinder. The layers of graphite form concentric circles if the tube were to be viewed from either end.*

3.2 Electronic properties

In this section we will apply the tight-binding approximation method [1] to a two-dimensional sheet of graphene. From this point of view, a solid, metal or insulator, can be seen as a collection of weakly interacting neutral atoms. The tight-binding approximation deals with the case in which the overlap of atomic wave functions is enough to require corrections to the picture of isolated atoms, but not so much to render the atomic description completely irrilevant. This appoximation is useful for describing the bandstructure that arise from the partially filled d-shells of transition metal atoms and for describing the electronic structure of insulator.

3.2.1 Graphene bandstructure in the tight-binding approximation

The carbon atoms on the surface of a graphene sheet are arranged in a hexagonal pattern (figure 3.7). It can be seen that the structure is not really periodic. Adjacent carbon atoms do not have identical environments. But

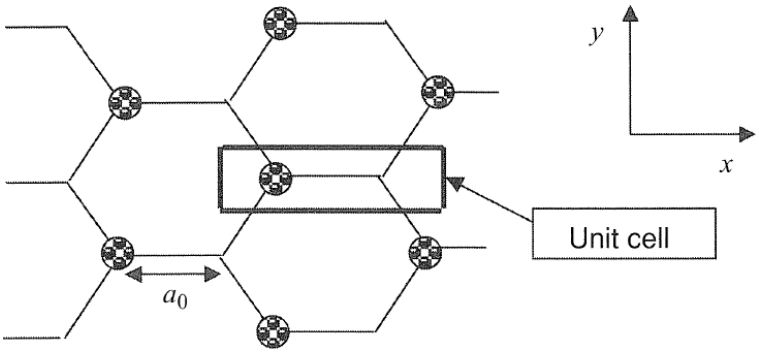

Figure 3.7: *Arrangement of carbon atoms on the surface of graphene, showing the unit cell of two atoms.*

if we lump two atoms together into a unit cell the lattice of unit cells is periodic: every site has the same environment as shown in figure 3.8. We

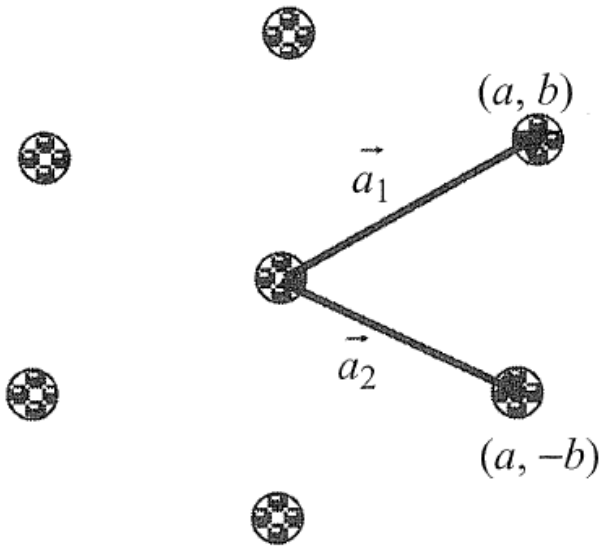

Figure 3.8: *Direct lattice showing the periodic arrangement of unit cells with basis vectors a_1 and a_2.*

have seen that every point on this periodic lattice formed by the unit cells can be described by a set of integers (m, n) where

$$R = ma_1 + na_2 \tag{3.8}$$

with

$$a_1 = xa + yb,\ a_2 = xa - yb \tag{3.9}$$

where

$$a = 3a_0/2,\ and\ b = \sqrt{3}a_0/2 \tag{3.10}$$

The points on the reciprocal lattice in the $k_x - k_y$ plane are given by

$$\mathbf{K} = \mathbf{MA_1} + \mathbf{NA_2} \tag{3.11}$$

Where (M, N) are integers and A_1, A_2 are determined such that

$$\mathbf{A_j} \cdot \mathbf{a_i} = \mathbf{2}\pi\delta_{\mathbf{ij}} \tag{3.12}$$

where δ_{ij} is the Kronecker delta function, equal to one if $i = j$, and equal to zero if $i \neq j$. Equation (3.12) is satisfied by

$$\mathbf{A_1} = \frac{\mathbf{2}\pi(\mathbf{a_2} \times \hat{\mathbf{z}})}{\mathbf{a_1} \cdot (\mathbf{a_2} \times \hat{\mathbf{z}})} = \hat{\mathbf{x}}\left(\frac{\pi}{\mathbf{a}}\right) + \hat{\mathbf{y}}\left(\frac{\pi}{\mathbf{b}}\right) \tag{3.13}$$

$$\mathbf{A_1} = \frac{\mathbf{2}\pi(\hat{\mathbf{z}} \times \mathbf{a_1})}{\mathbf{a_2} \cdot (\hat{\mathbf{z}} \times \mathbf{a_1})} = \hat{\mathbf{x}}\left(\frac{\pi}{\mathbf{a}}\right) - \hat{\mathbf{y}}\left(\frac{\pi}{\mathbf{b}}\right) \tag{3.14}$$

The Brillouin zone for the permitted k-vecotors is then obtained by drawing the perpendicular bisectors of the lines joining the origin $(0, 0)$ to the neighboring points on the reciprocal lattice.

The Brillouin zone tells us the range of k values while the actual discrete values of k have to be obtained from the finite size of the direct lattice. For a given value of k we obtained the corresponding energy eingenvalues from equation

$$E\{\phi_0\} = [h(\mathbf{k})]\{\phi_0\} \tag{3.15}$$

with

$$[h(\mathbf{k})] = \sum_m [H_{nm}] e^{i\mathbf{k}\cdot(\mathbf{d_m} - \mathbf{d_n})} \tag{3.16}$$

The summation over m runs over all neighboring unit cells (including itself) with which cell n has any overlap (that is, for which H_{nm} is non-zero). The size of the matrix $[h(k)]$ depends on the number of basis functions per unit cell. If we use the four valence orbitals of carbon ($2s$, $2p_x$, $2p_y$, $2p_z$) as our basis functions then we will have $4 \times 2 = 8$ basis functions per unit cell (since it contains two carbon atoms) and hence eight eingenvalues for each value of k.

It is found, however, for graphene that the levels involving $2s$, $2p_x$, $2p_y$ orbitals are largely decoupled form those involving $2p_z$ orbitals; in other words, there are non matrix elements coupling these two subspaces. Moreover, the

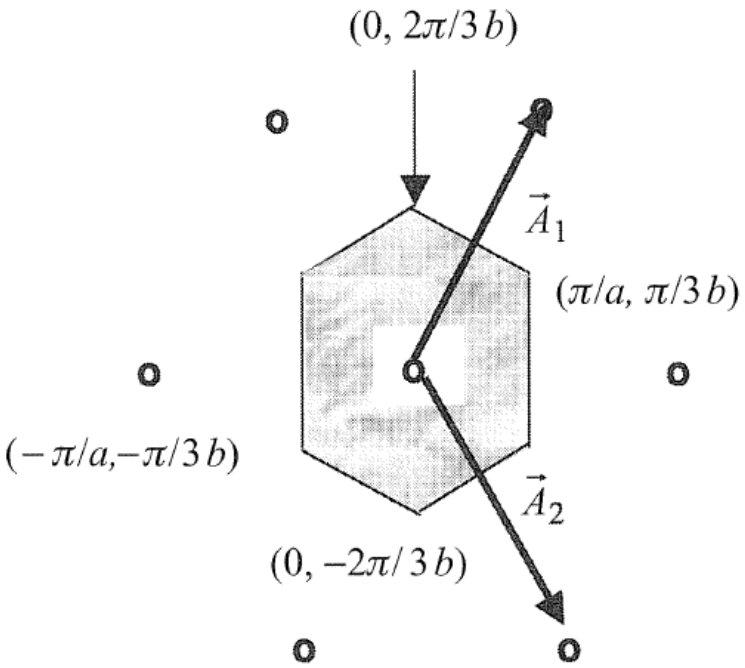

Figure 3.9: *Reciprocal lattice with basis vectros A_1 and A_2. Also the Brillouin zone (shaded) is shown.*

levels involving $2s$, $2p_x$, $2p_y$ orbitals are either far below or far above the Fermi energy, so that the conduction and valence band levels right around the Fermi energy (which are reponsible for electrical conduction) are essentially formed out of the $2p_z$ orbitals. This means that the conduction and valence band states can be described quite well by a theory that uses only one orbital (the $2p_z$ orbital) per carbon atom resulting in a 2×2 matrix $[h(k)]$ that can be written down by summing over any unit cell and all its four neighboring unit cells (the matrix element is assumed equal to $-t$ between neighboring carbon atoms and zero otherwise):

$$\begin{aligned}
[h(\mathbf{k})] &= \begin{bmatrix} 0 & -t \\ -t & 0 \end{bmatrix} + \\
&+ \begin{bmatrix} 0 & -t\,exp(i\mathbf{k}\cdot\mathbf{a_1}) \\ 0 & 0 \end{bmatrix} + \begin{bmatrix} 0 & -t\,exp(i\mathbf{k}\cdot\mathbf{a_2}) \\ 0 & 0 \end{bmatrix} + \\
&+ \begin{bmatrix} 0 & 0 \\ -t\,exp(i\mathbf{k}\cdot\mathbf{a_1}) & 0 \end{bmatrix} + \begin{bmatrix} 0 & 0 \\ -t\,exp(i\mathbf{k}\cdot\mathbf{a_2}) & 0 \end{bmatrix}
\end{aligned} \tag{3.17}$$

Defining

$$h_0 \equiv -t\left(1 + e^{i\mathbf{k}\cdot\mathbf{a_1}} + e^{i\mathbf{k}\cdot\mathbf{a_2}}\right) = -t\left(1 + e^{ik_x a} cosk_y b\right) \tag{3.18}$$

we can write

$$h(\mathbf{k}) = \begin{bmatrix} 0 & h_0 \\ h_0^* & 0 \end{bmatrix} \tag{3.19}$$

so that the eigenvalues are given by

$$E = \pm|h_0| = \pm t\sqrt{1 + 4cosk_y b\, cosk_x a + 4cos^2 k_y b} \tag{3.20}$$

Note that we obtain two eigenvalues (one positive and one negative) for each value of k resulting in two branches in the $E(k)$ plot (figure 3.10). This is

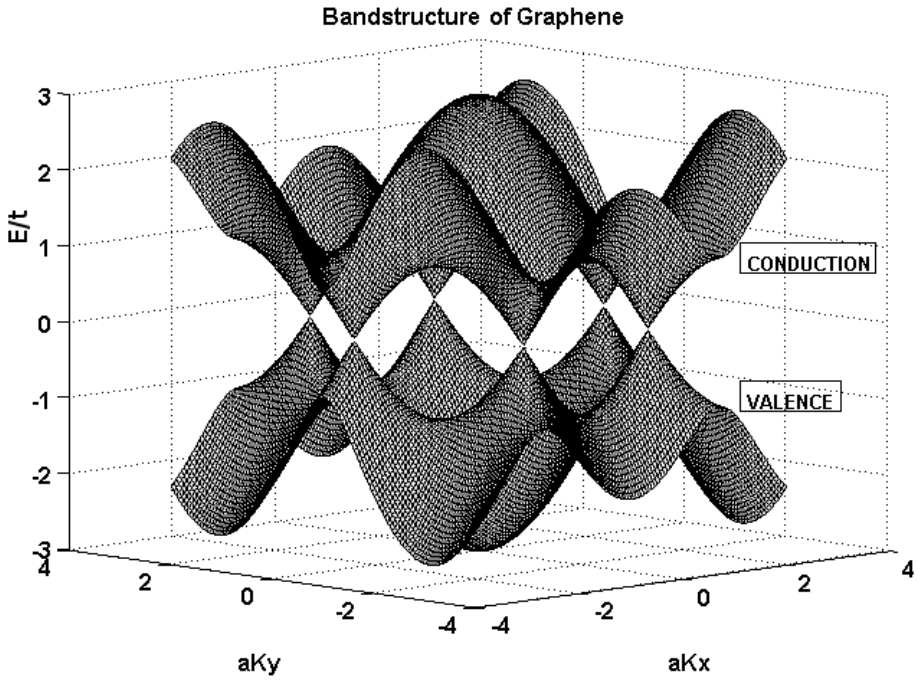

Figure 3.10: *Band structure calculated from tight binding model. The energy of valence and conduction states in graphene plotted as a function of wavevector k. The valence and conduction states meet at singular points in k-space. Dispersion around these points is conical.*

what we expect since we have two basis functions per unit cell. $E(k)$ is called energy dispersion relation.

Energy levels of graphene can be found by diagonalizing the (2×2) matrix (3.19). Since each unit cell has two basis functions, the total number of states is equal tho $2N$, N being the number of unit cells. Each carbon atom contributes one electron to the π-band, giving a total of $2N$ electrons that fill up exactly half the states. Since the energy levels are symmetrically disposed about $E = 0$, this means that all states with $E < 0$ are occupied while all states with $E > 0$ are empty, or equivalently one could say that the Fermi energy is located at $E = 0$. In the $k_x - k_y$ plane these regions with $E = 0$ are located wherever $h_0(k) = 0$. It is easy to see thet this occurs at the six corners of the Brillouin zone:

$$k_x a = 0,\ k_y b = \pm 2\pi/3,\ k_x a = \pi,\ k_y b = \pm\pi/3 \tag{3.21}$$

These six points are special as they provide the states right around the Fermi energy and thus determine the electronic properties. They can be put into two groups of three:

$$(k_x a, k_y b) = (0, -2\pi/3),\ (-\pi, +\pi/3),\ (+\pi, +\pi/3) \tag{3.22}$$

$$(k_x a, k_y b) = (0, +2\pi/3),\ (-\pi, -\pi/3),\ (+\pi, -\pi/3) \tag{3.23}$$

All three within a group are equivalent points since they differ by a reciprocal lattice vector. Each of the six points has one-third of a valley around in within the first Brillouin zone (shared area in figure 3.11). But we can translate these appropriate reciprocal lattice vectors to form two full valleys around two of these points, one from each group:

$$(k_x a, k_y b) = (0, \pm 2\pi/3) \tag{3.24}$$

3.2.2 Bandstructure of CNTs

Once a sheet of graphene is rolled up into a CNT, the allowed values of k are constrained by the imposition of periodic boundary conditions along the circumferential direction. Note that this periodic boundary condition is a real one imposed by the physical structure, rather than a conceptual one used to facilitate the counting of states in a large structure whose exact boundary conditions are unimportatnt. Defining a circumferential vector

$$\mathbf{c} = m\mathbf{a_1} + n\mathbf{a_2} = \hat{x}(m+n)a + \hat{y}(m-n)b \tag{3.25}$$

that joins two equivalent points on the $x-y$ plane that connects to each other on being rolled up, we can express the requirement on periodic boundary condition as

$$\mathbf{k} \cdot \mathbf{c} \equiv k_c|c| = k_x a(m+n) + k_y b(m-n) = 2\pi\nu \tag{3.26}$$

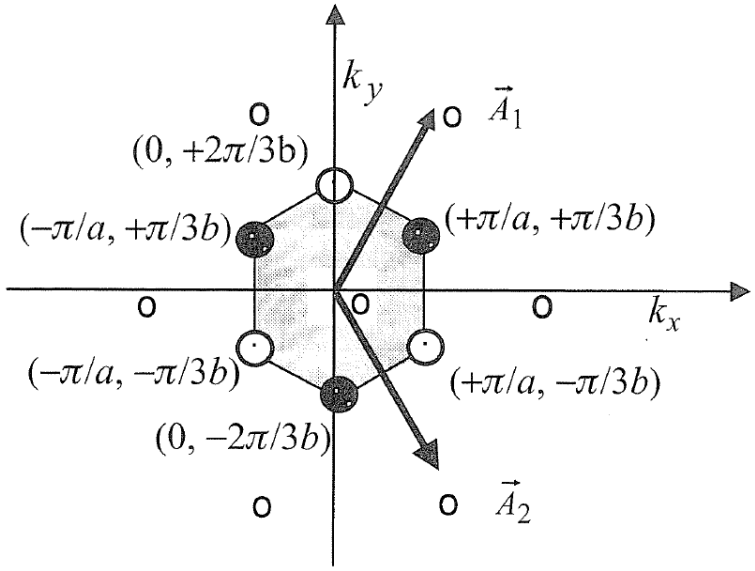

Figure 3.11: *Reciprocal lattice showing Brillouin zone (shaded).*

Which defines a series of parallel lines, each corresponding to a different integer value for ν (figure 3.12).

We can draw a one-dimensional dispersion relation along any of these lines, providing a set of dipersion relations $E_\nu(k)$, one for each sub-band ν.

Whether the resulting sub-band dispersion relations will show an energy gap or not depends on whether one of the lines defined by equation (3.26) passes through the center of the valleys defined in (3.24), where the energy levels lie at $E = 0$. It is easy to see from equation (3.26) that in order for a line to pass through $k_x = 0$, $k_y = 2\pi/3$ we must have

$$(m - n)/3 = \nu \tag{3.27}$$

Since ν is an integer this can only happen if $(m - n)$ is a multiple of three: CNTs satisfying this condition are metallic.

Now we consider a specific example: a CNT with a circumferential vector along the y-direction, $c = y2bm$, which is a zigzag CNT. The periodic boundary condition then requires the allowed values of k lie parallel to the k_x-axis described by (the circumference is $2bm$)

$$k_y 2bm = 2\pi\nu \rightarrow k_y = \frac{2\pi}{3b}\frac{3\nu}{2m} \tag{3.28}$$

as shown in figure 3.13.

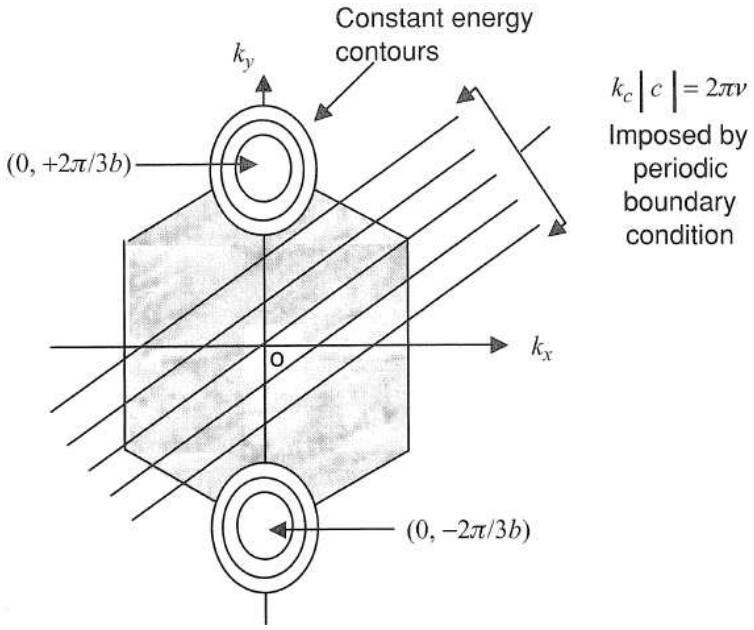

Figure 3.12: *Graphene reciprocal lattice showing straight lines* $k_c|c| = 2\pi\nu$ *representing the constraint imposed by the SWCNT periodic boundary conditions.*

Figures 3.14 and 3.15 show the two "lowest" sub-babds corresponding to values of the sub-band index ν that give rise to the smallest gaps around $E = 0$. If $m = 66$ (a multiple of three), one of the sub-bands will pass through $(k_x a, k_y b) = (0, +-2\pi/3))$ and the dispersion relation for the lowest sub-bands looks as shown in figrure 3.14, with no gap in the energy spectrum. But if $m = 65$ (not a multiple of three), then no sub-bands will pass through $(k_x a, k_y b) = (0, + - 2\pi/3)$ giving rise to a gap in the energy spectrum as shown in figure 3.15.

A CNT with a circumferential vector along the x-direction, $c = x2am$, is armchair. The periodic boundary contition then requires the allowed values of k to lie parallel to the k_y-axis described by (the circumference is again 2bm)

$$k_x 2am = 2\pi\nu \rightarrow k_x = \frac{2\pi\nu}{2ma} \tag{3.29}$$

as shown in figure 3.16.

The sub-band with $\nu = 0$ will always pass through the special point $(k_x a, k_y b) = (0, +-2\pi/3)$ giving rise to dispersion relations that look metallic (figure 3.15) regardless of the value of m.

Electrical conduction is determined by states around the Fermi energy and

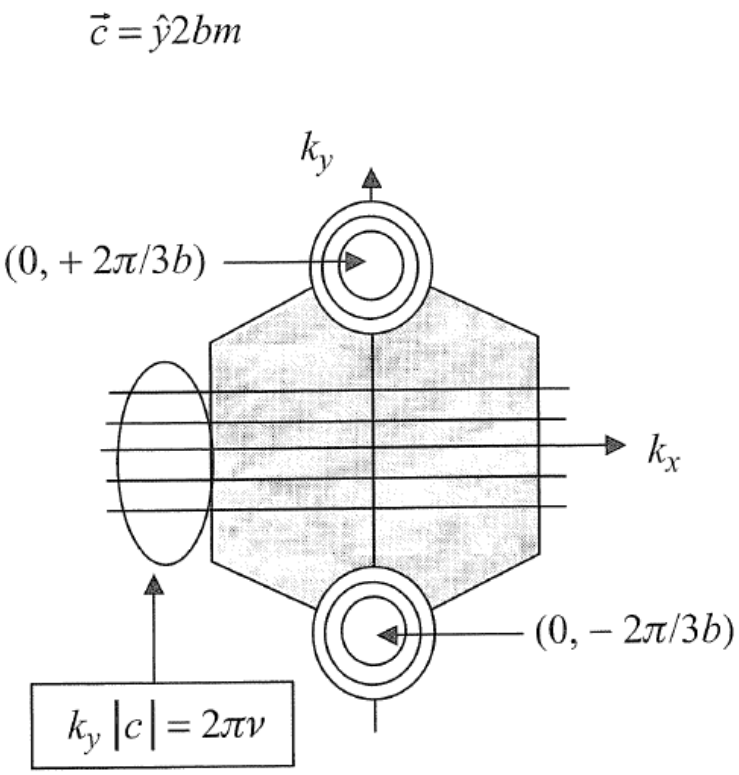

Figure 3.13: *A zigzag CNT has it allowed k-values constrained to lie along a set of lines parallel to the k_x-axis. On of the lines pass though $(0, 2\pi/3b)$ only if m is a multiple of three.*

so it is useful to develop an appoximate relation that describes the regions of the $E-k$ plot around $E=0$. Thus can be done by replacing the expression for $h_0(k) = -t(1+2e^i k_x a cos k_x b)$ with a Taylor expansion around $(k_x a, k_y b) = (0, +-2\pi/3)$ where the energy gap is zero (note that $h_0 = 0$ at these points):

$$h_0 \approx k_x \left[\frac{\partial h_0}{\partial k_x}\right]_{k_x a=0, k_y b=\pm 2\pi/3} + \left(k_y \mp \frac{2\pi}{3b}\right)\left[\frac{\partial h_0}{\partial k_y}\right]_{k_x a=0, k_y b=\pm 2\pi/3} \tag{3.30}$$

It is strainghtforward to evaluate the partial derivates:

$$\frac{\partial h_0}{\partial k_x} = \left[-2iat\ e^{ik_x a} cos k_x b\right]_{k_x a=0, k_y b=\pm 2\pi/3} = iat = i3a_0 t/2 \tag{3.31}$$

$$\frac{\partial h_0}{\partial k_y} = \left[2bt\ e^{ik_x a} sin k_y b\right]_{k_x a=0, k_y b=\pm 2\pi/3} = \pm bt\sqrt{3} = \pm 3a_0 t/2 \tag{3.32}$$

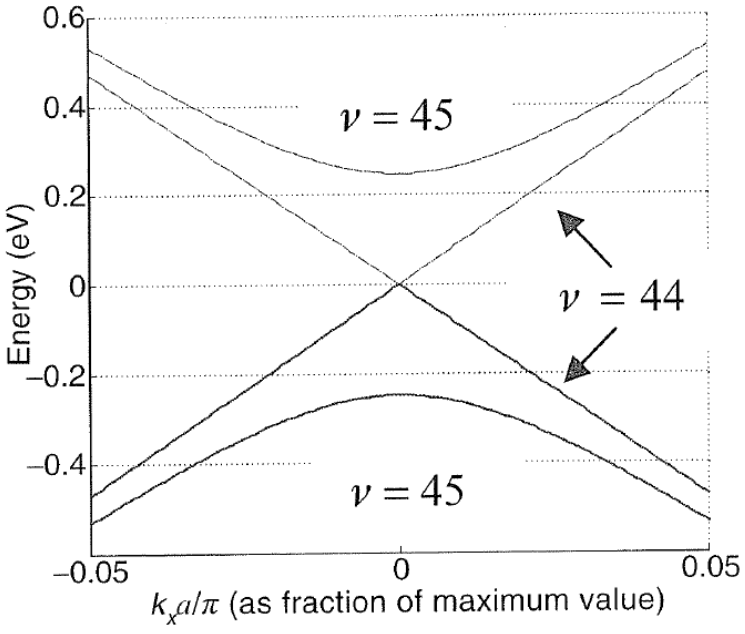

Figure 3.14: *Dispersion relation for the two "lowest" sub-bands of a zigzag CNT showing metalling character (no gap in the energy spectrum).*

So that we can write

$$h_0(\mathbf{k}) \approx i\frac{3a_0 t}{2}(k_x \mp i\beta_y) \tag{3.33}$$

where

$$\beta_y \equiv k_y \mp \frac{2\pi}{3b} \tag{3.34}$$

The corresponding energy dispersion relation (cf. equation (3.20)) can be written as

$$E_k = \pm|h_0| = \pm\frac{3ta_0}{2}\sqrt{k_x^2 + \beta_y^2} \tag{3.35}$$

This simplified approximate relation (obtained from Taylor expansion of equation (3.20) around one of the two valleys) agrees with the exact relation fairly well over a wide range of energies, as is evident from figure 3.17. Within this approximation the constant-energy countours are circles isotropically disposed around the center of each valley , $0, +2\pi/3b$ or $0, -2\pi/3b$. The energy gap of a semiconducting CNT is independent of the specific type of CNT, as long as $(m-n)$ is not a multiple of three so that the gap is not zero. But it is easier to derive an expression for the energy gap if we consider a

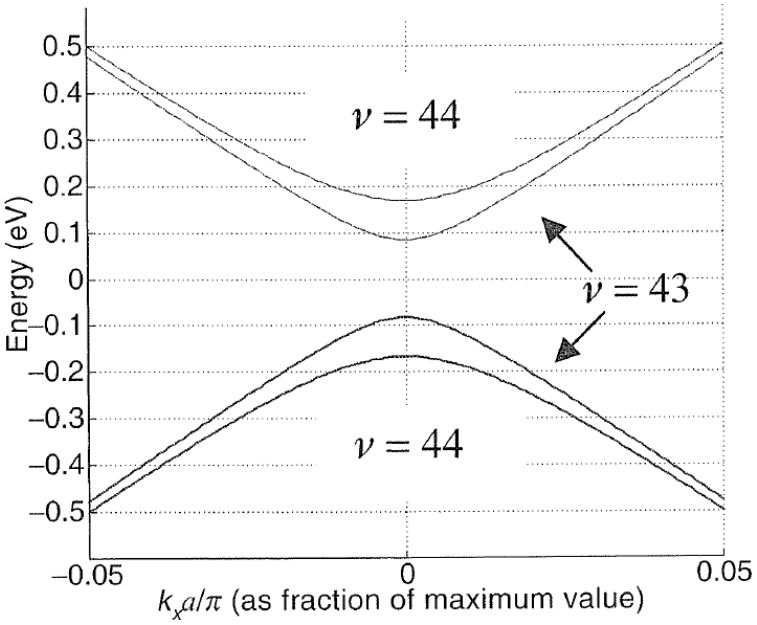

Figure 3.15: *Dispersion relation for the two "lowest" sub-bands of a zigzag CNT showing semiconducting character (gap in the energy spectrum).*

zigzag CNT. From equations (3.28), (3.34) and (3.35) we can write

$$E_{k_x} = \pm\frac{3ta_0}{2}\sqrt{k_x^2 + \left[\frac{2\pi}{3b}\left(\frac{3\nu}{2m} - 1\right)\right]^2} \tag{3.36}$$

So that the energy gap for sub-bands ν can be written as the difference in the energies between the $+$ and $-$ braches at $k_x = 0$:

$$E_{g,\nu} = 3ta_0\frac{2\pi}{2mb}\left(\nu - \frac{2m}{3}\right) \tag{3.37}$$

This has a minimum value of zero corresponding to $\nu = 2m/3$. But if m is not a multiple of three then the minimum value of $(\nu - 2m/3)$ is equal to $1/3$. This means that the minimum energy gap is then given by

$$E_g = ta_0\frac{2\pi}{2mb} = \frac{2ta_0}{d} \approx \frac{0.8eV}{d} \tag{3.38}$$

where d is the diameter of the CNT in nanometers, so that πd is equal to the circumference $2mb$.

$$E_g = ta_0\frac{2\pi}{2mb} = \frac{2ta_0}{d} \approx \frac{0.8eV}{d} \tag{3.39}$$

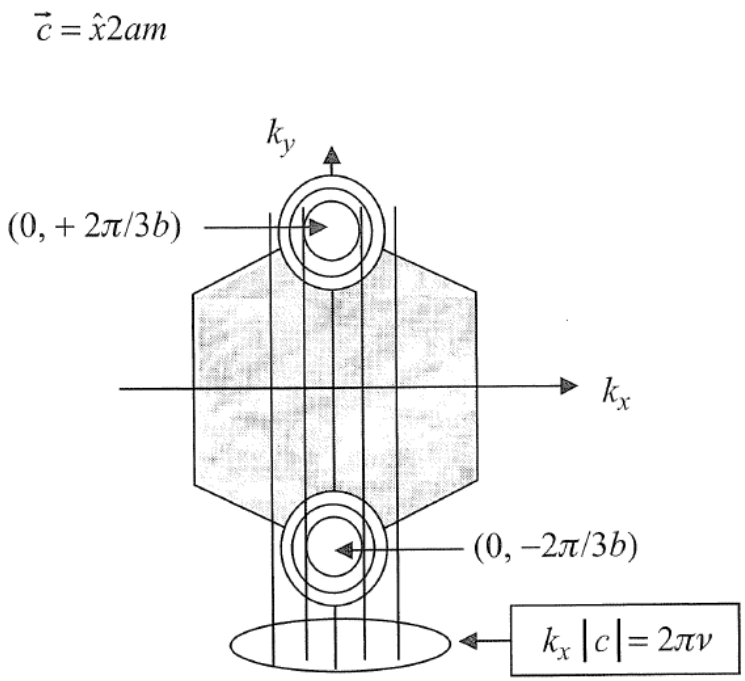

Figure 3.16: *An armachair CNT has its k-values constrained to lie parallel to the k_y-axis. One of the lines will always pass through $(0, 2\pi/3b)$ regardless of the value of m.*

3.2.3 Density of states

The above model is also useful to understand the unusual density of states of CNTs. Density of states tells us the number of energy eigenstates per unit energy range and it depends on the $E(\mathbf{k})$ relationship. The density of states can be expressed as [11]

$$D(E) = \frac{\sqrt{3}a^2}{2\pi R} \sum_i \int dk \delta(k - k_i) \left| \frac{\partial \epsilon}{\partial k} \right|^{-1} \tag{3.40}$$

To understand the basic features of CNTs density of states, one can expand the dispersion relation (3.20) around the Fermi point, this gives

$$D(E) = \frac{a\sqrt{3}}{\pi^2 Rt} \sum_{m=1}^{N} \frac{|E|}{\sqrt{E^2 - \epsilon_m^2}} \tag{3.41}$$

where

- $\epsilon_m = |3m + 1|at/2R$ for semiconducting tubes;

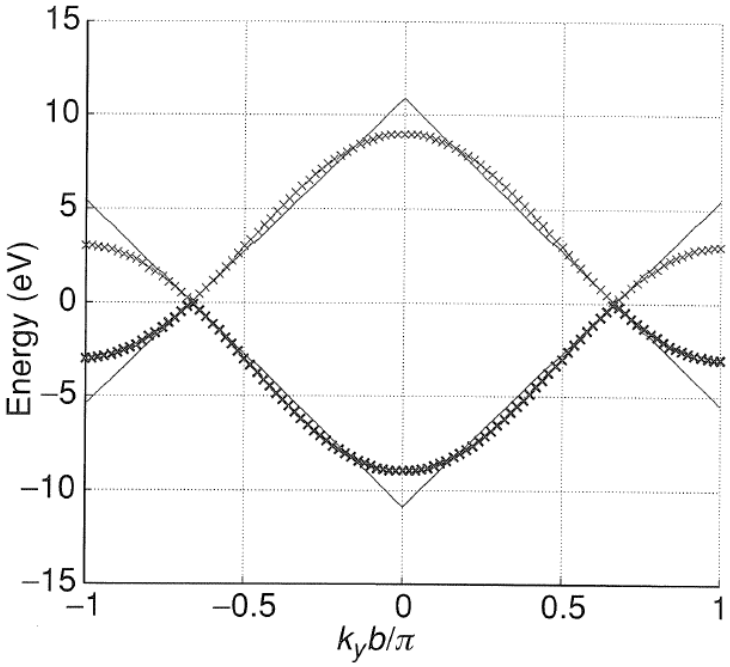

Figure 3.17: *Energy dispersion relation plotted as a function of $k_y b$ along the line $k_x a = 0$. The solid curve is obtained from equation (3.35), while the crosses are obtained from equation (3.20).*

- $\epsilon_m = |3m|at/2R$ for metallic tubes.

In the case of metallic tubes, the $m = 0$ band gives a non-zero density of states at the Fermi level, with $D(E) = (a\sqrt{3})/(2\pi Rt)$. The expression for the density of states shows van Hove singularities when $E = \pm\epsilon_m$, which is indicative of quasi-one-dimensional materials. The presence of these singularities in the density of states has been verified by scanning-tunnelling microscopy of individual nanotubes [12]. Figure 3.18 shows density of states calculated for $(11, 0)$ and $(12, 0)$ nanotubes. The unique feature here is the presence of singularities at the band edges.

A remark on approximations

Finally, it is important to note that there are some deviations in the electronic properties of nanotubes from the simple π-orbital graphene picture described above, due to curvature. As a result of curvature, first, the hopping integrals describing the three bonds between nearest neighbours are not identical and, second, $\sigma - \pi$ hybridization and charge self-consistency become important.

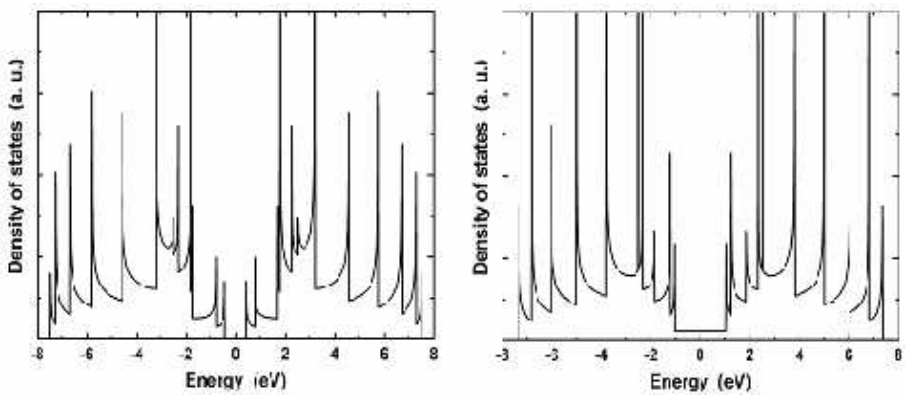

Figure 3.18: *Density of states for (11,0) and (12,0) CNTs computed from tight binding show van Hove singularities.*

Since curvature becomes larger with a decrease in the nanotube diameter, deviations from the simple π-orbital graphene picture become more important in small diameter nanotubes. Nanotubes satisfying $n\ m = 3\nu$ develop a small curvature-induced bandgap and are hence semi-metallic. Armchair nanotubes are an exception because of their special symmetry, and they remain metallic for all diameters. The bandgap of semi-metallic nanotubes is small and varies inversely as the square of nanotube diameter. For example, while a semiconducting nanotube with a diameter of 10 Å has a bandgap of 1eV, a semi-metallic nanotube with a comparable diameter has a bandgap of only 40 meV.

In graphene, hybridization between σ and π orbitals is absent. In contrast, the curvature of a nanotube induces $\sigma - \pi$ hybridization and the resulting changes in long-range interactions. While the influence of $\sigma - \pi$ hybridization in affecting the electronic properties of large diameter nanotubes is negligible, small diameter nanotubes are significantly affected. In general, small diameter nanotubes require a more careful treatment beyond the simple tight-binding graphene model.

3.3 Synthesis

Techniques have been developed to produce nanotubes in sizable quantities, they can be synthesized using different methods, for example arc discharge, laser ablation, chemical vapor deposition (CVD) from hydrocarbons and high pressure conversion of carbon monoxide (HiPco).

Arc discharge and laser ablation methods for the growth of nanotubes

have been actively pursued in the past years. Both methods involve the condensation of carbon atoms generated from evaporation of solid carbon sources. The temperatures involved in these methods are close to the melting temperature of graphite, 3000-4000°C. In arc discharge, carbon atoms are evaporated by plasma of helium gas ignited by high currents passed through opposing carbon anode and cathode. Arc discharge has been developed into an excellent method for producing both high quality multi-walled nanotubes and single-walled nanotubes. MWNTs can be obtained by controlling the growth conditions such as the pressure of inert gas in the discharge chamber and the arcing current. MWNTs produced by arcdischarge are very straight, which is indicative of their high crystallinity. For as grown materials, there are few defects such as pentagons or heptagons existing on the sidewalls of the nanotubes. For the growth of single-walled tubes, a metal catalyst is needed in the arc discharge system. The growth of high quality SWNTs at the 1-10 gram scale is achieved using a laser ablation. The method utilize intense laser pulses to ablate a carbon target containing 0.5 atomic percent of nickel and cobalt. The target is placed in a tube-furnace heated to 1200°C. During laser ablation, a flow of inert gas is passed through the growth chamber to carry the grown nanotubes downstream to be collected on a cold finger.

3.3.1 Chemical vapor deposition technique

Chemical vapor deposition methods have been successful in making carbon fiber, filament and nanotube materials since several years ago. The growth process involves heating a catalyst material to high temperatures in a tube furnace and flowing a hydrocarbon gas through the tube reactor over a period of time. Materials grown over the catalyst are collected upon cooling the system to room temperature. The key parameters in nanotube CVD growth are the types of hydrocarbons, catalysts and growth temperature. The active catalytic species are typically transition-metal nanoparticles that are formed on a support material (the substrate). The general nanotube growth mechanism in a CVD process involves the dissociation of hydrocarbon molecules catalyzed by the transition metal, and dissolution and saturation of carbon atoms in the metal nanoparticle. The precipitation of carbon from the saturated metal particle leads to the formation of tubular carbon solids in sp^2 structure. Tubule formation is favored over other forms of carbon such as graphitic sheets with open edges, this is because a tube contains no dangling bonds and therefore is in a low energy form. For MWNTs growth, most of the CVD methods employ ethylene or acetylene as the carbon feedstock and the growth temperature is typically in the range of 500-750°C. Iron, nickel or cobalt nanoparticles are often used as catalyst. The rational for choosing

these metals as catalyst for CVD growth of nanotubes lies in the phase diagrams for the metals and carbon. At high temperatures, carbon has finite solubility in these metals, which leads to the formation of metal-carbon solutions and therefore the aforementioned growth mechanism. A major pitfall for CVD grown MWNTs has been the high defect densities in their structures. The defective nature of CVD grown MWNTs remains to be thoroughly understood, but is most likely be due to the relatively low growth temperature, which does not provide sufficient thermal energy to anneal nanotubes into perfectly crystalline structures.

For the growth of the layers of MWCNTs on various substrates with different geometry and characteristics, used for the realization of the samples studied in this thesis, the group of University of L'Aquila in charge of this part, used the CVD technique. During the CVD process a substrate is prepared with a layer nickel. The metal nanoparticles can also be produced by other ways, including reduction of oxides or oxides solid solutions. The diameters of the nanotubes that are to be grown are related to the size of the metal particles. This can be controlled by patterned (or masked) deposition of the metal, annealing, or by plasma etching of a metal layer. To initiate the growth of nanotubes, two gases are bled into the reactor: a process gas (such as ammonia, nitrogen or hydrogen) and a carbon-containing gas (such as acetylene, ethylene, ethanol or methane). Nanotubes grow at the sites of the metal catalyst; the carbon-containing gas is broken apart at the surface of the catalyst particle, and the carbon is transported to the edges of the particle, where it forms the nanotubes. This mechanism is still being studied. The catalyst particles can stay at the tips of the growing nanotube during growth, or remain at the nanotube base, depending on the adhesion between the catalyst particle and the substrate.

Usually our MWCNTs are grown as follows, but in some cases these parameters were changed. The MWCNTs have been grown on a substrate of silicon with a thin film of silicon nitride (Si_3N_4) on the surface. A ∼3nm thick-Ni film has been deposited on the substrate by thermal evaporation under a pressure of $\sim 10^{-6}$Torr. In order to form the catalytic particles in the nanometer size the substrate has been pre-treated in NH_3 gas with a flow rate of ∼60sccm[1] for ∼10min at ∼500°C or ∼700°C of temperature. The MWCNTs have been grown on the solid substrate by adding C_2H_2 at a flow rate of ∼20sccm for ∼20min at the same temperature of the NH_3 pre-treatment temperature [26].

Figure 3.19 shows two types of nanostructures grown at different CVD temperatures. On the left side (T = 500°C), the crystalline structure of nan-

[1]Standard cubic centimeter per minute

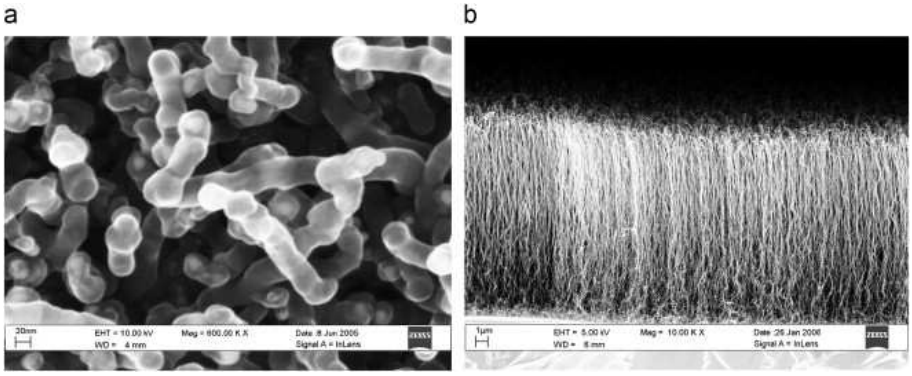

Figure 3.19: *Left: carbon nanofibers grown by CVD at a temperature of 500° C; right: CNT growth at 700° C.(Measurements performed by M. Passacantando).*

otubes is not yet well developed and the tubes look like carbon nanofibers. On the right side (T = 700°C), instead, a clear one-dimensional and crystalline structure is visible. CNTs are well aligned, with uniform density and uniform length of about 20μm.

TEM images carried out by high resolution transmission electron microscopy of both kinds of nanostructures are reported in figure 3.20. Nanotubes

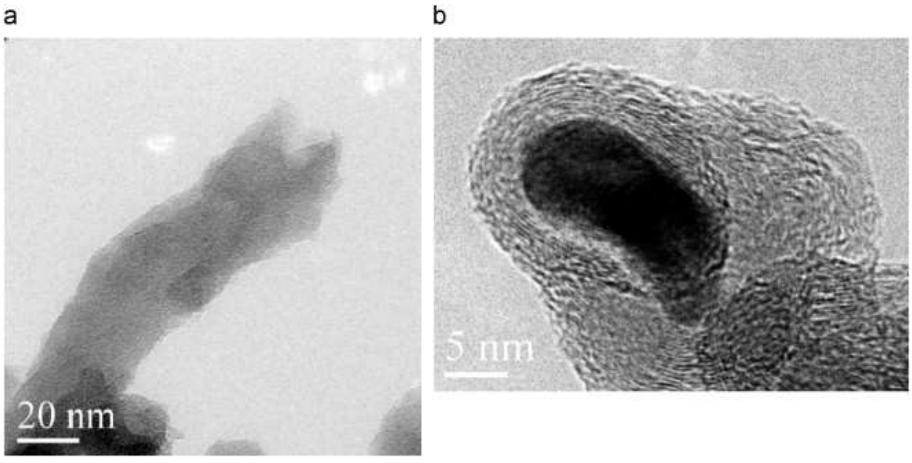

Figure 3.20: *(a) Structure of a 500 °C carbon nanotubes; (b) nickel catalyst particle encapsulated at the apex of the structure. (Measurements performed by P.G. Gucciardi from CNR - IPCF Sezione di Messina and INFN).*

grown at low temperature present an average length of 150nm, a diameter

of tens nanometers and a round edge of 20-30nm. The structure is more similar to a filled cylinder than to a tube, with the external shell not well graphitized. Nickel particles used as catalyst appear to be encapsulated close to the apex of the structure. At 700°C temperature, the CVD process produces nanotubes of very different kinds. Their structure is well defined as a multiwall made in average of 10-15 tubes, with an inner diameter of 5-10nm, an outer diameter ranging from 15 to 25nm (figure 3.21a and b) and a length of tens of micron. Several tubes look bended. Inclusions of particles are also present (figure 3.21c). Most of them are uncapped (figure 3.21d).

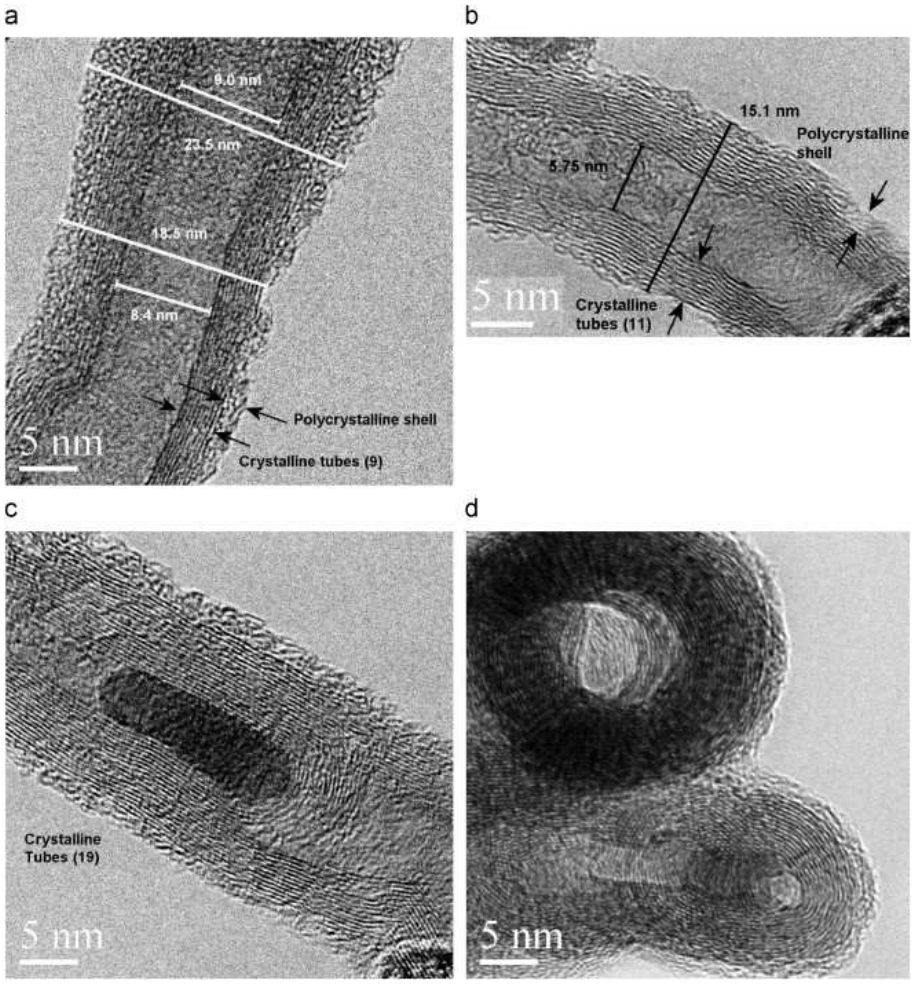

Figure 3.21: *TEM images of MWCNTs. (Measurements performed by P.G. Gucciardi from CNR - IPCF Sezione di Messina and INFN).*

Chapter 4

Carbon nanostructures based photodetectors

The birth of the field of carbon nanotubes is marked by the publication by Iijima of the observation of multi-walled nanotubes with outer diameters as small as 55Å, and inner diameters as small as 23Å, and a nanotube consisting of only two coaxial cylinders [7]. Since this discovery, CNTs unusual characteristics due to the particular geometry have been intensively investigated everywhere in several research laboratories in the world, and a lot of papers have been published on their properties.

From the point of view of photodetection, semiconducting nanotubes show interesting optoelectronic properties in the region of near-to-mid infrared [22]. We have seen in chapter 3 that due to their quasi-one-dimensional geometry, the energy gap of a SWCNT is a function of the diameter, approximately given by the relationship: $E_{gap} = \frac{a}{d}$, where $a = 0.0284eV\ nm$ and d is the diameter in nm. This implies that for the SWCNTs, with diameter ranging from 1 to 2nm, the fundamental gap ranging from 0.4 to 0.7eV, corresponding to a wavelength range from 1.5 to 3μm.

CNTs sensitivity to radiation has been studied by various authors [28] [29] who measured a variation in the nanotubes conductivity when illuminated with IR radiation. Photoconductivity of individual, ropes and films of CNTs has been also investigated in the visible [30] and IR [35] spectral regions. Photon induced charge carrier generation in single wall carbon nanotubes and subsequent charge separation across the metal carbon nanotube contacts is believed to cause the photoconductivity variations [30]. Measurements in the UV region are still missing.

In the case of MWCNTs, optoelectronic properties have not been well understood. A multiwall carbon nanotube can be supposed to be constituted of many SWCNTs and the result is a material still one-dimensional but without

a precise chirality. This means that a single MWCNT covers a wide range of energy levels, up to 3eV with all kinds of metallic and semiconducting characteristics [25] [22]. So, there is the possibility that a layer of multiwall carbon nanotubes can cover a wide range of diameters and chiralities, offering a photocathode sensitive to a large range of wavelength.

In the first part of the chapter some characteristics of five photodetectors realized whith a layer of carbon nanostructures grown on a silicon substrate are shown. This work has been carried out in the framework of the SinPhoNIA (Single Photon Nanotechnology Innovative Approach) experiment first [26] [27], and continued by the PARIDE (Pixel Array for Radiation Imaging DEtector) experiment.

The second part of the chapter will be dedicated to results obtained when an electrically conductive coating layer is applied to carbon nanostructures films to avoid nanostructures detachment from the silicon substrate and uniformly transmit the electric field to the entire active surface.

Finally, the last part of the chapter will be dedicated to a modeling and simulation study. Two photodetectors will be analyzed. These two photodetectors have been modelled and simulated in order to understand the main parameters that characterize their performances. In order to simulate the devices behavior, we started with an equivalent circuit: once the parameter values are fixed we are able to reproduce the current-voltage characteristics, both in dark conditions and under illumination for different light intensities.

4.1 Experimental setup

In order to investigate the basic characteristics of photodetectors we equipped a measurement system (Figure 4.1) with LED lasers emitting at various wavelengths (378, 405, 532, 650, 685, 785, 808, 880, 980nm), with a diameter spot of about 0.5mm. The laser light power intensity (proportional to the number of photons) was electronically controlled and measured with a calibrated photodiode. Measurements were performed by varying the laser power from 0.1mW to 1.0mW with a step of 0.1mW. The volt-amperometric characterization was measured with a Keithley 2635 Source Meter.

The system operated under computerized control, in order to easily communicate with the instrumentation. The control software has been developed using a visual programming language. For this scope, LabVIEW (short for Laboratory Virtual Instrument Engineering Workbench) programs have been employed for data acquisition, instrument control, real time control and data storage. Data were stored in ASCII format and then analysed (depending on the complexity of the analysis to be performed) with Origin, Matlab or Root.

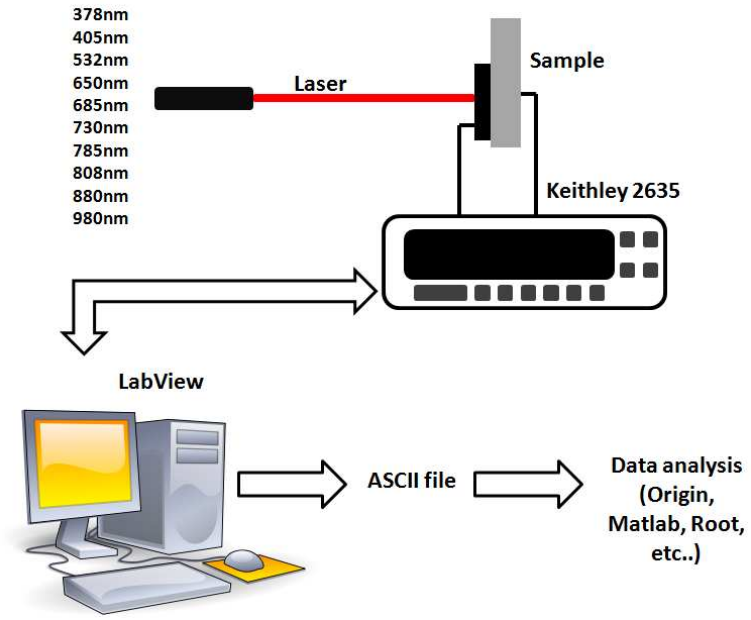

Figure 4.1: *Experimental setup.*

4.2 The substrate

In the next sections we will discuss features of five films of carbon nanostructures grown on substrates having the same characteristics. As mentioned in Section 3.3, carbon nanostructures films, in our case, are grown by means of CVD technique on substrates of particular materials and geometric shapes. For samples analyzed in this chapter, the geometric shape and materials of the substrate are shown in Figure 4.2. The substrate is formed by n-doped silicon with a doping concentration of about 10^{14}cm^{-3}, and a size of $5\times7.8\text{mm}^2$ with a thickness of 500μm. On the top and on the bottom a layer of 140nm of stoichiometric Silicon Nitride (Si_3N_4) is deposited. On the top side, two squares of $1\text{x}1\text{mm}^2$ gold-platinum (Au-Pt) electrodes of 50nm of thickness have been sputtered, on the bottom side the same conducting material covers the surface. In particular, the structure on the back side of the substrate appears to be a metal insulator semiconductor (MIS) junction.

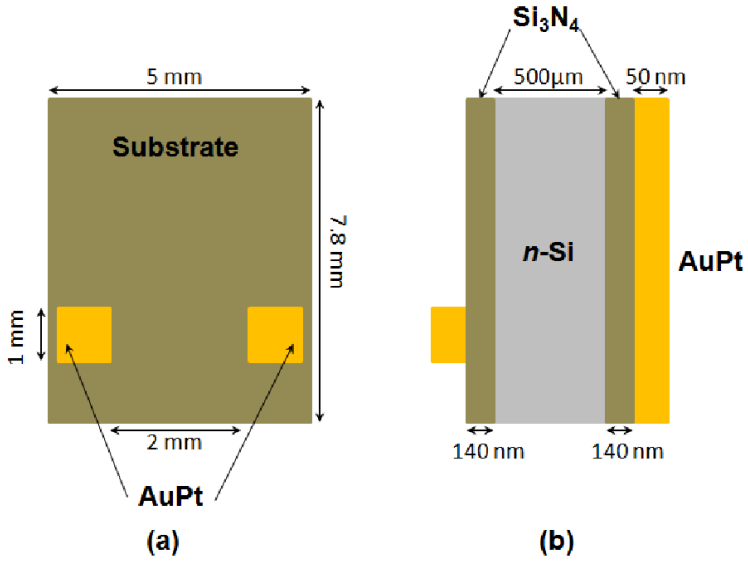

Figure 4.2: *Substrate (a) top and (b) cross-sectional view (not in scale).*

4.3 Sample with carbon nanofibers (Samples C1 and C2)

In this section we report on the main characteristics of two samples with nanostructures grown at the CVD temperature of 500°C. At this CVD temperature we obtain carbon nanofibers (CNFs) as shown in Figure 3.19a. These two samples with nanofibers are called Sample C1 and C2.

In Figure 4.3 is schematized the sample with the film of nanofibers. CNFs film covers an area of about 5x5mm^2 (CNFs are represented by the rectangle in black). CNFs are in electrical contact with the electrodes, in yellow, implanted on the top side of the substrate.

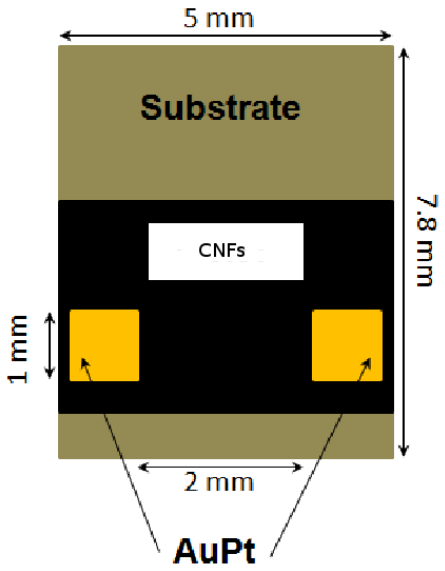

Figure 4.3: *Sample C1 and C2 top view. The rectangle in black represents the CNFs film.*

Electrical measurements have been done applying an electric field with the top-side electrodes at ground, as illustrated in the sketch of figure 4.4. Since nanofibers present an electrical conductivity, we assume that the whole film of CNFs is placed at zero potential with respect to the back of the substrate.

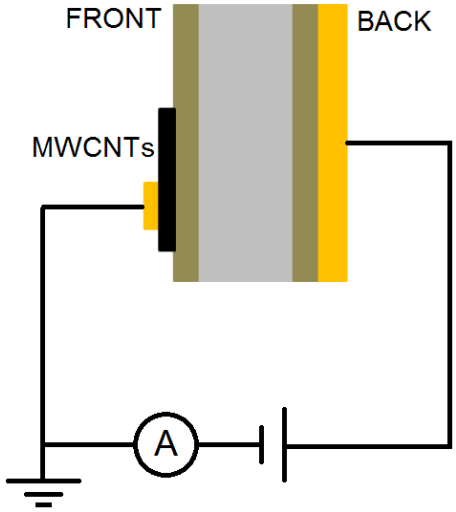

Figure 4.4: *Applied electric field (not in scale sectional view).*

4.3.1 Dark current

Dark currents of Samples C1 and C2 for different bias offsets at room temperature are presented. Dark current is the electric current that flows through photodetectors even when no light is shining on it. Figure 4.5 shows the typical dark currents of Samples C1 and C2 as a function of bias voltage.

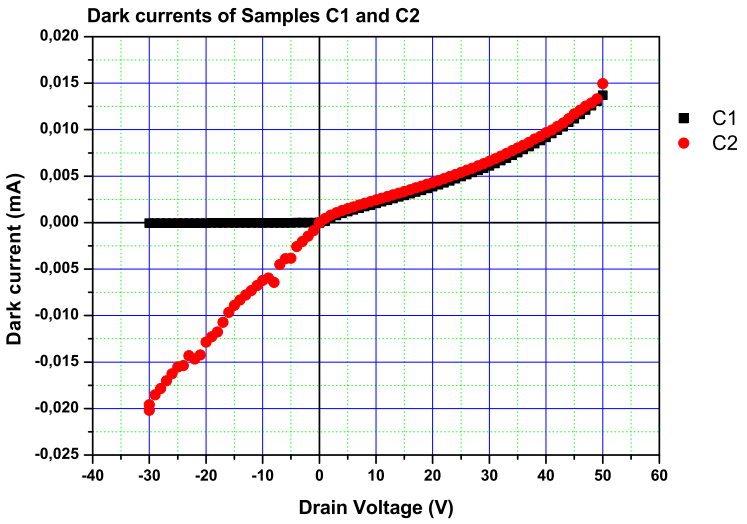

Figure 4.5: *The very high dark currents of samples C1 and C2.*

4.3.2 Photocurrent

The photocurrent generated by devices has been investigated when irradiated by a monochromatic electromagnetic field at different wavelength and subject to a step-like electrostatic potential. Figures 4.6a and b show responses at 650nm continuous light and ten power intensities of samples C1 and C2, respectively.

The effective photocurrent has been obtained subtracting the dark current from the measured current (figure 4.7a and b). From the last two figures we note that as the applied voltage increases, the current is almost zero until few volts, then it increases reaching a saturation region. The threshold voltage when the current begins to be constant depends on the power light intensity, therefore by the number of charges generated into the device under illumination. The plateau region remains constant over a wide range of voltages. Other samples have shown the breakdown limit around a drain voltage of 100V. On the other hand, as the light power intensity increases, a higher drain voltage is necessary to collect all the charges at saturation. These volt-amperometric characteristics under illumination are similar to those of photodiodes.

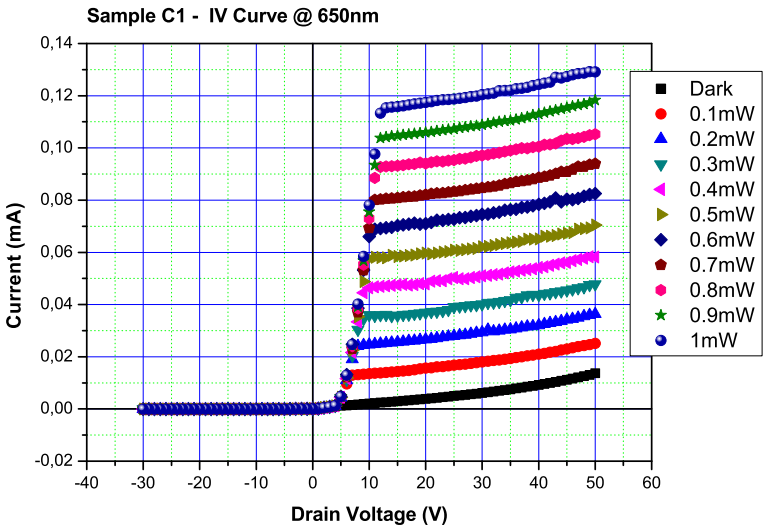

(a)

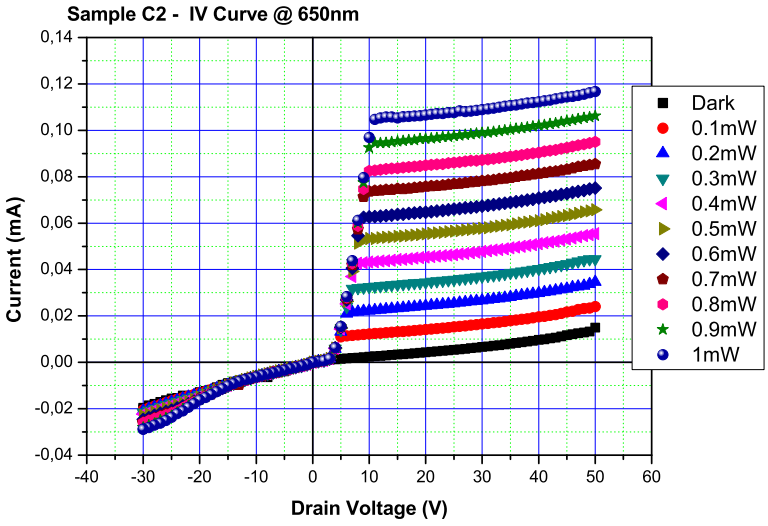

(b)

Figure 4.6: I-V charactristics of Samples C1 (a) and C2 (b) at different light intensities.

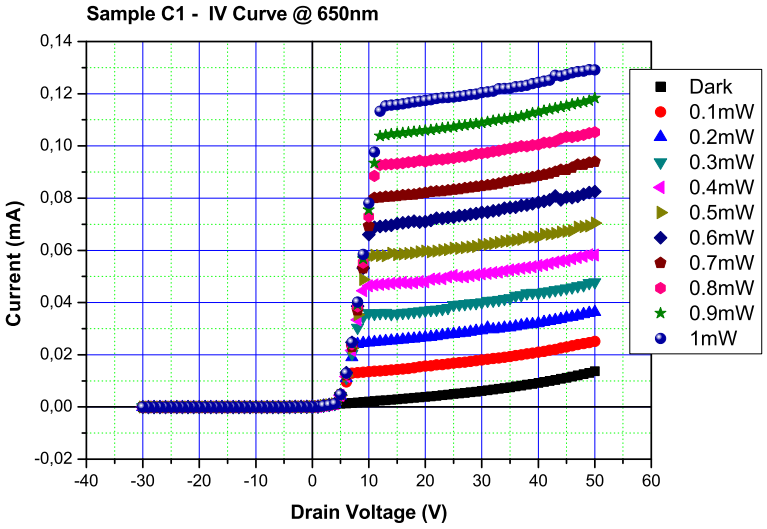

(a)

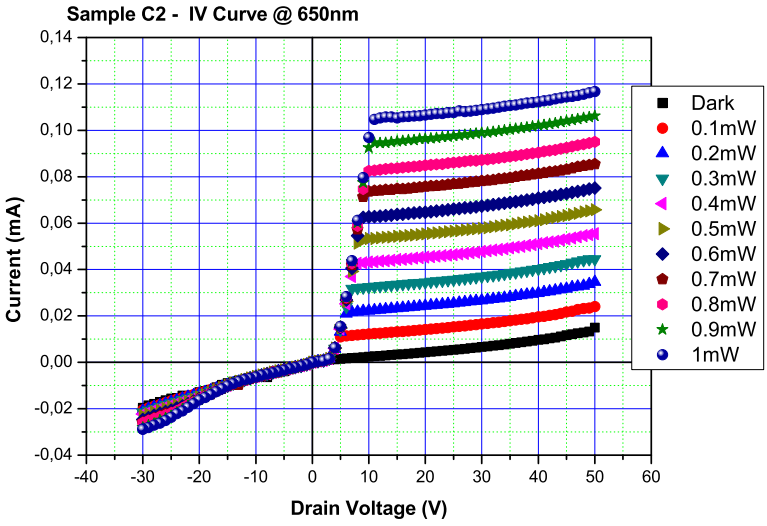

(b)

Figure 4.7: I-V charactristics of Samples C1 (a) and C2 (b) with subtracted dark current.

4.3.3 Linearity

Photodetectors are used for measurements in various branches of industry and research, and usually the assumption is made that they have a linear response with respect to optical power. This assumption greatly simplifies the use of these devices, as the results of characterization measurements at one power level can be extended to other power levels. In some of the more advanced applications, the requirements for measurement accuracy are so demanding that the validity of the assumed linear response must be experimentally verified. A photodetector is defined to be linear when the photoelectric conversion efficiency, the responsivity or quantum efficiency, is constant at a fixed wavelength, so independent on the incident optical power. A typical high-quality pn junction has a constant responsivity, related to quantum efficiency, up to a certain power level, above which the responsivity decreases with increasing optical power. The nonlinearity of a pn junction is a function of several parameters. Obviously, the linearity of the responsivity depends on the generated photocurrent itself, and thus also on the incident optical power. The diameter of the incident beam has been observed to affect the linearity, but in a different manner for various types of photodiodes [31]. For visible wavelengths the linearity of pn junction is wavelength independent, it depends on the photocurrent only [32], [33]. The series resistance over the pn-junction, inversely proportional to the size of the active area, largely determines the saturation current, and thus the limit of the linearity for a pn junction [34].

The correlation between the current at saturation versus the light power intensity is reported in figures 4.8a and b for Samples C1 and C2, respectively. For both detectors the measurement was performed at the fixed voltage of 25V. As can be seen from fit parameters reported in figures, both detectors exhibit good linearity

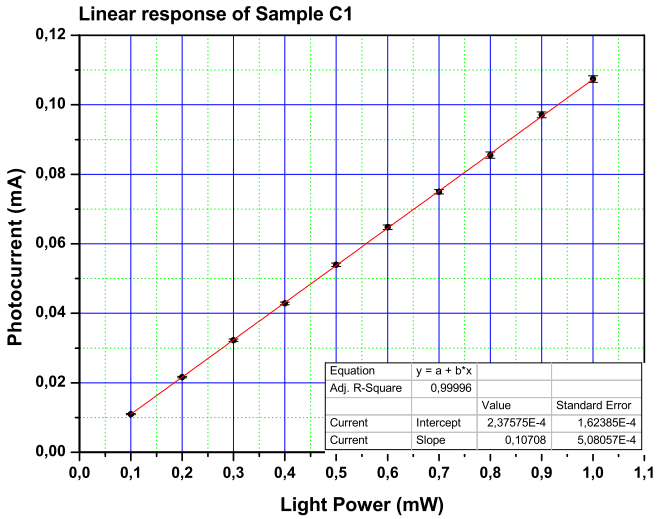

(a)

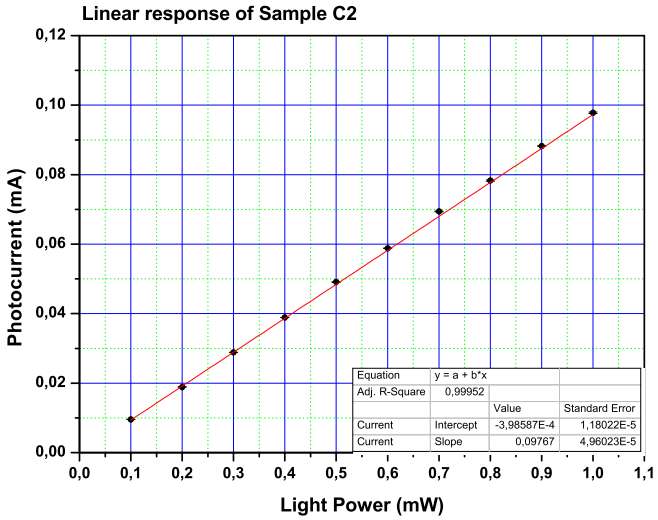

(b)

Figure 4.8: Current versus power light intensity of Samples C1 and C2. The light wavelength is 650nm. The applied voltage is fixed at 25V.

4.3.4 Uniformity

This is a measure of the sensitivity uniformity in the active area. To measure spatial uniformity, a light spot has been scanned in two-dimensions over the photocathode and the variation in the output current has been measured. This data is obtained with a light spot of about 0.5mm diameter (at wavelength of 650nm) scanned over the photocathode surface. The detector surface has been scanned uniformly in the two-dimensional space with a step of 0.5mm.

The photocurrent is generated only if the laser beam illuminates the CNFs layer. Note, in fact, that out of this layer and on the electrodes no signal has been recorded. The situation is illustrated in figure 4.9 where a map of the photocurrent measured by scanning the CNFs surface is reported. It can be seen that the response is relatively uniform in the center of the sensitive surface, but there is a considerable increase of the photocurrent on the top and on the bottom edges of the active area. In particular, the quantum efficiency on the edges exceeds 100%, thus it is obtained a kind of charge multiplication. This phenomenon has also been observed in other samples, it is under study, but a consistent model to explain this physical behavior has not yet been developed.

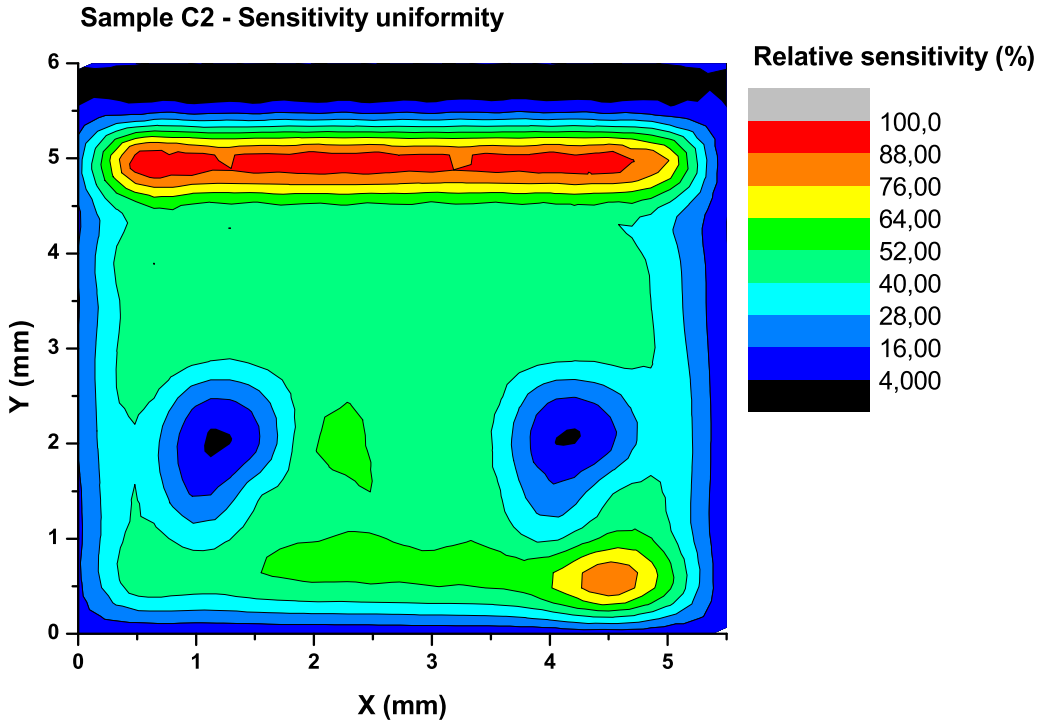

Figure 4.9: *Sensitivity uniformity of Sample C2.*

4.3.5 Quantum Efficiency

The quantum efficiency (QE) of photodevices was estimated as the ratio of the number of electrons collected at saturation I_{sat} to the number of incident photons according to the relation (Section 2.2.2):

$$QE = \frac{I_{sat} hc}{eP\lambda} \tag{4.1}$$

where

- h is the Planck's constant;
- c is the speed of light in vacuum;
- e is the electron charge;
- P is the laser power intensity (measured with a calibrated photodiode);

- λ is the radiation wavelength.

The measured quantum efficiencies of Samples C1 and C2 are shown in Figures 4.10 and 4.11, respectively. Both Samples shown a quantum efficiency with a peak at about 880nm (35% Sample C1 and 30% Sample C2) and at the wavelength of 980nm Samples C1 and C2 have a QE of about 30% and 25%, respectively. This response in the near infrared region makes these Samples interesting for the operation in this wavelength interval.

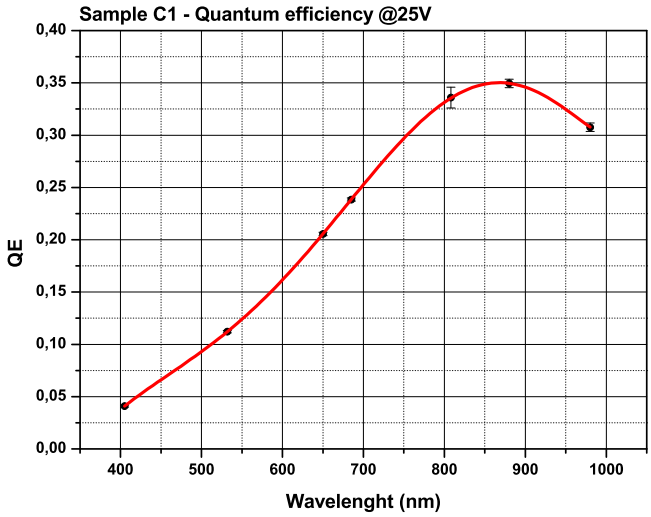

Figure 4.10: *Quantum efficiency of Sample C1.*

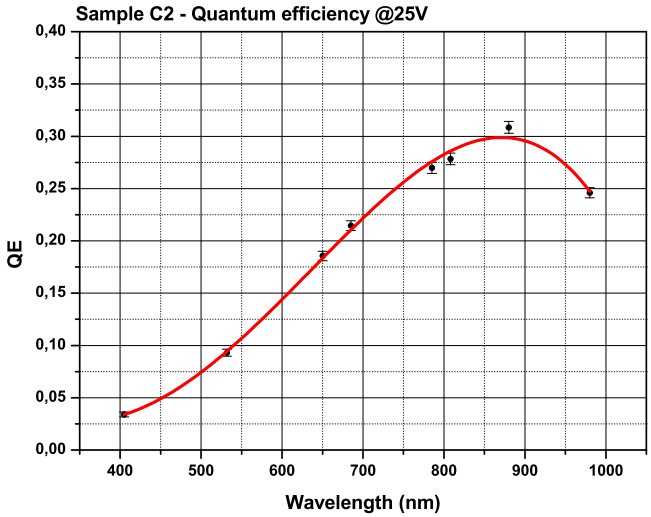

Figure 4.11: *Quantum efficiency of Sample C1.*

4.4 Sample with multiwalled carbon nanotubes (Samples D and E)

In this section we will show the photoelectric characteristics of two samples, called Samples D and E, with nanostructures grown at the CVD temperature of 700°C. Nanostructures obtained are shown in Figure 3.19b. In this case, at a highest CVD temperature, the nanostructures obtained are vertically aligned MWCNTs. The geometric shape of the film is the same as that shown in Figure 4.3, and MWCNTs film covers an area of about 5x5mm^2.

4.4.1 Dark current

Dark currents of Samples D and E are shown in Figures 4.12 and 4.13. It is immediate to realize that the two curves of dark currents are very different from each other, although the substrates and the growth parameters are the same. Furthermore, the dark current of the Sample E is greater than the dark current of the Sample D of several orders of magnitude.

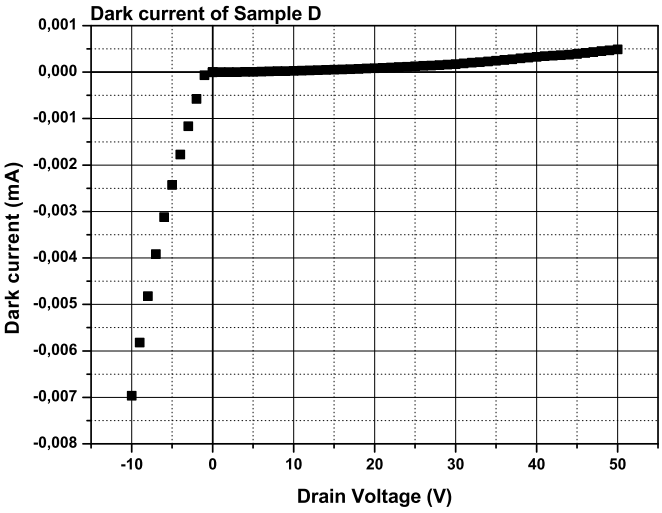

Figure 4.12: *Dark current of Sample D.*

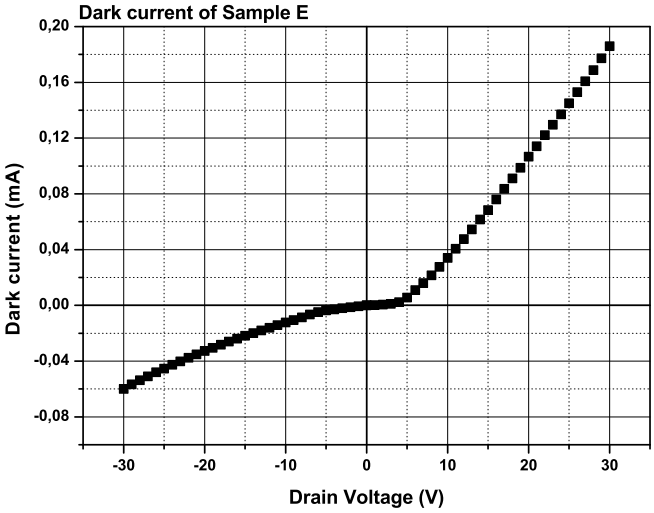

Figure 4.13: *Dark current of Sample E.*

4.4.2 Photocurrent

Photocurrents of Samples D and E are shown in Figures 4.14a and b, respectively, where photoresponses are obtained using a 650nm laser diode light

emitting at various power intensities as a function of drain voltage. It is immediate to note that the very high dark current of Sample E drastically influence the IV characteristic compared to that of Sample D.

The effective photocurrent has been obtained subtracting the dark current from the measured current (figures 4.15a and b). From the last plots we can see that as the applied voltage increases, the current is almost zero until few volts, then it increases linearly reaching a saturation region. The threshold voltage when the current begins to be constant depends on the power light intensity, therefore by the number of charges generated into the device under illumination.

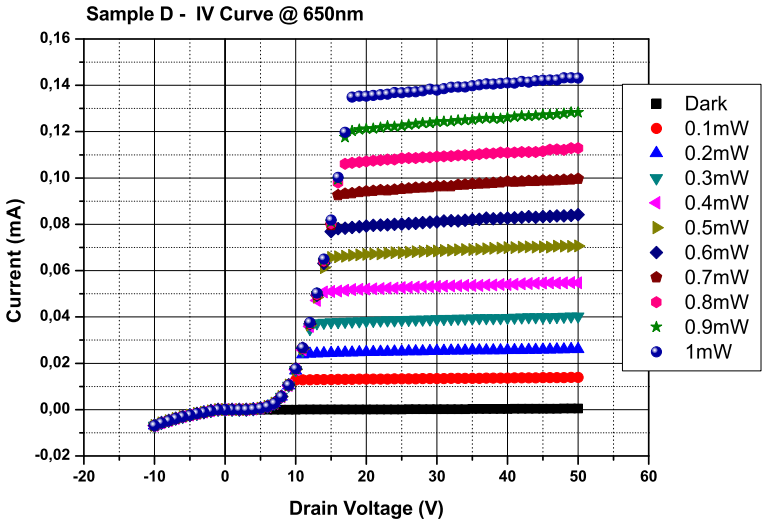

(a)

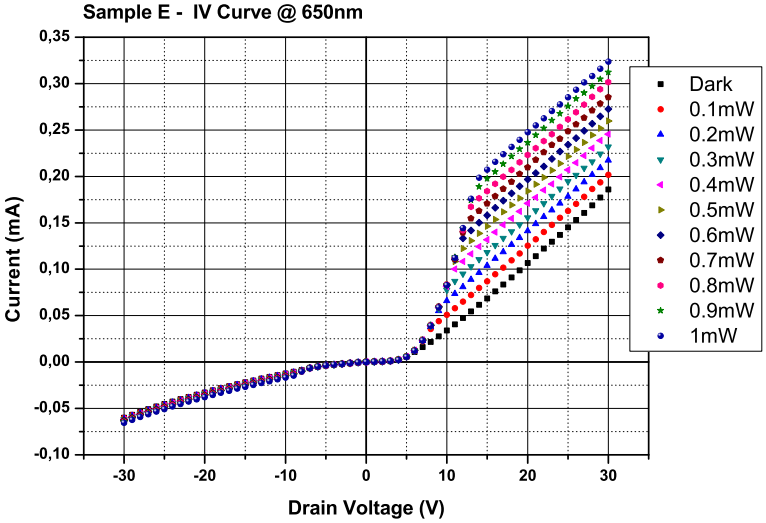

(b)

Figure 4.14: I-V charactristics of Samples D (a) and E (b) at different light intensities.

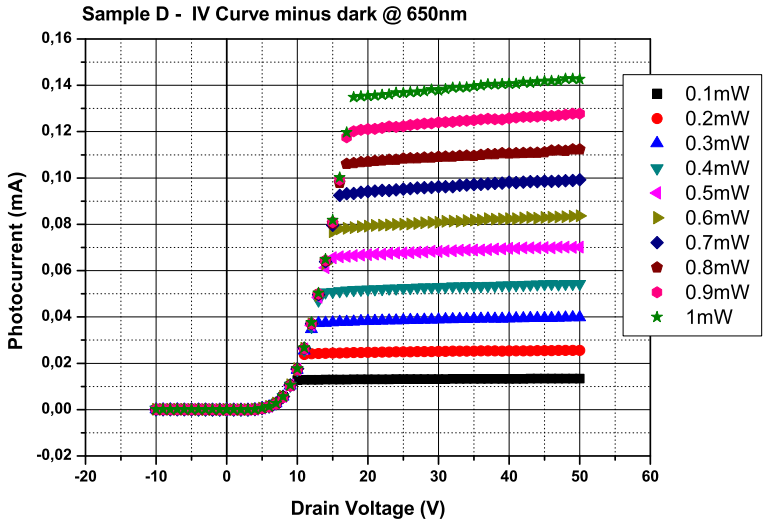

(a)

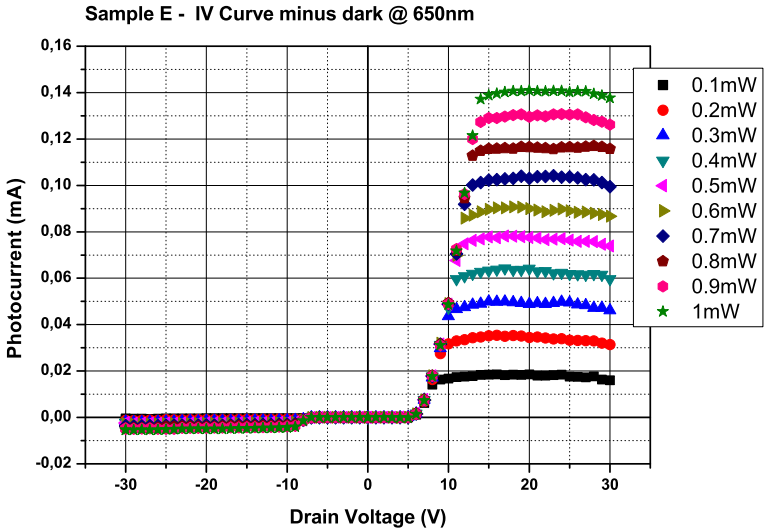

(b)

Figure 4.15: I-V charactristics of Samples D (a) and E (b) with subtracted dark currents.

4.4.3 Linearity

The correlation between the current at saturation versus the light power intensity is reported in figures 4.16a and b, for samples D and E, respectively. For detector D the measurement was performed at the fixed voltage of 30V. For detector E the measurement was performed at the fixed voltage of 25V. As can be seen from fit parameters reported in figures, both detectors exhibit good linearity.

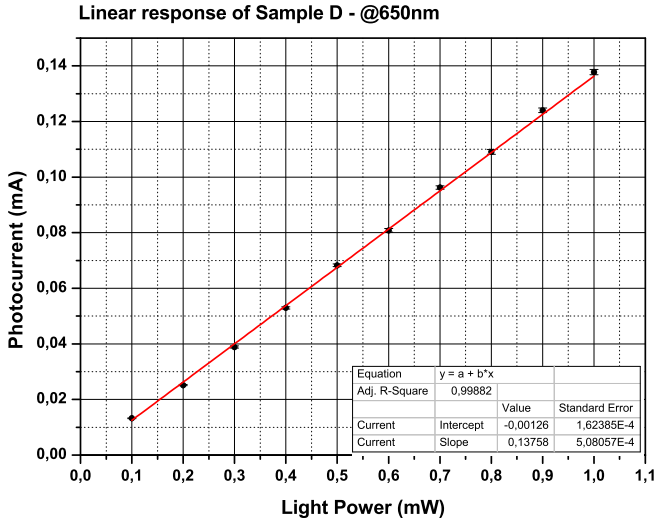

(a)

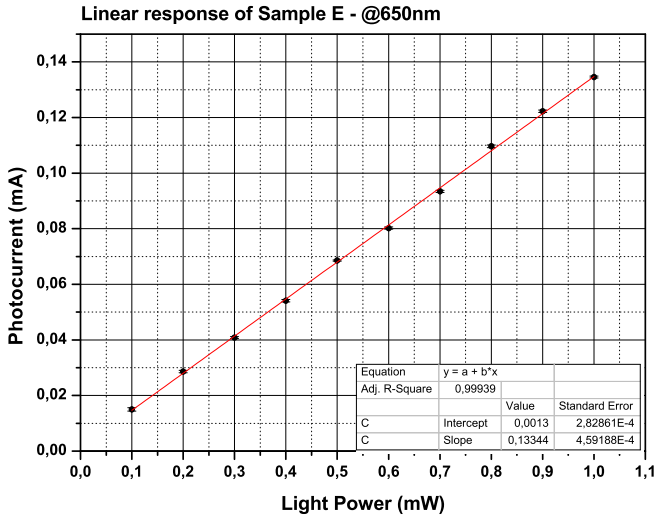

(b)

Figure 4.16: Current versus power light intensity of Samples D and E. The light wavelength is 650nm. The applied voltage is fixed at 30V for Sampe D and 25V for Sample E.

4.4.4 Quantum Efficiency

The measured quantum efficiencies of Samples D and E are shown in Figure 4.17. Taking into account the definition of quantum efficincy (Equation 4.1) and since the two detectors exhibit good linearity, for both detectors the quantum efficiency does not depend on the laser light power intensity.

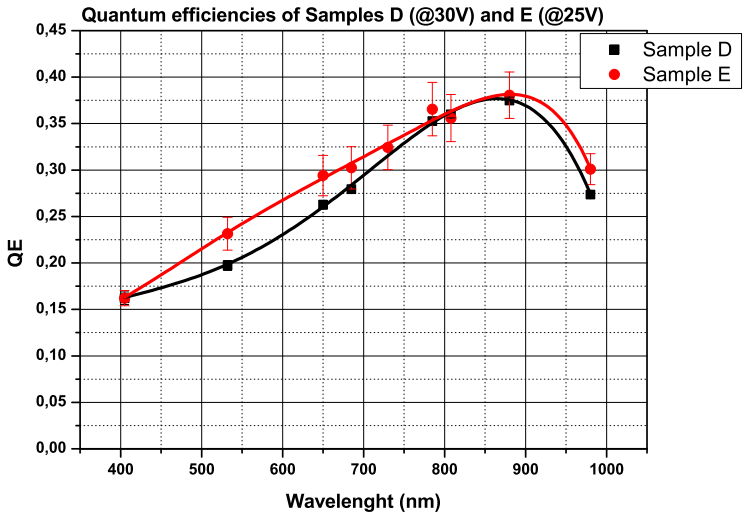

Figure 4.17: *Quantum efficiencies of Samples D and E.*

4.5 Coating with Indium Tin Oxide

In this section properties of a Sample covered with a Indium Tin Oxide (ITO) film on the nanostructures layer will be reported. This study has been carried out with the collaboration of **Prof. A. Valentini** and the experimental and technical contribution of his staff from sezione INFN di Bari.

Photodetectors presented in this work need an electrically conductive coating layer to avoid the nanostructures detachment from the substrate and uniformly transmit the electric field to the entire active surface. Coating material must be transparent to the radiation, and must provide the drain voltage necessary to collect charges generated by incident photons. Indium Tin Oxide is a metal oxide with important physical properties for both basic studies and applications. Because of its low resistivity and high optical transmittance in the range from UV to IR, ITO films are by general consent the most useful for applications in photodetector devices [43]. Many different deposition techniques are described in literature [44] [45] [46]. In the present work ITO films have been deposited by ion beam sputtering (IBS) technique. In figure 4.18 is reported the transmittance spectra of ITO on glass. This measurement shows that film transmission in the 300-800nm wavelength range increases when low energies are used for sputtering (Sputtering source for Samples is fixed at 750V for 0934, 500V for 0936, 350V for 0637 and 0939).

In this section we report on the main characteristics of a sample (Sample IBS0955) with nanostructures grown at the CVD temperature of 500°C. At this CVD temperature we have been obtained carbon nanofibers (CNFs) like those in Figure 3.19a. After the growth process an ITO film has been deposited (In Figure 4.19 is shown a schematic representation of how the ITO is deposited on the Sample) at room temperature on the photocatode made of CNFs, and optical and electrical analyses have been performed.

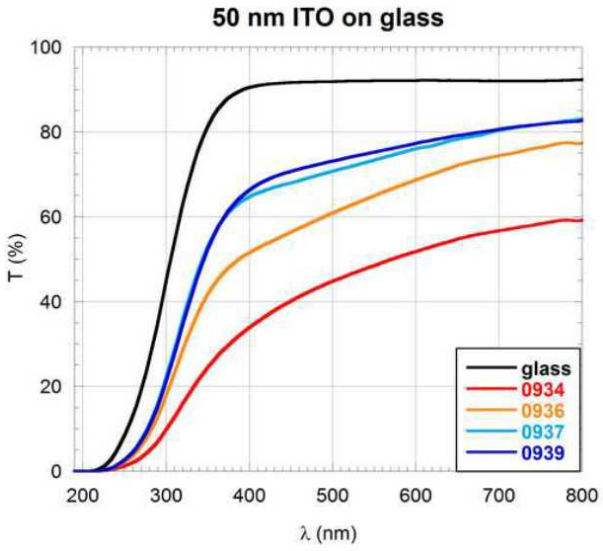

Figure 4.18: *ITO transmittance spectra (Measurements performed by Prof. A. Valentini from sezione INFN di Bari).*

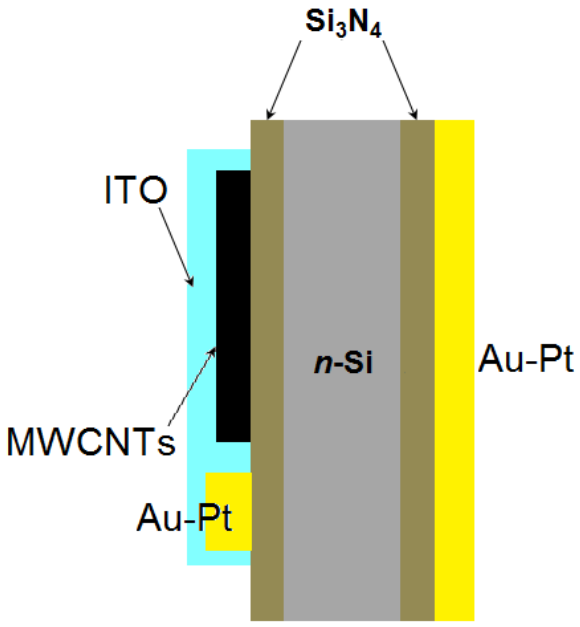

Figure 4.19: *Schematic representation of the deposited ITO film on the Sample (sectional view).*

4.5.1 Dark current

Figure 4.20 reports the dark current of the detector with ITO.

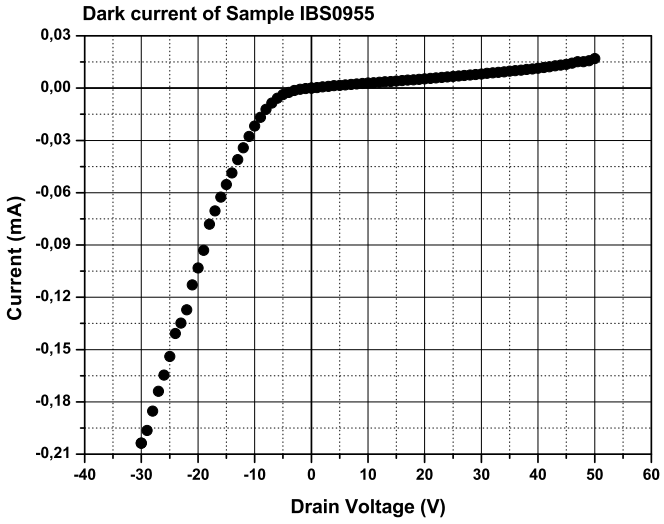

Figure 4.20: *Dark current of samples IBS0955.*

4.5.2 Photocurrent

Figure 4.21 reports the photocurrent produced by Sample IBS0955 under an optical radiation of 650nm.

The effective photocurrent has been obtained subtracting the dark current from the measured current (figure 4.22). Also in this case we can see that as the applied voltage increases, the current is almost zero until few volts, then it increases linearly reaching a saturation region. The threshold voltage when the current begins to be constant depends on the power light intensity, therefore by the number of charges generated into the device under illumination.

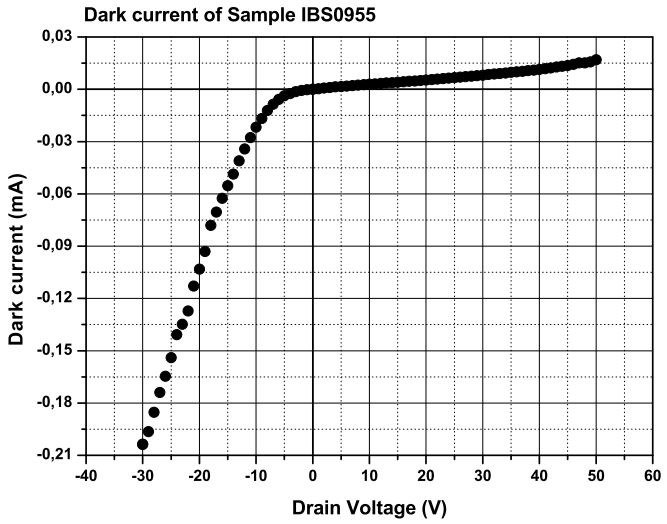

Figure 4.21: *I-V charactristic of Sample IBS0955 at different light intensities*

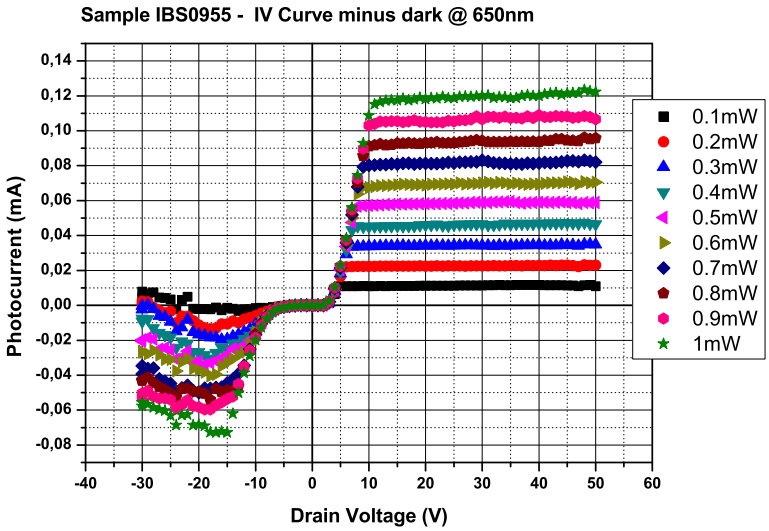

Figure 4.22: *I-V characteristic with subtracted dark current.*

4.5.3 Linearity

The linear relationship between the photocurrent and light level of Sample IBS0955 is shown in figure 4.23. The measure has been performed at the fixed voltage of 25V. As can be seen from fit parameters reported in figure, the detector exhibit good linearity.

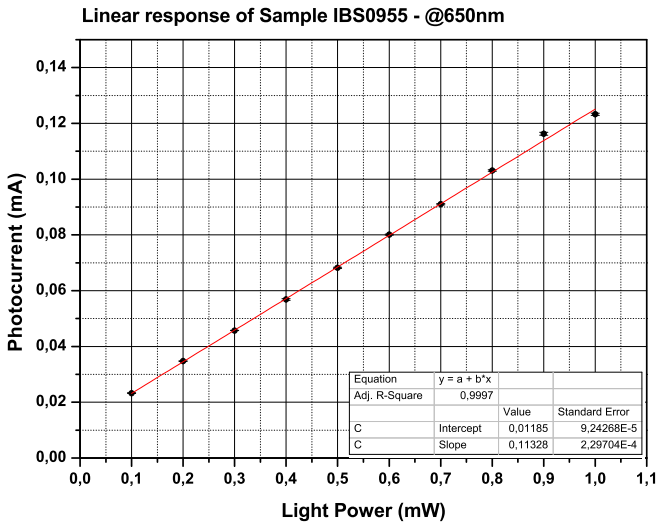

Figure 4.23: *Current versus power light intensity. The light wavelength is 650nm. The applied voltage is fixed at 25V*

4.5.4 Uniformity

This measurement was made by using the monochromatic light emitted by a laser diode with a wavelength of 650nm and a spot of about 0.5mm. The detector surface has been scanned with a step of 0.5mm.

Also in this case the photocurrent is generated only if the laser beam illuminates the CNF layer. Figure 4.24 shows a map of the gerated photocurrent scanning the surface. It can be seen that the response is relatively uniform in the center of the sensitive surface, but there is a considerable increase of the photocurrent on top and bottom edges of the active area.

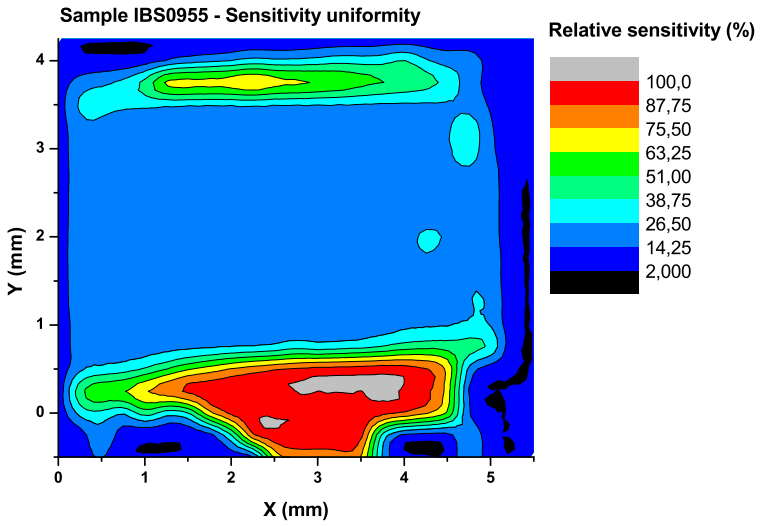

Figure 4.24: *Sensitivity uniformity of Sample IBS0955.*

4.5.5 Quantum Efficiency

The quantum efficiency of the photodetector with ITO film has been also measured and reported in figure 4.25.

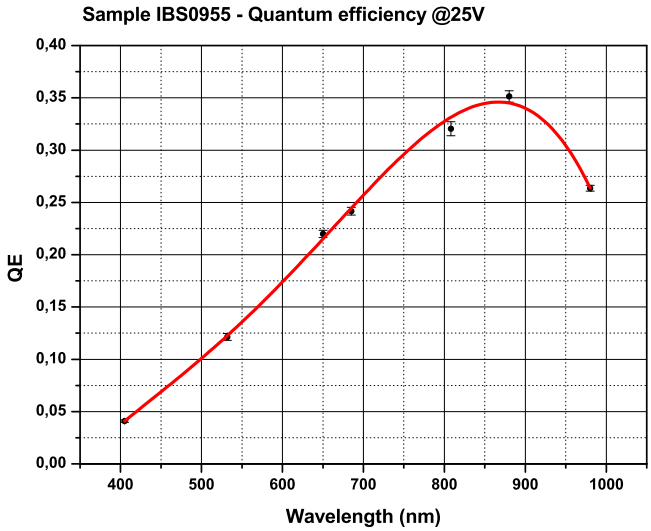

Figure 4.25: *Quantum efficiency of Sample IBS0955.*

4.6 Comparison between devices with MWCNTs, CNFs and with ITO

In the present chapter we have showed the photoresponse of three types of photodetectors based on carbon nanostructures:

- two detectors with carbon nanofibers;
- two detectors with multiwalled carbon nanotubes;
- one detector with carbon nanofibers covered with an ITO film.

Now we compare the characteristics of these five devices.

Dark currents comparison

In Figure 4.26 are shown the dark currents, in logarithmic scale, of the five devices. It is clear that devices composed of carbon nanofibers (Samples C1, C2 and IBS0955) have a comparable dark current. In particular, at the operating voltage (25V) is about 0.5×10^{-3}mA for all devices.

Devices with MWCNTs (Samples D and E) exhibit a dark current significantly different, even though the substrates and the growth parameters of MWCNTs are the same. In particular, we have for the Sample D, at the operating voltage (30V), a dark current of 2×10^{-4}mA, and for Sample E, at the operating voltage (25V), we have a dark current of 0.2mA, which is three orders of magnitude greater.

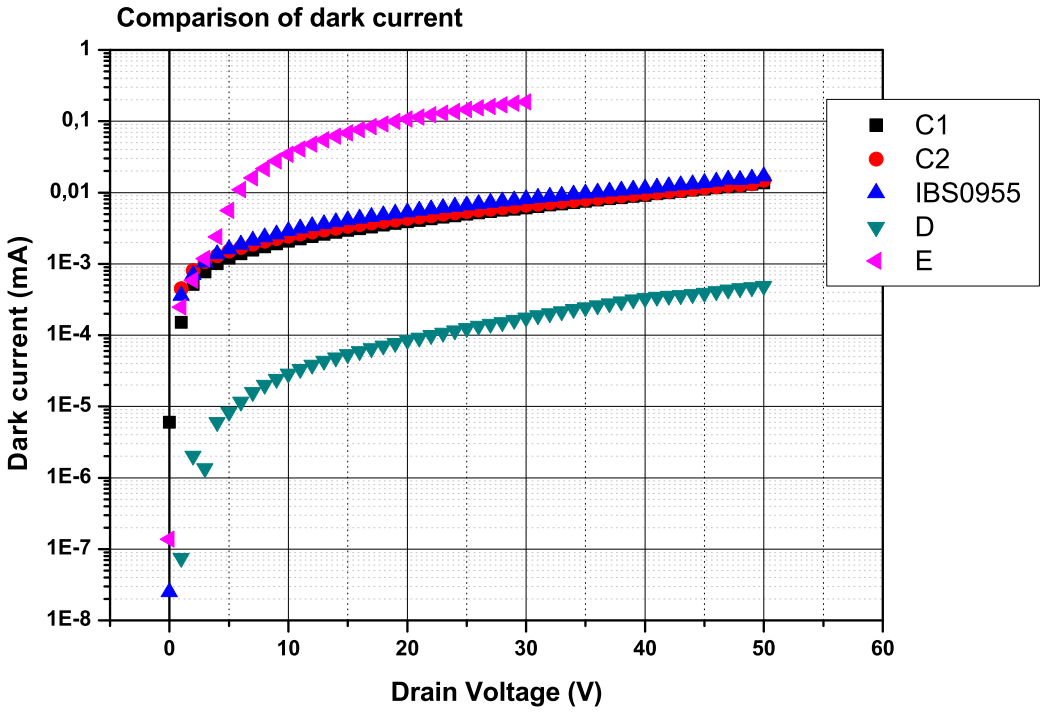

Figure 4.26: *Dark currents comparison.*

Quantum efficiencies comparison

Figure 4.27 shows the quantum efficiencies of the five detectors under test. Photodetectors with MWCNTs exhibit a higher quantum efficiency over the entire spectrum, compared to photodetectors with carbon nanofibers.

Each sample shows a maximum at about 880nm, probably this is due to the contribution in the photoconversion of the silicon substrate.

Sample C2 has the lower quantum efficiency, while Samples C1 and IBS0955 have an efficiency comparable with the measurement errors, and this suggests that the presence of the ITO film does not give any benefit in terms of quantum efficiency. Anyway, with the same nanostructures, it is noteworthy that the sample with ITO seems to have a slightly higher efficiency respect to Sample C1.

The most interesting thing is that the samples with MWCNTs have a greater efficiency toward the violet region of the spectrum. In particular, at 400nm the quantum efficiency of devices with MWCNTs is about four times

higher than that measured for devices with CNFs. Being the substrates identical, this behaviour could be due to the presence of MWCNTs which could contribute to the photon conversion in the violet region.

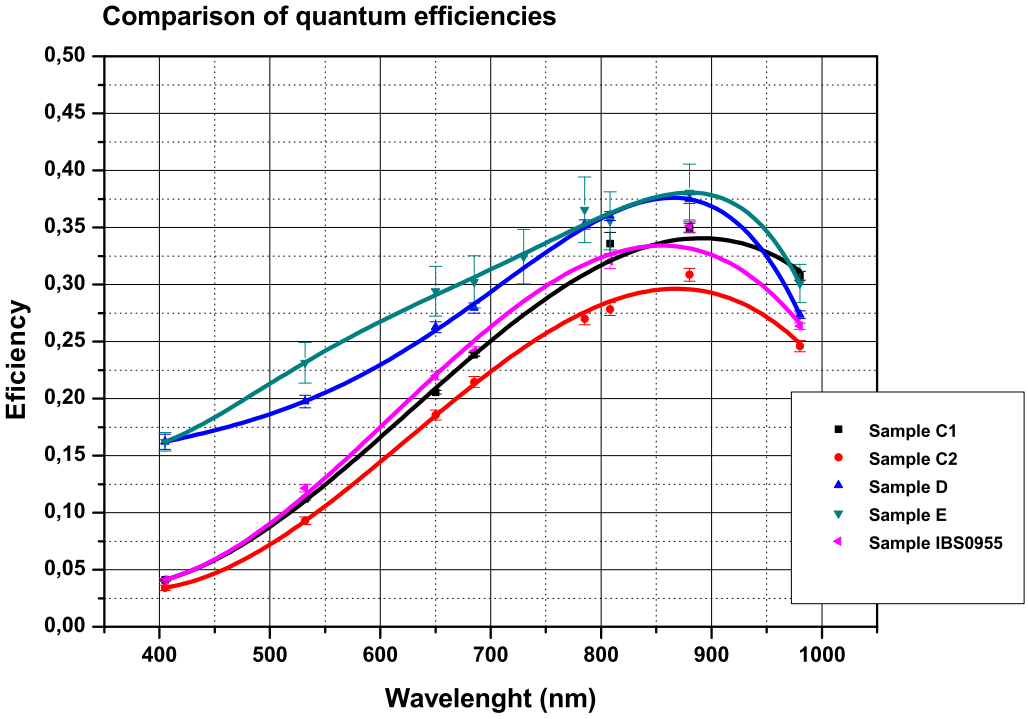

Figure 4.27: *Quantum efficiencies comparison.*

Responsivities comparison

The structures of responsivities were investigated in order to highlight differences between the nanostructures and the presence of ITO film.

Figure 4.28 reports the comparison between photoresponsivity to a 880nm optical radiation (880nm is the maximum of quantum efficiency for all devices). We can note that as the applied voltage increases, the responsivities are very low until one reaches a threshold of few volts (conduction threshold), then they increase until saturation is reached (plateau threshold). The conduction threshold and the plateau threshold were evaluated. To estimate these thresholds does not exist a particularly rigorous method, but several methods may be used. In particular, we have evaluated the maximum and the minimum of the second derivative of responsivity, which may be associated with the conduction threshold and the plateau threshold, respectively. This identification method has been chosen observing the particular shape of the curves. Responsivity curves have, in first approximation, variations in slope (represented by the first derivative) only in the neighborhoods of the conduction (positive variation) and the plateau threshold (negative variation). For this reason, these variations of the first derivative, linear in first approximation, will be identified as "peaks" of the second derivative, positive in the case of the conduction threshold and negative in the case of the plateau threshold.

The method employed is shown in Figures 4.29, 4.30, 4.31, 4.32, 4.33. So, voltage thresholds of devices have been evaluated and reported in Table 4.1. As we can see from Table, the conduction thresholds are lower for samples with CNFs, and have highest values for samples with MWCNTs. It should be noted that the sample with ITO has the conduction and plateau thresholds lower, this can be explained by the fact that the presence of ITO facilitates current drain, but on the other hand the presence of ITO does not increase the responsivity because the region of the plateau is equal to that of the Sample C1.

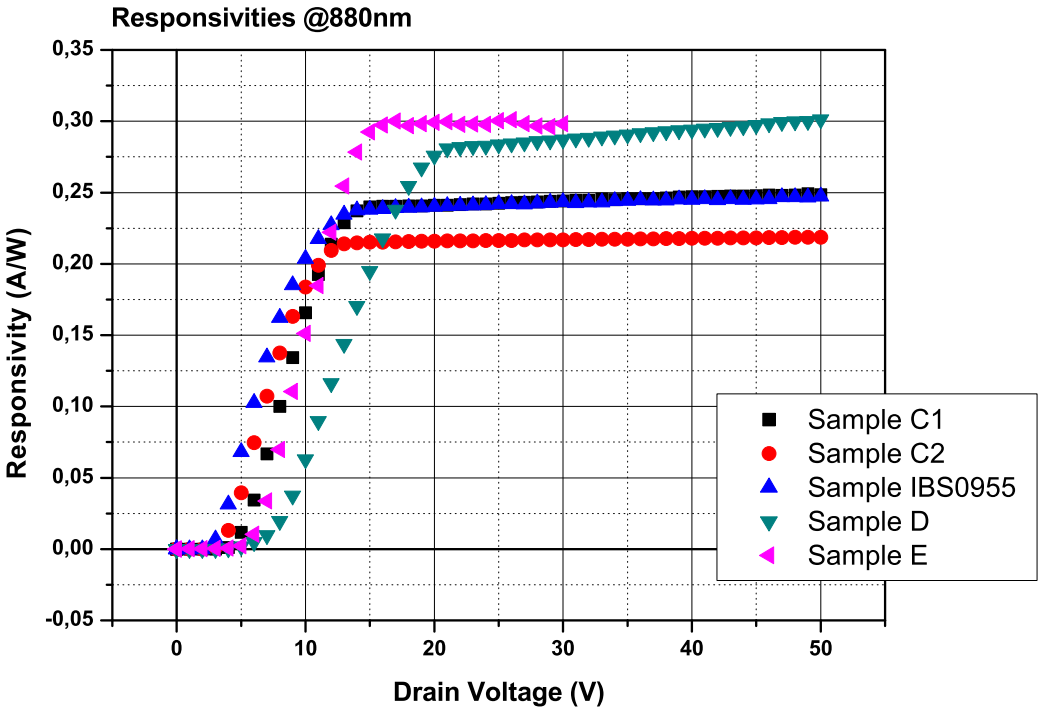

Figure 4.28: *Responsivities comparison.*

Sample	Conduction threshold (V)	Plateau threshold (V)
C1	5.06	12.36
C2	3.92	10.65
IBS0955	3.15	7.90
D	8.27	18.45
E	6.35	14.18

Table 4.1: Conduction and plateau thresholds.

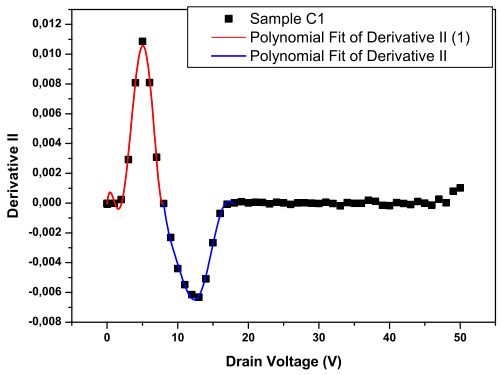

Figure 4.29: *Sample C1. Second derivative of Responsivity. Maximum: 5.06V; minimum: 12.36V.*

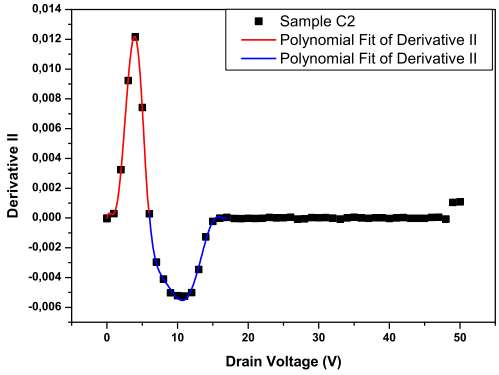

Figure 4.30: *Sample C2. Second derivative of Responsivity. Maximum: 3.92V; minimum: 10.65V.*

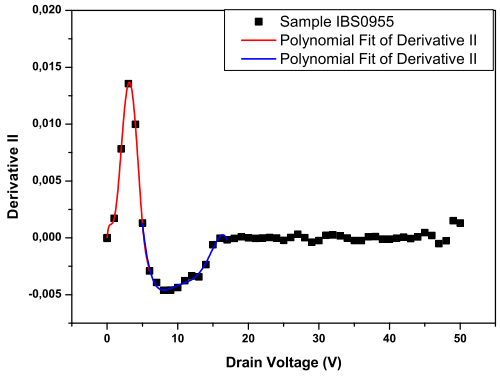

Figure 4.31: *Sample IBS0955. Second derivative of Responsivity. Maximum: 3.15V; minimum: 7.90V.*

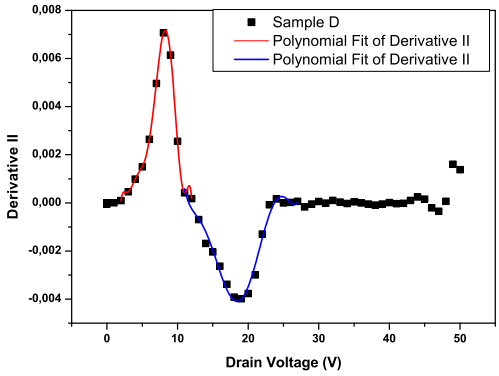

Figure 4.32: *Sample D. Second derivative of Responsivity. Maximum: 8.27V; minimum: 18.45V.*

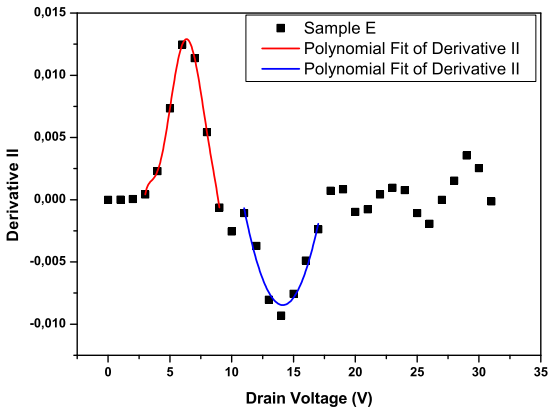

Figure 4.33: *Sample E. Second derivative of Responsivity. Maximum: 6.35V; minimum: 14.18V.*

4.7 Comparison with standard solid-state photodetectors

Detectors based on carbon nanostructures have been shown to be sensitive to a continuous flow of light radiation, with a wavelength ranging from near infrared to near ultraviolet (from 400nm to 980nm). We investigated the light power response of detectors ranging from 0.1mW to 1mW. These detectors become less sensitive to levels of power light lower than 0.1mW. In particular, they are absolutely not sensitive to single photons, as photomultiplier tubes or silicon photomultiplier. In fact, they do not show mechanisms of charge multiplication, and exhibit very high dark current compared with silicon photomultiplier. For this reason, these photodetectors can be compared, for example, with photodiodes or phototubes. So, in this section we compare devices with carbon nanostructures with solid state devices which measure relatively high power light levels in continuous mode (usually ranging from 10^{-12} to 10^{-2}W, in the spectum from near infrared to ultravilet region): silicon photodiodes.

Spectral response comparition

As already mentioned in section 2.2.2 and 2.4, usually, the spectral response of photodiodes is expressed in spectral responsivity.

Figure 5.34 shows measured spectral dependence of various kinds of com-

mercial photodiodes expressed in spectral responsivity. For ordinary photodiodes, the cut-off wavelength on the short wavelength side is 320nm, whereas it is 190nm for UV-enhanced Si photodiodes. In the case of silicon at room temperature, the band gap energy is 1.12eV, so the cut-off wavelength in the IR region is 1100nm. The BQ type uses a quartz window, the BK type a borosilicate glass window, and the BR type a resin-coated window. The S9219 is a Si photodiode with a visual-sensitive compensation filter.

Figure 4.35 shows spectral responsivities of Samples C1, C2, IBS0955, D and E, where the black line is the quantum efficiency at 100%. The responsivity of photodetectors based on carbon nanostructures has been calculated as explained in Section 2.2.2. Comparing the measurements shown in Figure 4.35 with spectral responses of commercial photodiodes, it is evident that the conversion efficiency of photodetectors based on carbon nanostructures is very low. In particular, the Hamamatsu S3590-19 (which is UV-sensitive) in the near ultraviolet region (about 400nm) shows a quantum efficiency very close to 100%, while at 400nm the higher efficiecy of detectors based on carbon nanostructures is 16%.

It is clear that these devices are not competitive with existing devices in terms of spectral response, in particular near the ultraviolet region.

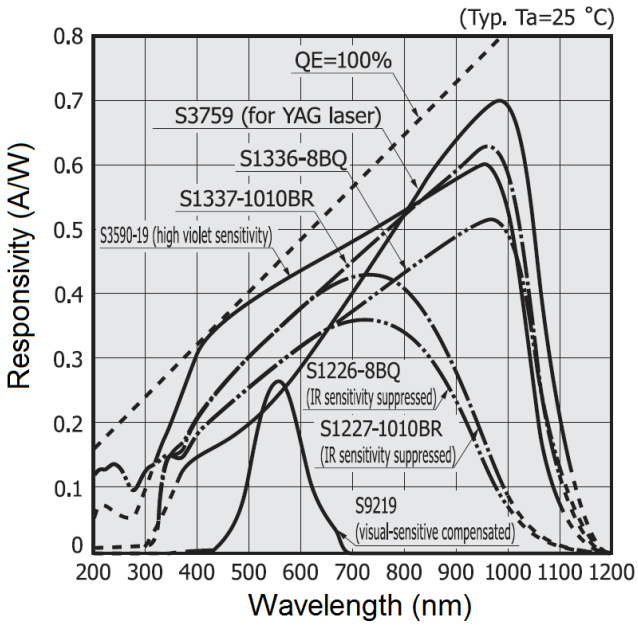

Figure 4.34: *Typical spectral response of commercial silicon photodiodes. The dashed black line is the quantum efficiency at 100%. (From Hamammatsu catalog).*

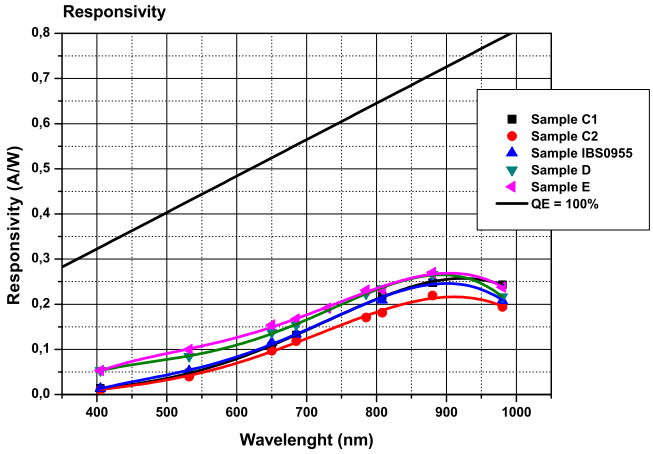

Figure 4.35: *Spectral response of samples with carbon nanostructures. The black solid line is the quantum efficiency at 100%.*

4.8 Interpretation and model

In this section we will introduce a first model for devices based on carbon nanostructures, in particular, the simulations will be compared with Samples C2 and D, presented in previous sections of this chapter. The basic principle of operation the of developed photodetectors can be the following. Carbon nanostructures can form local Schottky junctions on the same nanotube due to the presence of twisting [54] or bending, between adjacent tubes forming a bundle, [55] and between tubes crossing each other [56]. Moreover, the presence of van Hove singularities in the electronic density of states of CNTs provides optical absorption responses extending from the infrared to the ultraviolet energy range. Also networks of entangled CNTs, where nanotubes touch and cross each other forming many junctions, exhibited sizeable photocurrent [56] [57] [58] [59]. Photoresponces observed in the present work are a mixture of these effects. We have also seen that carbon nanostructures covering doped silicon substrates create an heterojunction [40], in this case, both carbon nanostructures film and the silicon underneath participate in the photocurrent activation process: electron-hole pairs of longer wavelength can be generated both in carbon nanostructures layer and in the depleation layer of the heterojunction and separated.

Since silicon nitride is a good insulator, in principle there should be no current flowing between the electrodes when a voltage is applied. But the high temperature carbon nanostructures growth procedure causes defects in the bulk of the dielectric film, and then under bias application some current will conduct through the insulator defects, usually a tunneling current. When these defects reach a critical density level, catastrophic breakdown occurs (figure 4.36). In fact, when we applied the first voltage to the device we did not observe any charge flowing, but after a bias application of several tens of volts the device starts to operate as shown in previous paragraph. From a microscopic point of view, a percolation theory is employed to describe this phenomena.

In Addition on the back side of the substrate we have a MIS junction.

4.8.1 The energy band diagram

In order to understand the energy-band structure of the devices, we start from the parameters of the materials employed. The work function of the Au-Pt is $5.1 - 5.47$ eV. For silicon nitride we have an energy gap of 5.3 eV and an electron affinity of 2.1 eV. Silicon n-type (the doping concentration is 4×10^{15} cm^{-3}) has the following parameters: a work function of 4.28 eV and an electron affinity of 4.05 eV.

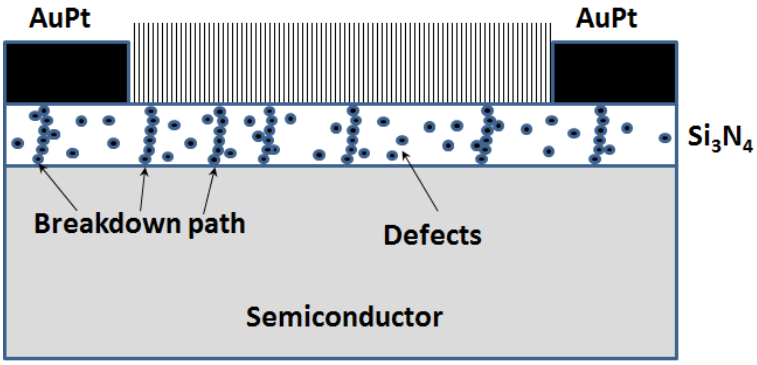

Figure 4.36: *When defects are dense enough to form a continuous chain shorting the electrode to the semiconductor, a conduction path is created and catastrophic breakdown occurs.*

A number of theoretical and experimental studies have been done on work functions of different CNTs. For semiconductor SWNTs the band gap E_G is function of the diameter, and is approximated by the formula [22]

$$E_G = \frac{2 \times \gamma \times a_{C-C}}{d_t} \tag{4.2}$$

where

- d_t is the diameter of the nanotubes,
- γ is 2.77eV,
- $a_{C-C} = 0.1421nm$ is the nearest neighbor carbon-carbon distance.

The MWCNTs consists of a concentric set of CNTs of both metallic and semiconducting types, and so they present a wider range of energy gap, ranging from 0 to 3eV, sensitive to a wide range of radiation wavelenght. Using the transmission electron microscope technique, Gao et al. [23] measured the work function of individual MWCNTs and reported the value of $4.6 - 4.8$eV. Moreover, using the photoelectron emission method, Shiraishi and Ata [24] measured the work functions of MWCNTs and reported value of 4.95eV. Figure 4.2b shows a schematic representation of our devices and figure 4.37 its energy band characteristics. The devices can be operated in two modes. First, the incident photon produces electron-hole pairs in the semiconductor, this pairs are separated by the electric field, leading to current flow in the external circuit as carriers drift across the depletion layer. Second, for higher photon energy the electrons photoexcited in the MWNTs can be collected.

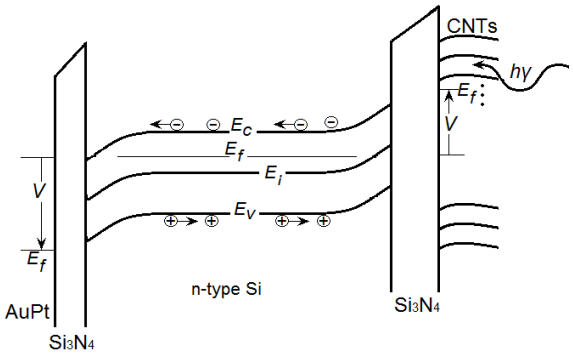

Figure 4.37: *Energy-band diagram of the photodetector biased in normal operating conditions.*

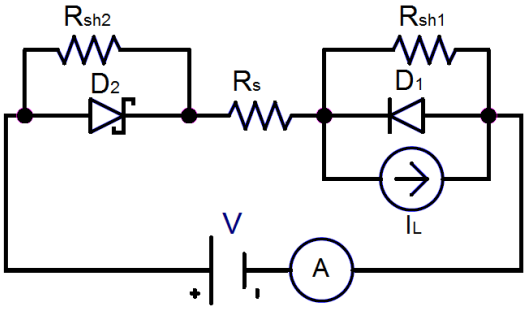

Figure 4.38: *Equivalent circuit of samples C2 and D.*

4.8.2 Model and simulation

In order to verify this model, simulations have been performed using PSpice, under the hypothesis that measured forward and reverse currents are due respectively to the hetero and to the MIS junctions. We start from the equivalent circuit schematically drawn in Figure 4.38, where two diodes have both cathodes facing each other. In particular,

- D1 is the carbon nanostructures-silicon heterojunction,
- R_{sh1} is the parasitic parallel resistance (shunt) of D1,
- I_L is the current generated by the incident light (proportional to the amount of light),

- D2 is the MIS junction,
- R_{sh2} is the shunt resistance of D2,
- R_s is the parasitic series resistance common to D1 and D2.

We used the Analog Behavioral Modeling (ABM) of PSpice to make flexible descriptions of electronic components in terms of a mathematical relationship. In particular, this approach has been adopted for the two junctions D1 and D2.

As schematically shown in Figure 4.39, we have three operation modes in

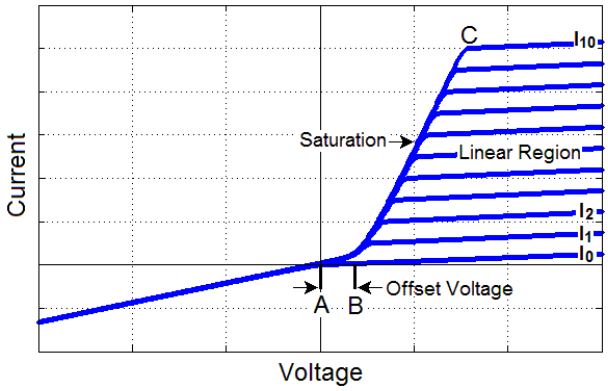

Figure 4.39: *General example of operation modes in terms of applied voltage.*

terms of applied voltage, junction biasing and light intensities. For example at the light intensity I_{10} we have the following cases:

- A) For B<V<C, the junctions are forward-biased ("saturation mode"), and the current is a linear function of the applied voltage;
- B) For V>C, the junction D2 is forward-biased and the junction D1 is reverse biased, the current is approximately constant and we are in the "linear region";
- C) For V<A the junction D1 is forward-biased and the junction D2 is reverse biased.

Figure 4.40 shown the effects of series resistance and parallel resistances (shunt) on the IV characteristic of the photodetector. In particular:

- A) The shunt resistance R_{sh2} influences the slope of the segment lying between A and B, this slope is 0 in the ideal case ($R_{sh2} = \infty$);

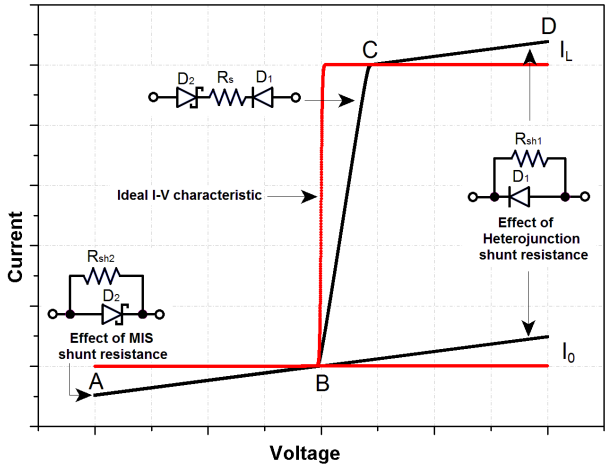

Figure 4.40: *Ideal IV characteristic (black) and influence of parassitic resistances reflected in the IV characteristic (red).*

- B) The shunt resistance R_{sh1} influences the slope of the segment lying between C and D, this slope is 0 in the ideal case ($R_{sh1} = \infty$);
- C) The series resistance R_s influences the slope of the segment lying between B and C, this slope is ∞ in the ideal case ($R_{sh2} = \infty$).

As proposed by A. Tinti et al. in [40], for devices with structures grown at a CVD temperature of 500 °C, we adopted for the heterojunction D1 an expression of the form

$$I_1 = I_{01} e^{\alpha_1 V_1} \tag{4.3}$$

For sample C2 we have the values:

- $I_{01} = 1.505 \times 10^{-6}$ A;
- $\alpha_1 = 6V^{-1}$.

We adopted an expression of the same form for the junction D2 but with the following parameters:

- $I_{02} = 1.192 \times 10^{-8}$ A,
- $\alpha_2 = 0.72$ V^{-1}.

The values of the resistances are:

- $R_{sh1} = 4$ MΩ,

- $R_{sh2} = 1.95$ MΩ,
- $R_{sh2} = 30$ kΩ.

We used the same expression (4.4) for the devices with CNTs grown at the CVD temperature of 700°C. In particular for sample D we have for D1:

- $I_{01} = 1 \times 10^{-9}$A,
- $\alpha_1 = 15V^{-1}$.

And for D2 the following parameters:

- $I_{02} = 1.192 \times 10^{-8}$A,
- $\alpha_2 = 0.72V^{-1}$.

The values of the resistances are:

- $R_{sh1} = 168M\Omega$,
- $R_{sh2} = 10M\Omega$
- $R_{sh2} = 41k\Omega$.

For devices with CNTs grown at 700°C, the previous model is valid only for small light power ($<300\mu$W). For light intensities $>300\mu$W, the current isn't constant in the plateau region but increases as V increases, with the following law

$$I_{700} = I(a + bV) \tag{4.4}$$

where $a = 1.0017$ and $b = 2.86 \times 10^{-2}V^{-1}$.

Experimental and simulation data for sample C2 and D are reported in Figure 4.41 and 4.42, respectively. It is easy to note the very good reproduction of the measured curves, thus confirming the validity of the interpretation of the device operational model we suggest.

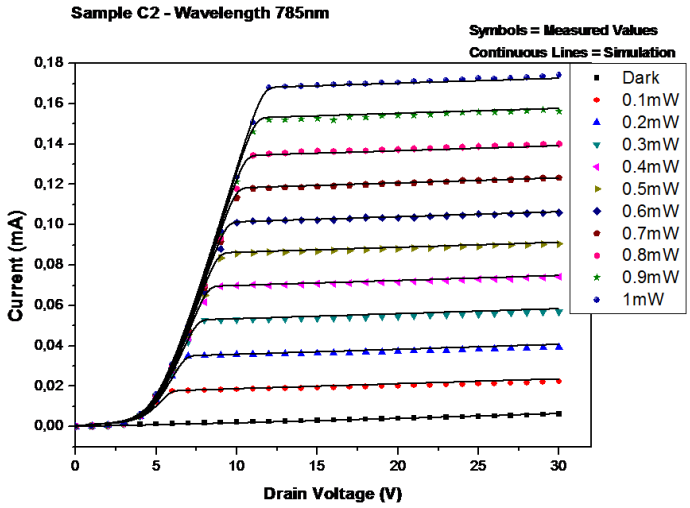

Figure 4.41: *Comparison between measured and simulated data for sample C2.*

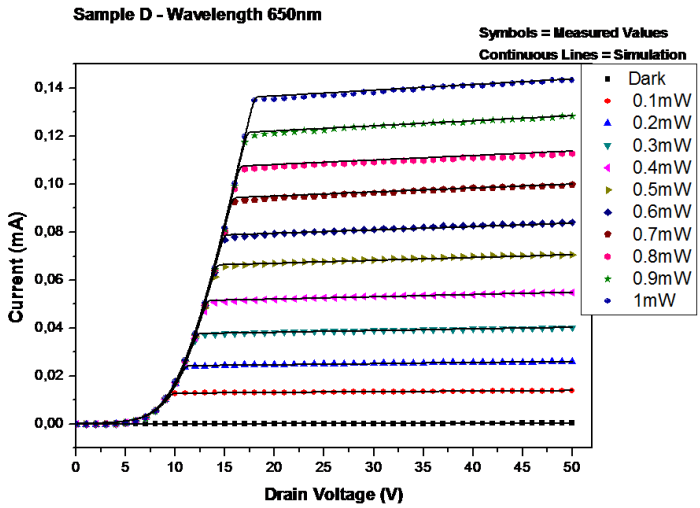

Figure 4.42: *Comparison between measured and simulated data for sample D.*

Chapter 5

The MWCNT-Si photodetectors II (IRST 5 production)

After the production and the characterization of photodetectors shown in Chapter 4, a set of substrates has been manufactured with different structures in order to obtaining an effect of charge multiplication inside the Silicon substrate. Samples shown in this chapter consist of substrates produced by the Fondazione Bruno Kessler (FBK), while MWCNTs have been grown by Dr. M. Passacantando from University of L'Aquila.

This chapter shows the measurements performed on this new type of device, similarly to that reported in the previous chapter, with in more sizes the measurements of capacitance versus voltage, but without the interpretation and simulations developed for previous samples, since at the moment is still going on their study.

5.1 The FBK-Trento substrates

Geometric shape and materials of substrates are shown in Figure 5.1. Substrates have a body of silicon doped both n and p. p-type Silicon has a concentration ranging from 0.4 to 0.7 Ωcm; n-type Silicon has a concentration ranging from 12 to 18 Ωcm. On the top side we have: a layer of 60nm of stoichiometric Silicon Nitride (Si_3N_4); on the layer of Si_3N_4 two circles of 1mm diameter made of titanium-platinum (Ti-Pt) for ohmic contacts, with a thickness of 120nm, are implanted; under the Si_3N_4 different contact structures are implanted (reported in Table 5.1). On the bottom side different contact structures are implanted (reported in Table 5.1).

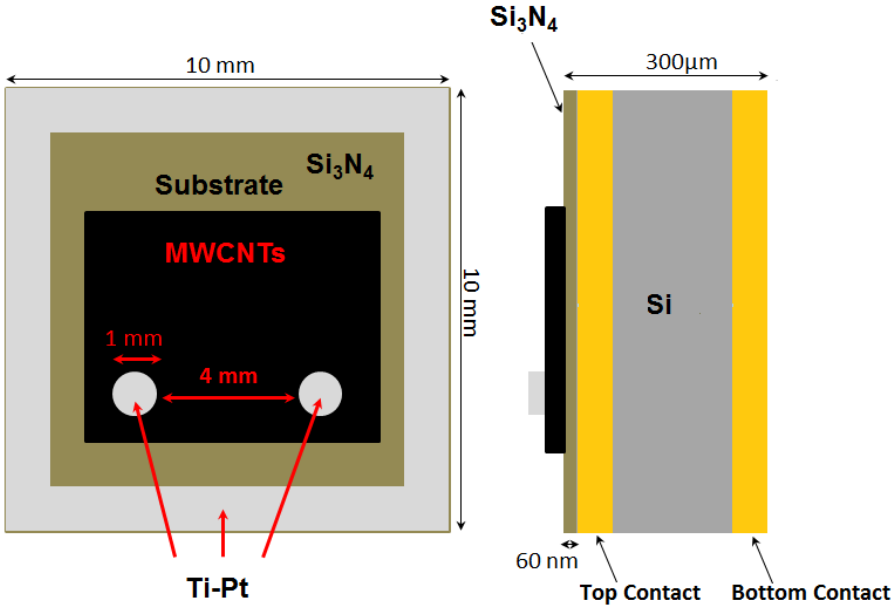

Figure 5.1: *General structure of substrates. On the left top view, and on the right cross-sectional view (not in scale).*

In Table 5.1 are shown the different types of produced substrates. On the lines of the table are reported the characteristcs of the substrates. On the first column there are the names of substrates; on the second, the carbon structure grown on substrate; on the third, the contact present between the carbon nanostructures and the substrate (n+ = high n-doped silicon, p+ = high p-doped silicon, NP = not present); on the fourth, the type of substrate (n-doped or p-doped); on the fifth, the electric contact of the bottom side (n+ = high n-doped silicon, p+ = high p-doped silicon, MIS = metal insulator

contact, MS = metal contact).

Substrate name	C-Structure	Top contact	Substrate	Bottom contact
IRST5-1 IRST5-2	MWCNT	NP	p-type	n+
IRST5-5 IRST5-6	MWCNT	NP	p-type	p+
IRST5-11 IRST5-12	MWCNT	n+	p-type	p+
IRST5-15 IRST5-16	MWCNT	NP	n-type	n+
IRST5-21 IRST5-22	MWCNT	NP	n-type	p+
IRST5-27 IRST5-28	MWCNT	NP	n-type	MIS
IRST5-33 IRST5-34	MWCNT	NP	n-type	MS
IRST5-37 IRST5-38	MWCNT	p+	n-type	n+

Table 5.1: Substrates structures.

5.1.1 Substrates photoresponse

Electrical measurements have been done applying an electric field with the top-side electrodes at ground and varying the voltage on the back of the device, as illustrated in the sketch of figure 4.4. For each substrates were performed measurements of dark currents (figures 5.2a, 5.3a, 5.4a, 5.5a, 5.6, 5.7a, 5.8a, 5.9a), and photoresponses with relative dark currents subtracted (figures 5.2b, 5.3b, 5.4b, 5.5b, 5.6b, 5.7b, 5.8b, 5.9b). All substrates show the presence of junctions. These junctions are present for various reasons, mainly to obtain an internal amplification.

In the next lines we will comment on volt-amperometric characterization of substrates.

Substrate IRST5-2 has a p-doped silicon body, and a highly n-doped implant of silicon on the back. The presence of the pn+ junction is evident in the measure of dark current of figure 5.2a. This junction enables the substrate to be sensitive to light, as we can see in the measurements reported in figure 5.2b.

Substrate IRST5-6 has a p-doped silicon body, and a highly p-doped implant of silicon on the back. This substrate is not light sensitive (Figure 5.3b).

Substrate IRST5-12 has a p-doped silicon body, a highly n-doped implant of silicon on the top, and a highly p-doped implant of silicon on the bottom. The junction n+p on the top side is highlighted by the measurement of the dark current (Figure 5.4a). The n+p junction on the top permits the substrate to be sensitive to light (measurements reported in Figure 5.4b).

Substrate IRST5-16 has a n-doped silicon body and a highly n-doped implant of silicon on the bottom side. Dark current measurement (Figure 5.5a) shows the presence of a junction, this junction is created under the top electrodes: it arise from the presence of the metal of the upper electrodes, the silicon nitride and the n-doped silicon of the body of the substrate (a MIS junction). This junction is not sensitive to light (Figure 5.5b) because it is formed under the upper electrodes, which are not transparent to light.

Substrate IRST5-22 has a n-doped silicon body and a highly p-doped implant of silicon on the bottom side. This substrate has a junction np+ on the back, which is evidenced by the dark current (Figure 5.6a) and the photoresponse (Figure 5.6b), but it is also evident a photosensitive junction on the top side. Probably this junction is created between the top electrodes and the silicon and is very wide, and in this case the light is able to reach it, in contrast to the previous substrate.

Substrate IRST5-22 has a n-doped silicon body and a MIS junction on the bottom side. The MIS junction is evidenced by measurements reported in Figures 5.7a, 5.7b.

Substrate IRST5-34 has a n-doped silicon body and a MS contact on the bottom side. Dark current measurement (Figure 5.8a) shows the presence of a junction, this junction is created under the top electrodes: it arise from the presence of the metal of the upper electrodes, the silicon nitride and the n-doped silicon of the body of the substrate (a MIS junction), like in the case of the substrate IRST5-16. This junction is not sensitive to light (Figure 5.8b) because it is formed under the upper electrodes, which, in this case, are not transparent to light.

Substrate IRST5-38 has a n-doped silicon body, a highly p-doped implant of silicon on the top, and a highly n-doped implant of silicon on the bottom. The junction p+n on the top side is highlighted by the measurement of the dark current (Figure 5.9a). The p+n junction on the top permits the substrate to be sensitive to light (measurements reported in Figure 5.9b).

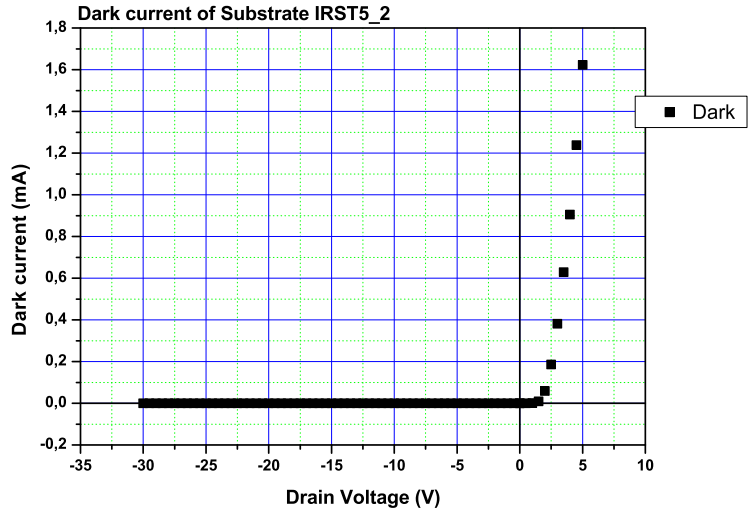

(a)

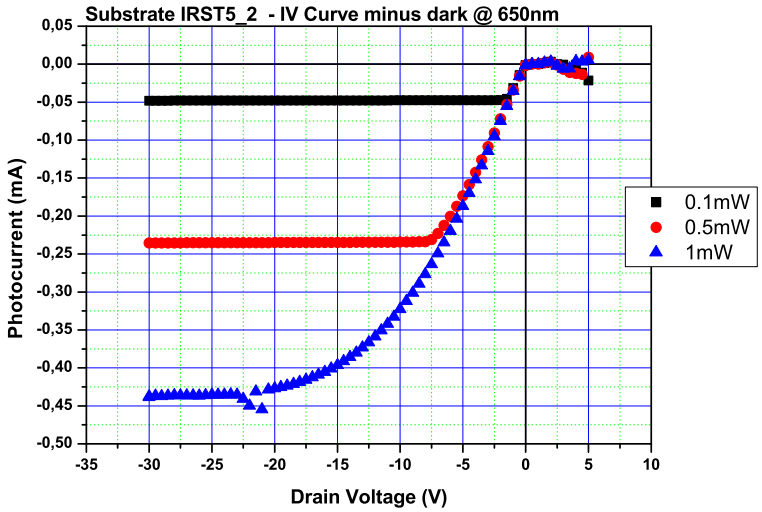

(b)

Figure 5.2: Dark current (a) and photocurrent (b) (the light wavelength is 650nm) of substrate IRST5-2.

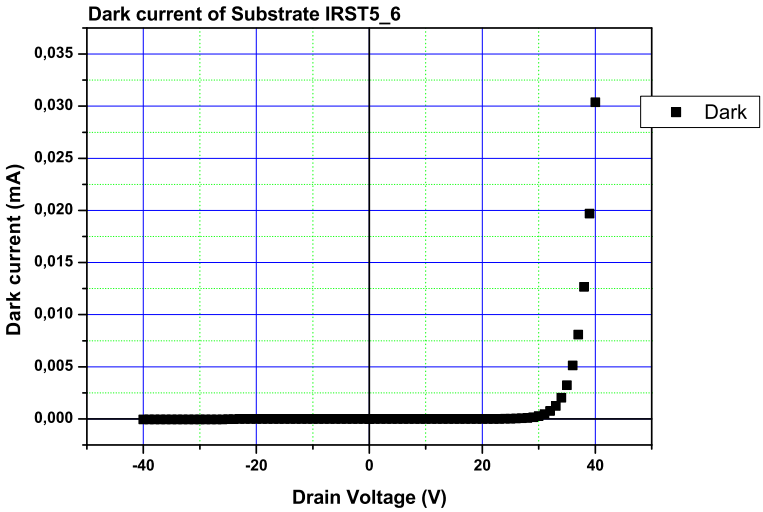

(a)

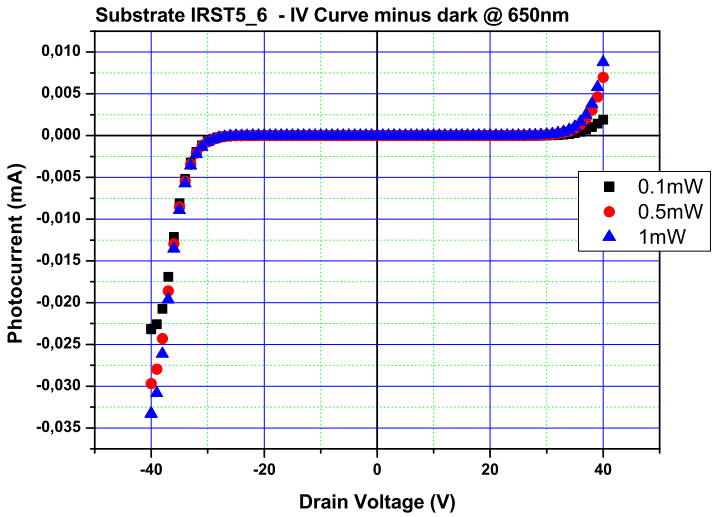

(b)

Figure 5.3: Dark current (a) and photocurrent (b) (the light wavelength is 650nm) of substrate IRST5-6.

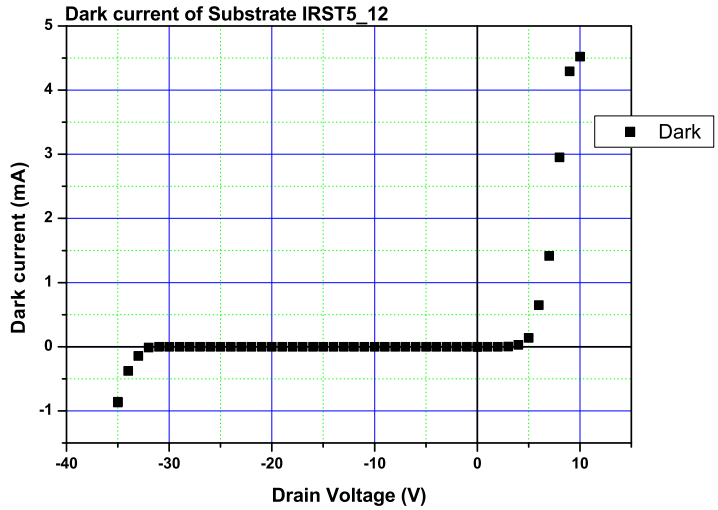

(a)

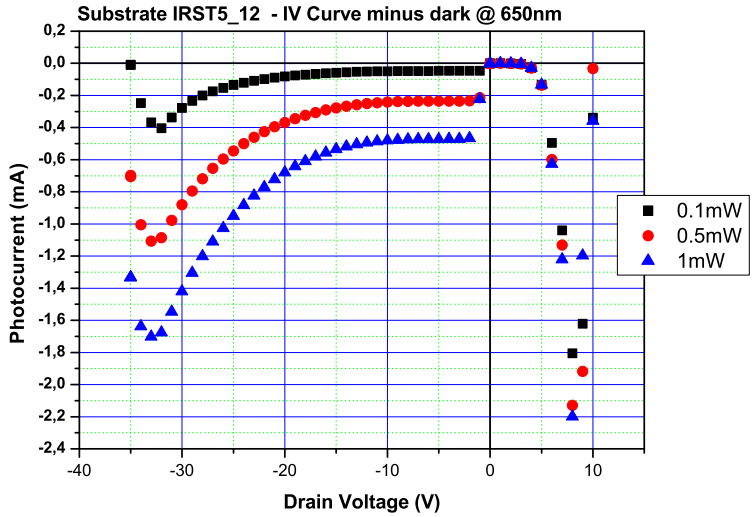

(b)

Figure 5.4: Dark current (a) and photocurrent (b) (the light wavelength is 650nm) of substrate IRST5-12.

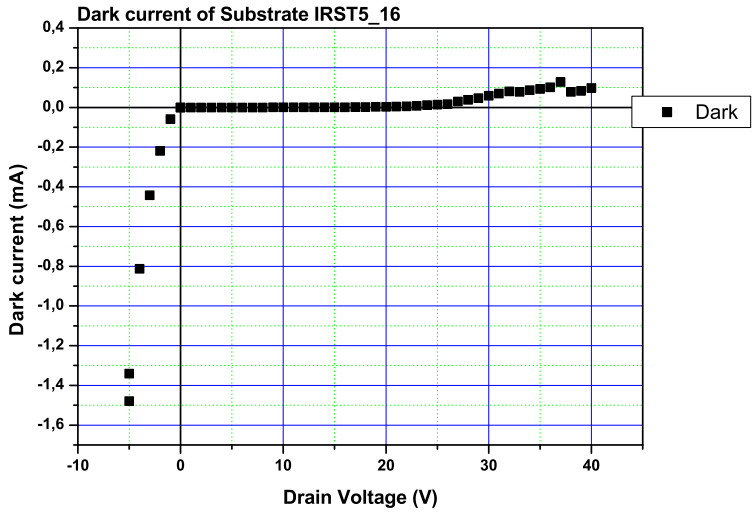

(a)

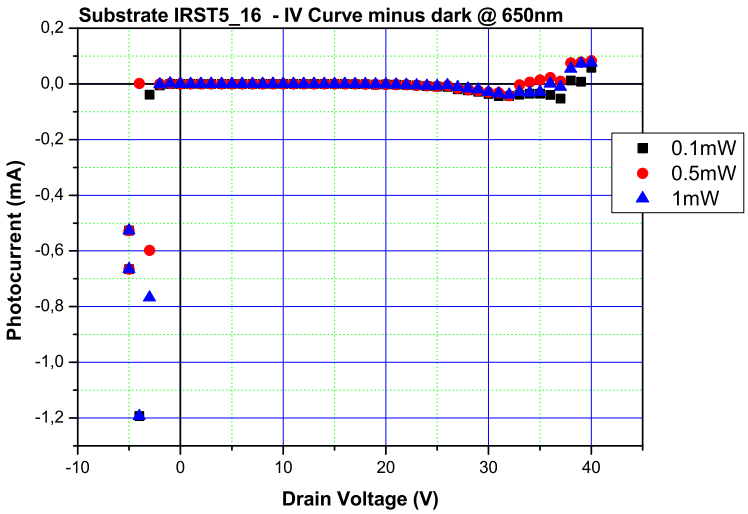

(b)

Figure 5.5: Dark current (a) and photocurrent (b) (the light wavelength is 650nm) of substrate IRST5-16.

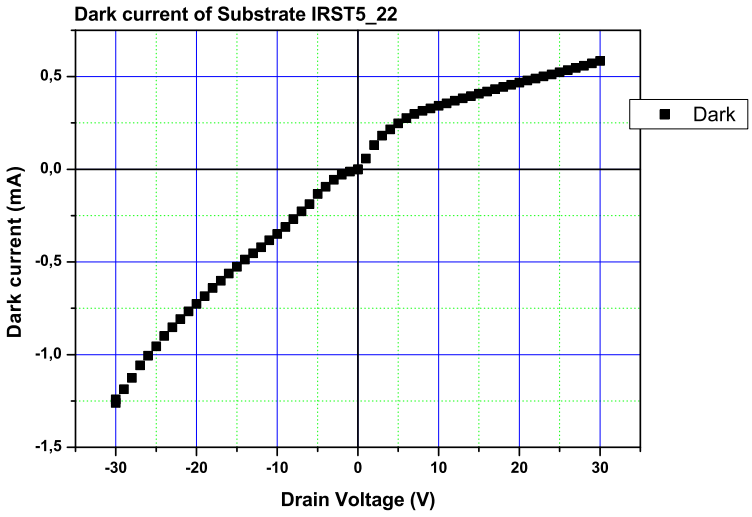

(a)

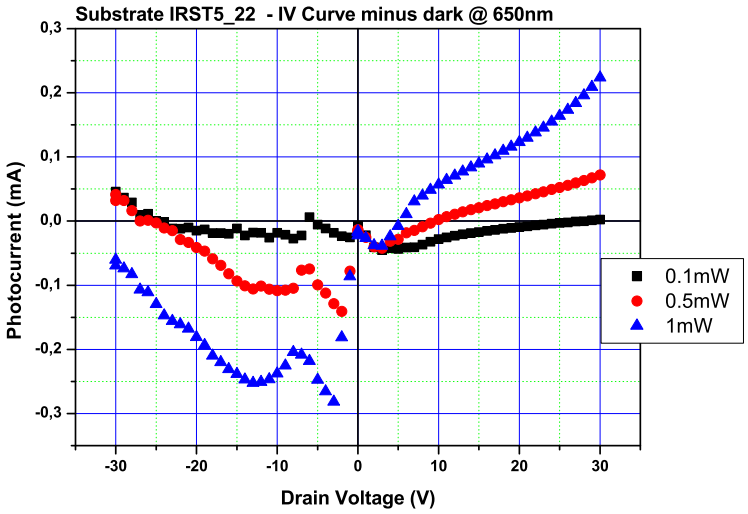

(b)

Figure 5.6: Dark current (a) and photocurrent (b) (the light wavelength is 650nm) of substrate IRST5-22.

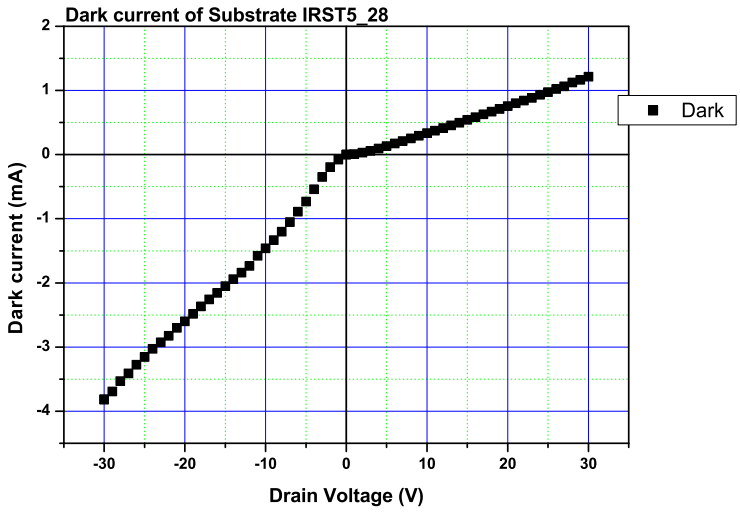

(a)

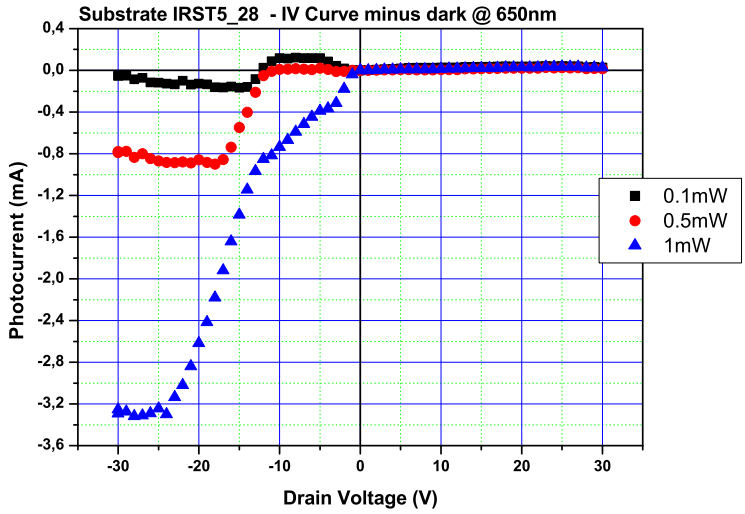

(b)

Figure 5.7: Dark current (a) and photocurrent (b) (the light wavelength is 650nm) of substrate IRST5-28.

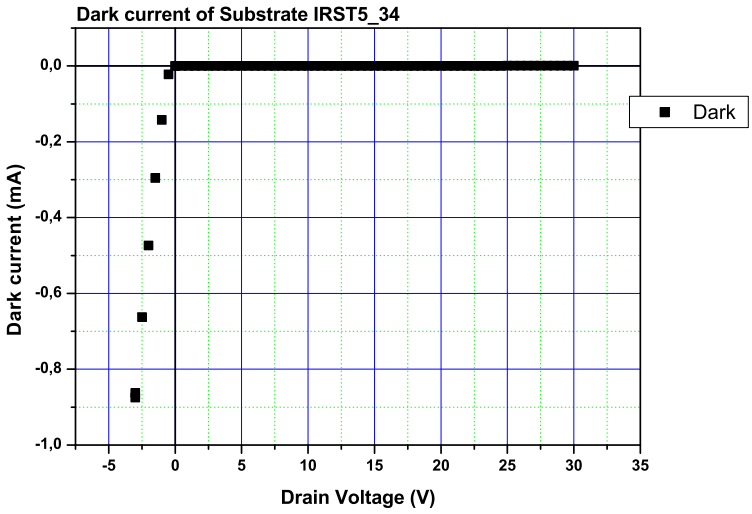

(a)

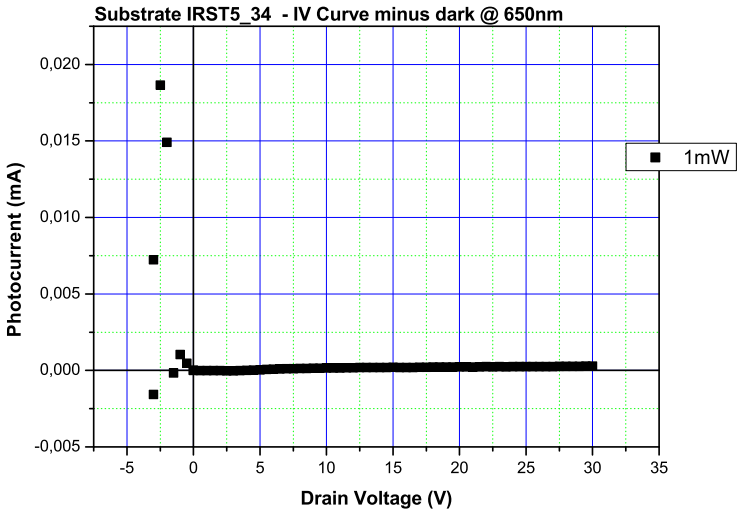

(b)

Figure 5.8: Dark current (a) and photocurrent (b) (the light wavelength is 650nm) of substrate IRST5-34.

5.2 Samples with multiwalled carbon nanotubes

On substrates shown in the previous section were grown MWCNTs by means of the CVD technique. In this section we report on the main characteristics of samples.

5.2.1 Dark current and Photocurrent

Measurements of dark currents are shown in Figures 5.10a, 5.11a, 5.12a, 5.13a, 5.14a, 5.15a, 5.16a, 5.17a, 5.18a, 5.19a, 5.20a, 5.21a, 5.22a, 5.23a. Measurements of photoresponses are shown in Figures 5.10b, 5.11b, 5.12b, 5.13b, 5.14b, 5.15b, 5.16b, 5.17b, 5.18b, 5.19b, 5.20b, 5.21b, 5.22b, 5.23b.

In the next lines we will report on the volt-amperometric characterization of devices with MWCNTs.

Sample IRST5-1a (measurements shown in Figures 5.10a,5.10b) exhibits a higher dark current than its substrate (Figure 5.2a), and a photoresponse similar to the substrate without nanotubes (Figure 5.2b).

Sample IRST5-5a (measurements shown in Figures 5.11a, 5.11b) exhibits a higher dark current than its substrate (Figure 5.3a), and a photoresponse, which is absent in the substrate without nanotubes (Figure 5.3b).

Sample IRST5-11a (measurements shown in Figures 5.13a, 5.13b) exhibits a dark current comparable with the substrate (Figure 5.4a), and a photoresponse comparable with the photoresponse of substrate without nanotubes (Figure 5.4b).

Sample IRST5-15a (measurements shown in Figures 5.15a, 5.15b) exhibits a dark current comparable with the substrate (Figure 5.5a), and a photoresponse, which is absent in the substrate without nanotubes (Figure 5.5b).

Sample IRST5-21a (measurements shown in Figures 5.18a, 5.18b) exhibits a dark current lower than exhibited by the substrate (Figure 5.6a), and a photoresponse higher then exhibited by the substrate without nanotubes (Figure 5.6b).

Sample IRST5-27a (measurements shown in Figures 5.19a, 5.19b) exhibits a dark current comparable with the substrate (Figure 5.7a), and an unstable photoresponse, which is absent in the substrate without nanotubes (Figure 5.7b).

Sample IRST5-33a (measurements shown in Figures 5.20a, 5.20b) exhibits a high dark current, respect to the substrate (Figure 5.8a), and a photoresponse, which is absent in the substrate without nanotubes (Figure 5.8b).

Sample IRST5-34a (measurements shown in Figures 5.24a, 5.24b) exhibits a dark current comparable with the substrate (Figure 5.9a), and a

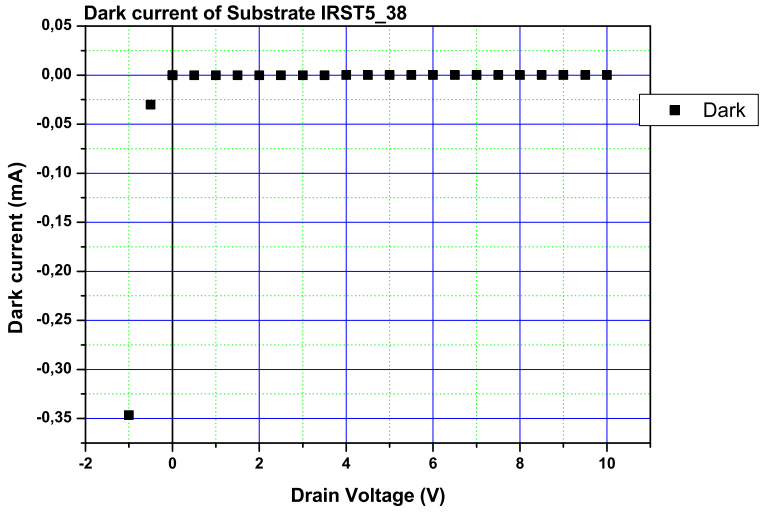

(a)

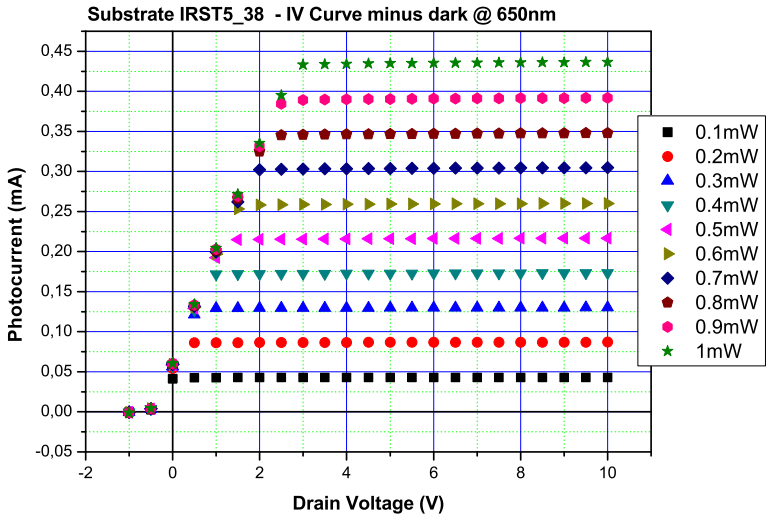

(b)

Figure 5.9: Dark current (a) and photocurrent (b) (the light wavelength is 650nm) of substrate IRST5-38.

photoresponse lower than the substrate (Figure 5.9b).

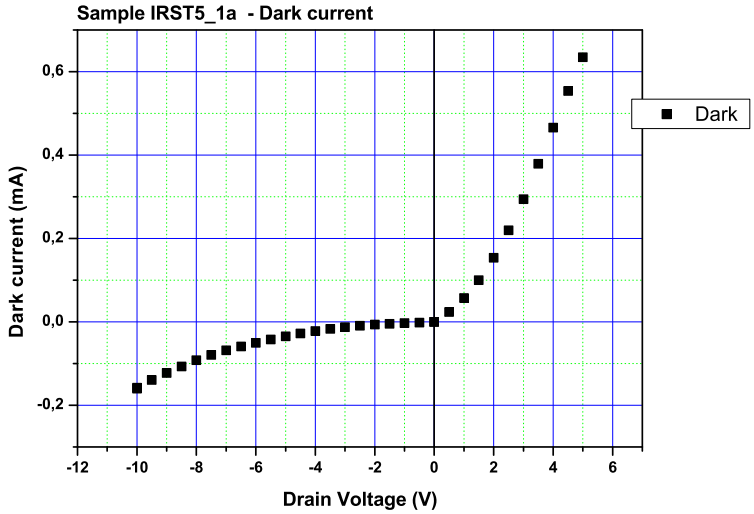

(a)

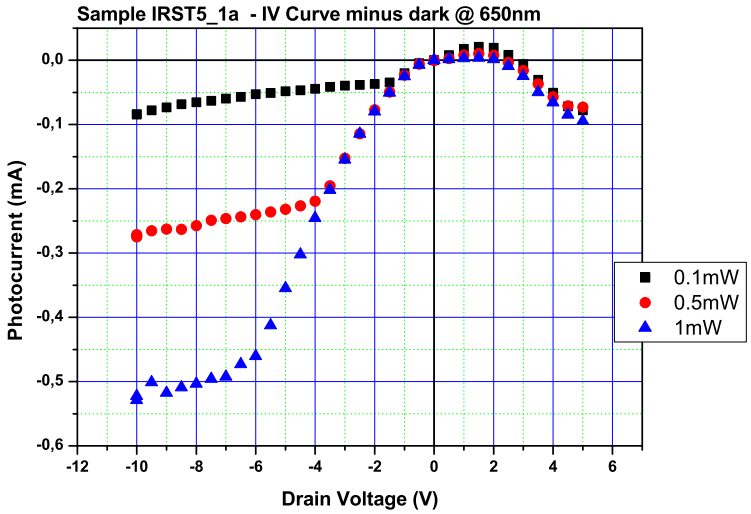

(b)

Figure 5.10: Dark current (a) and photocurrent (b) (the light wavelength is 650nm) of Sample IRST5-1a.

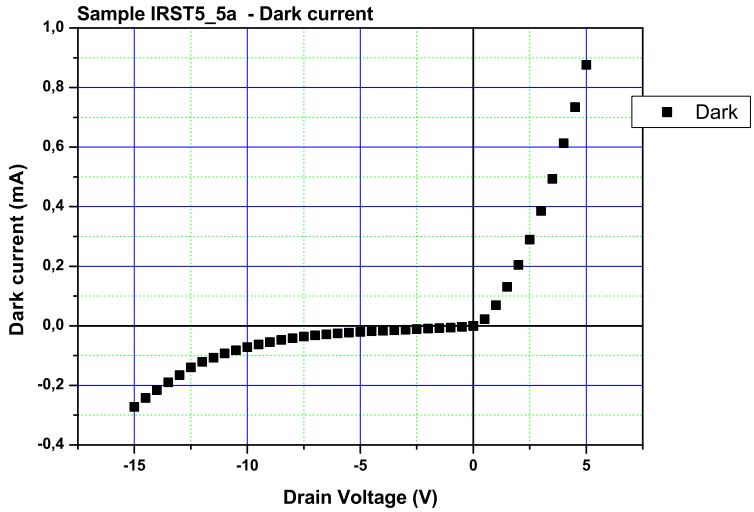

(a)

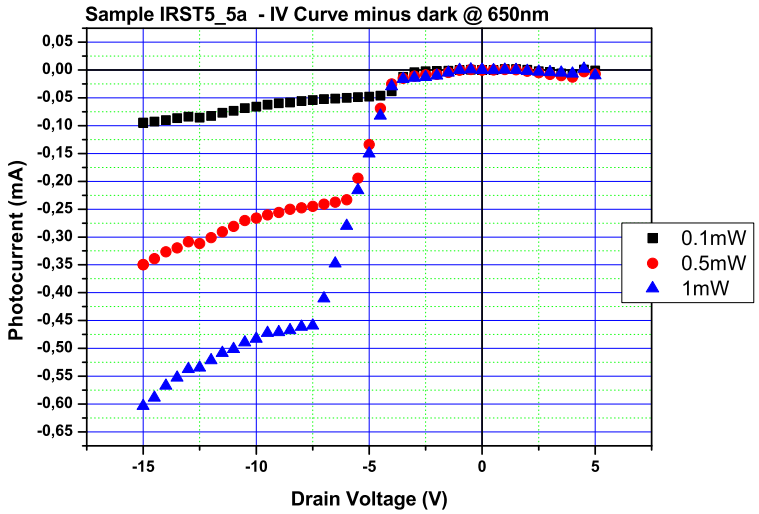

(b)

Figure 5.11: Dark current (a) and photocurrent (b) (the light wavelength is 650nm) of Sample IRST5-5a.

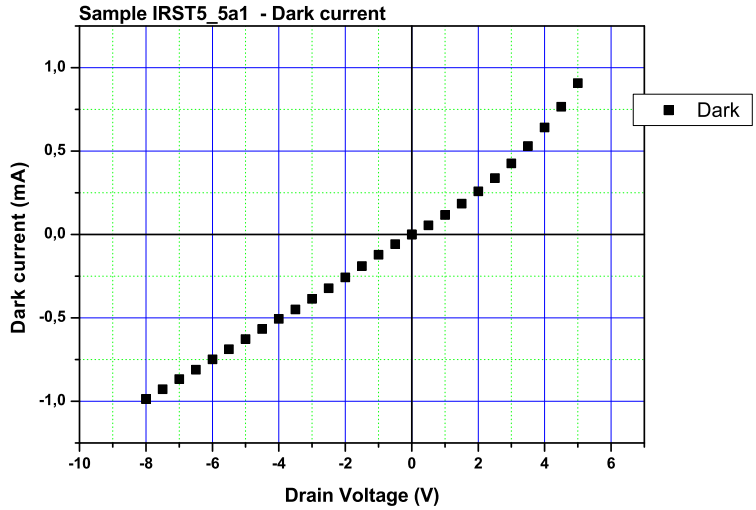

(a)

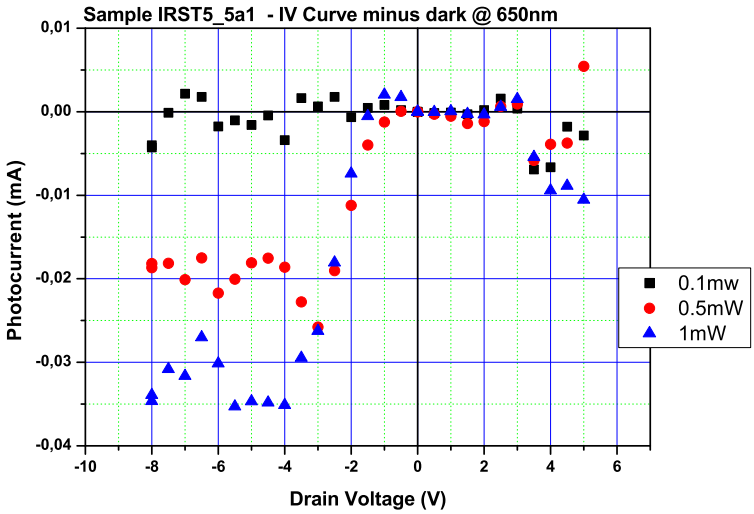

(b)

Figure 5.12: Dark current (a) and photocurrent (b) (the light wavelength is 650nm) of Sample IRST5-5a1.

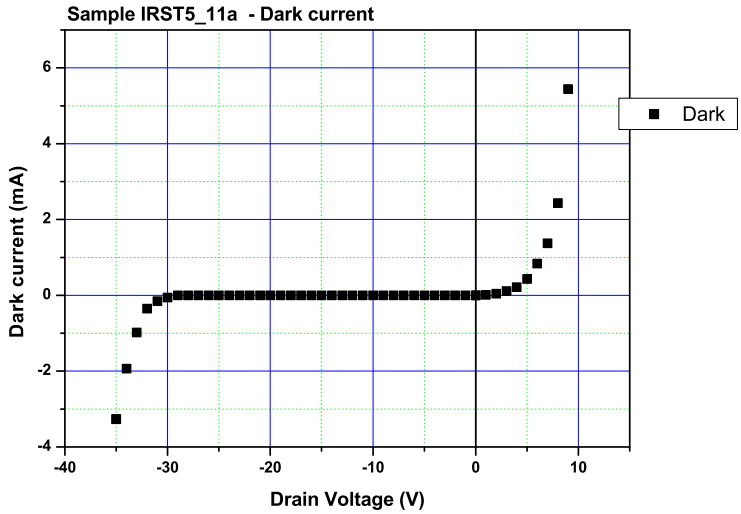

(a)

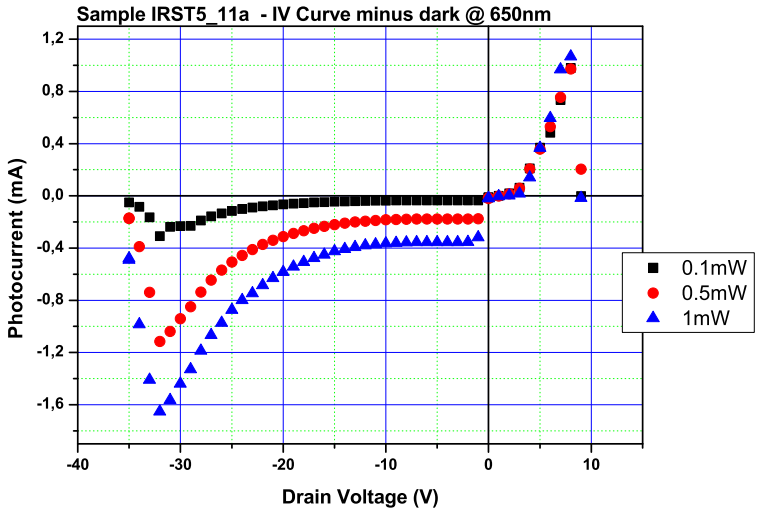

(b)

Figure 5.13: Dark current (a) and photocurrent (b) (the light wavelength is 650nm) of Sample IRST5-11a.

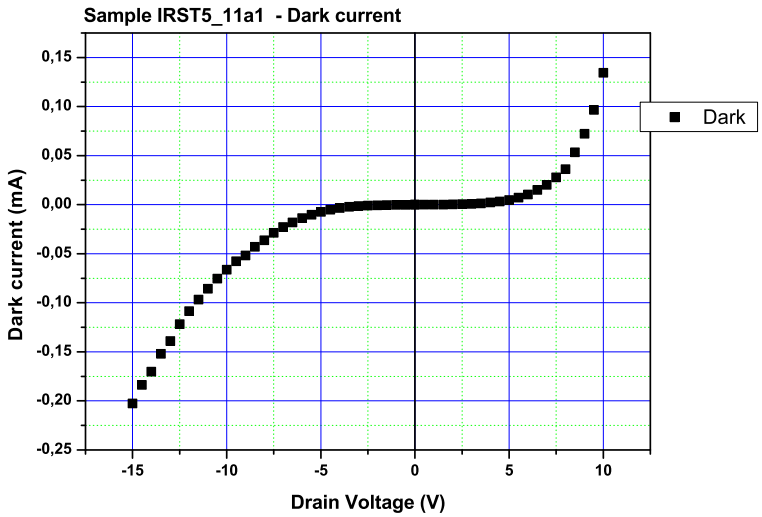

(a)

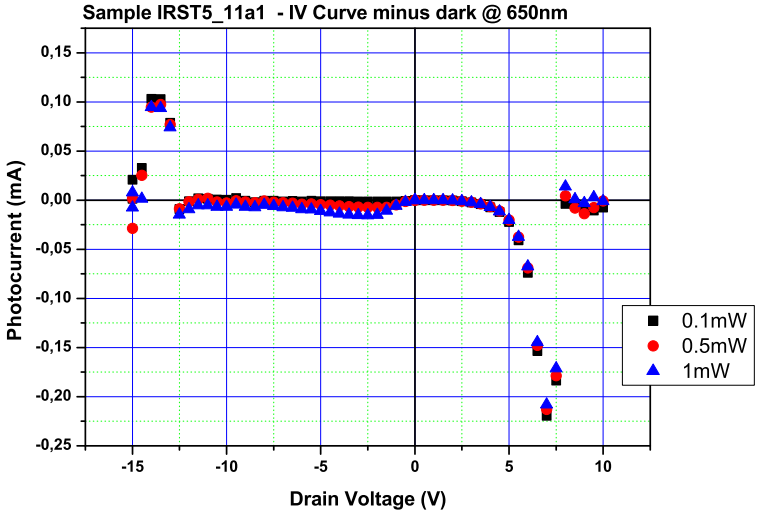

(b)

Figure 5.14: Dark current (a) and photocurrent (b) (the light wavelength is 650nm) of Sample IRST5-11a1.

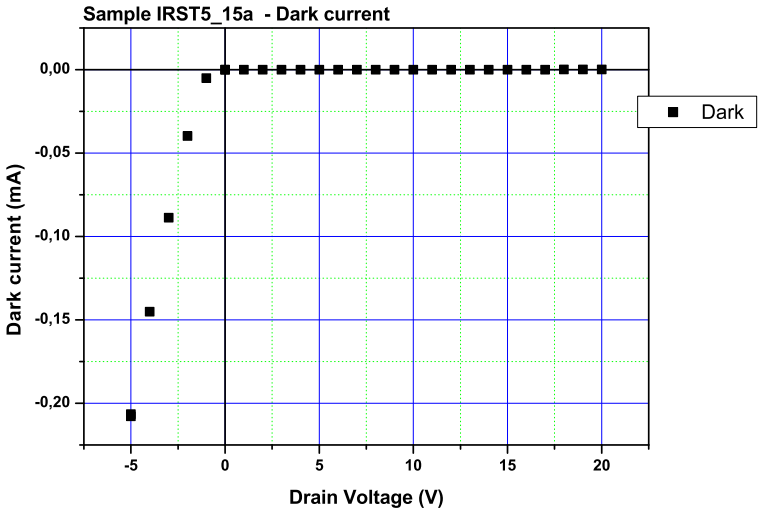

(a)

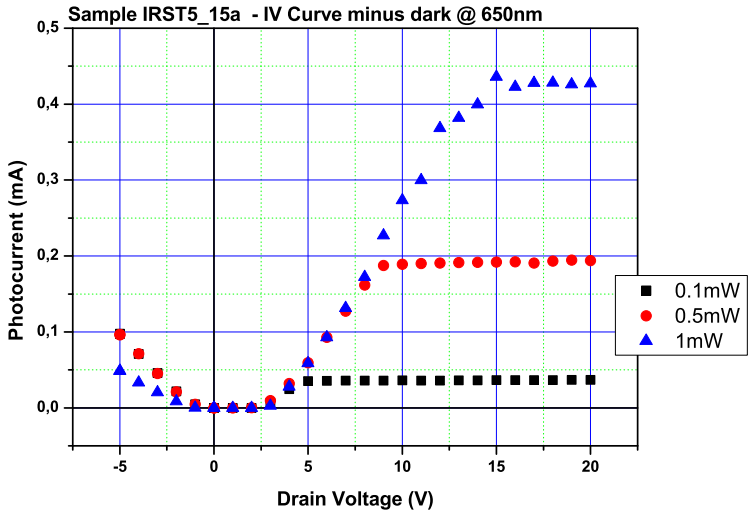

(b)

Figure 5.15: Dark current (a) and photocurrent (b) (the light wavelength is 650nm) of Sample IRST5-15a.

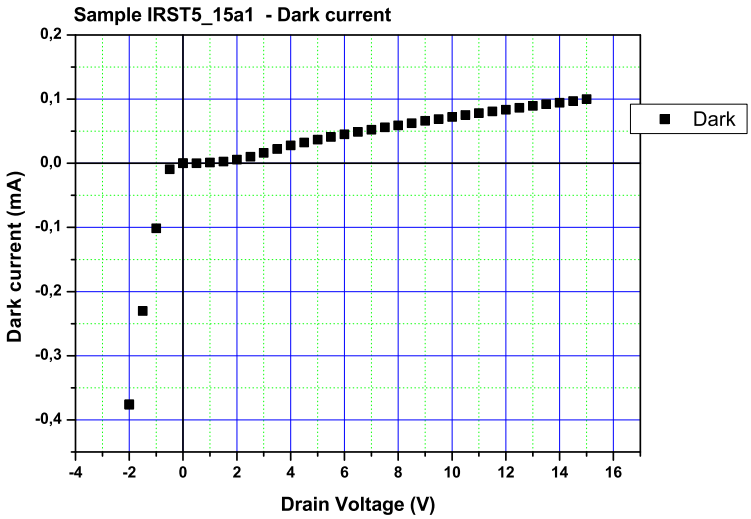

(a)

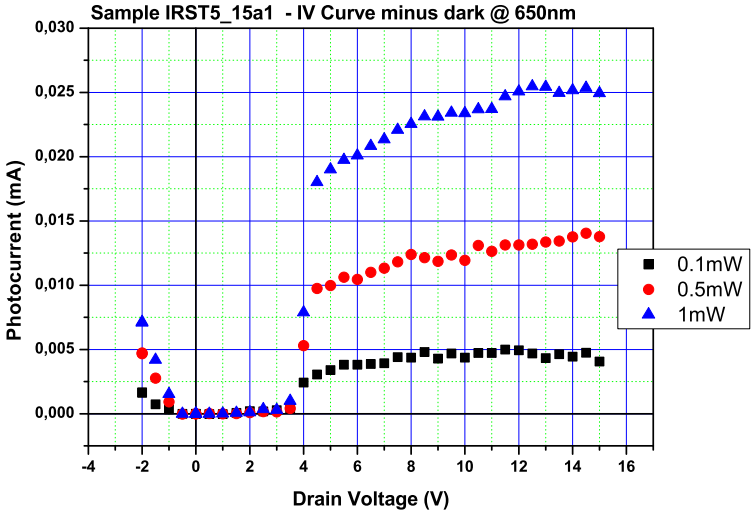

(b)

Figure 5.16: Dark current (a) and photocurrent (b) (the light wavelength is 650nm) of Sample IRST5-15a1.

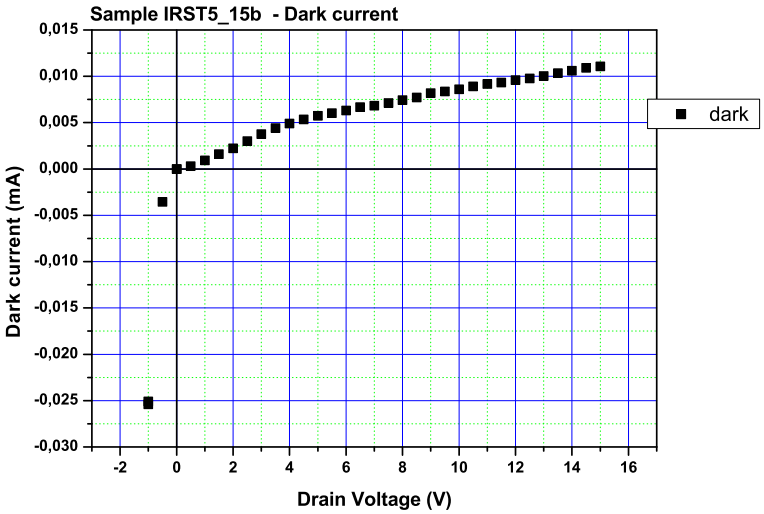

(a)

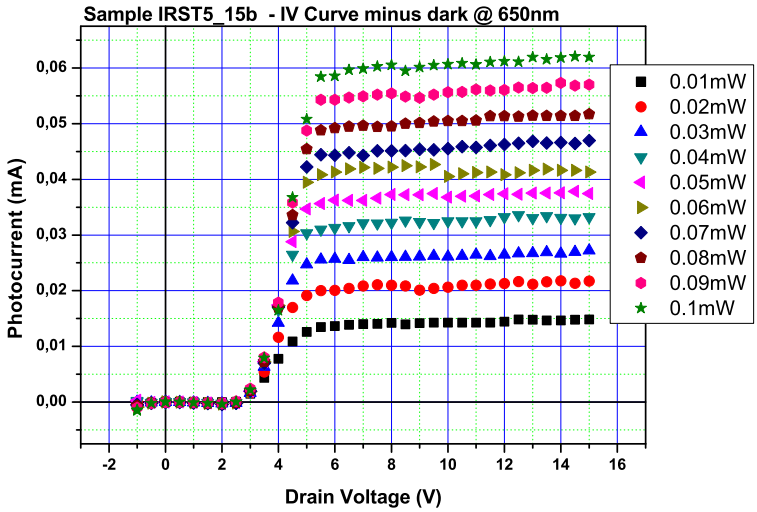

(b)

Figure 5.17: Dark current (a) and photocurrent (b) (the light wavelength is 650nm) of Sample IRST5-15b.

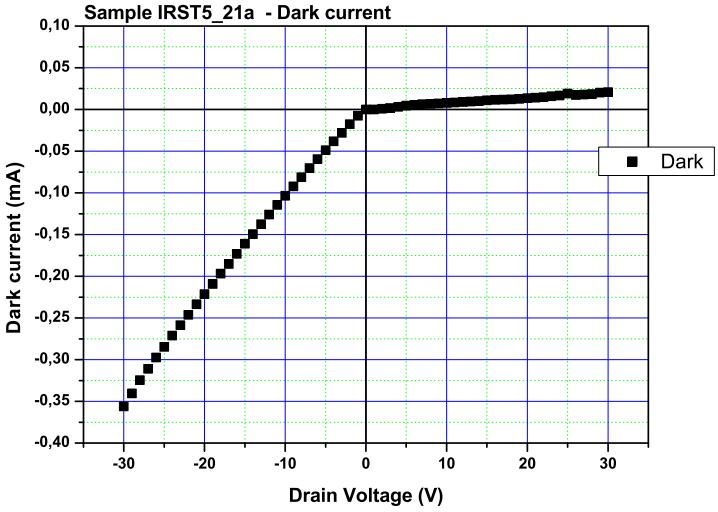

(a)

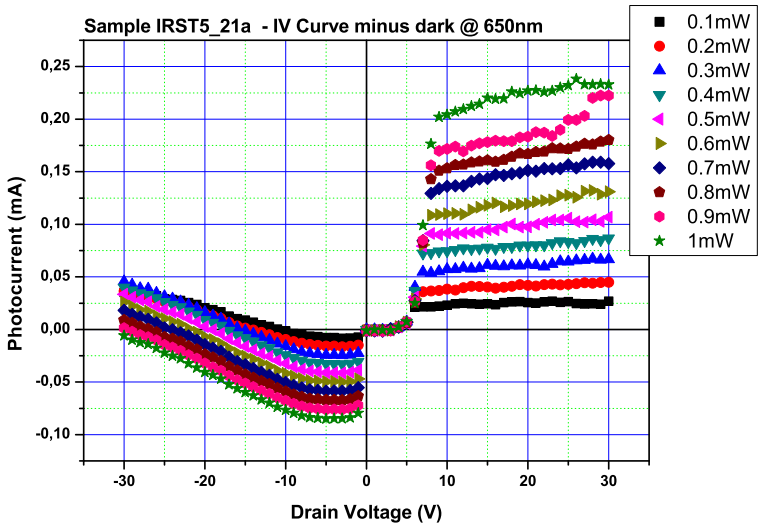

(b)

Figure 5.18: Dark current (a) and photocurrent (b) (the light wavelength is 650nm) of Sample IRST5-21a.

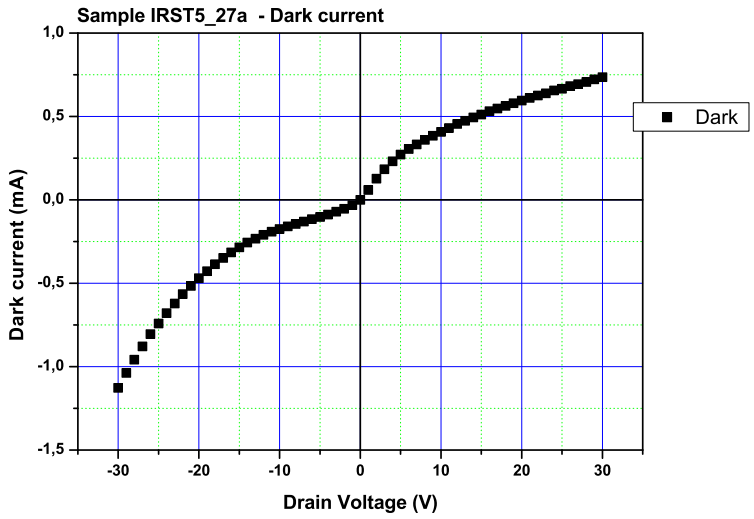

(a)

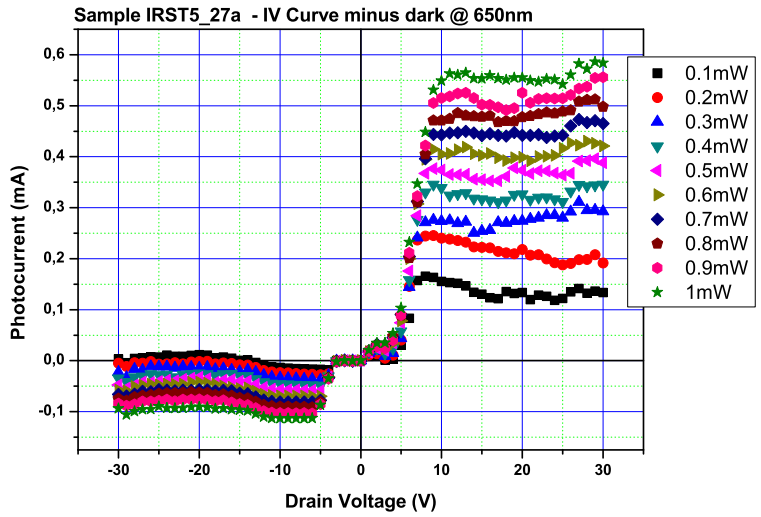

(b)

Figure 5.19: Dark current (a) and photocurrent (b) (the light wavelength is 650nm) of Sample IRST5-27a.

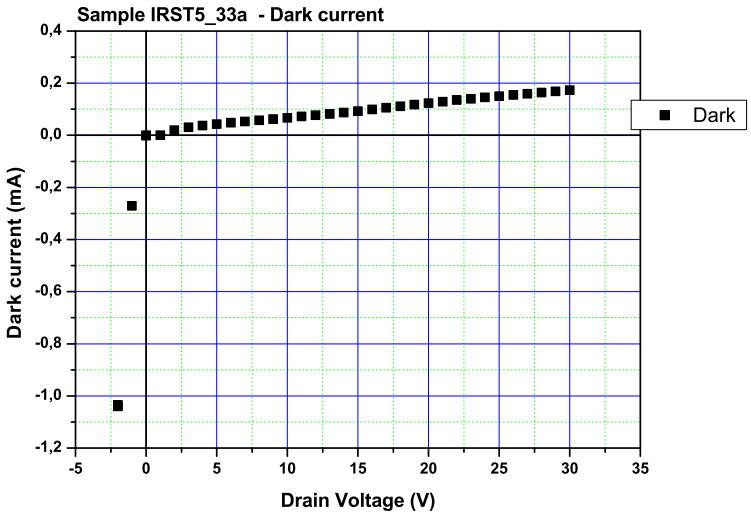

(a)

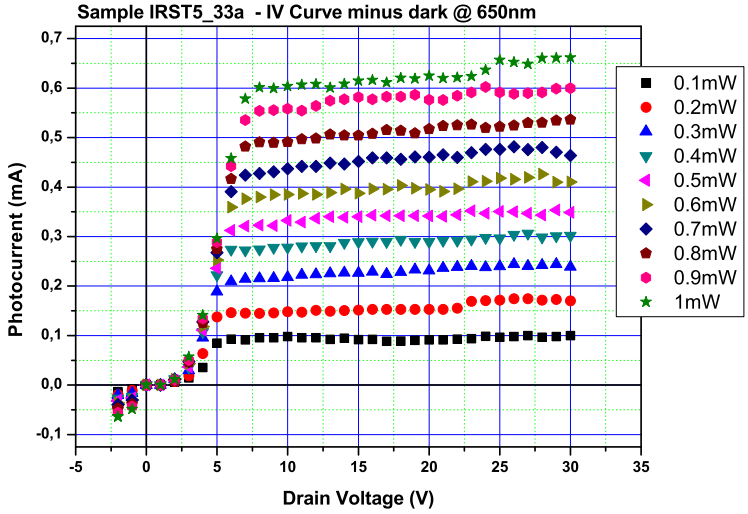

(b)

Figure 5.20: Dark current (a) and photocurrent (b) (the light wavelength is 650nm) of Sample IRST5-33a.

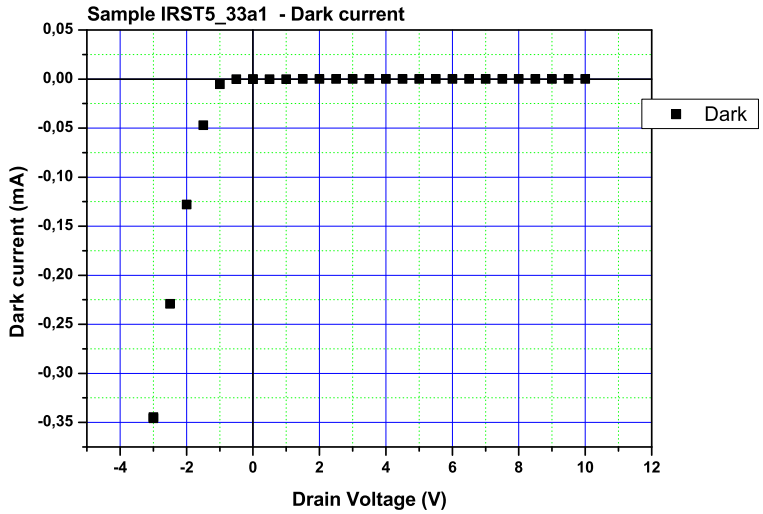

(a)

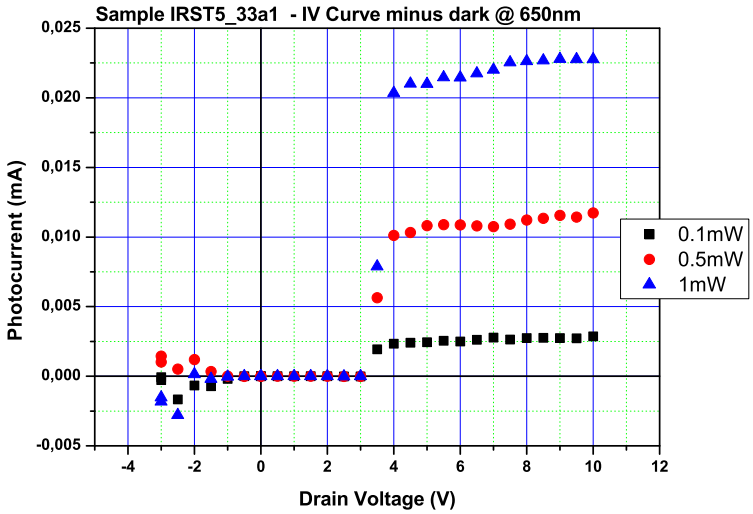

(b)

Figure 5.21: Dark current (a) and photocurrent (b) (the light wavelength is 650nm) of Sample IRST5-33a1.

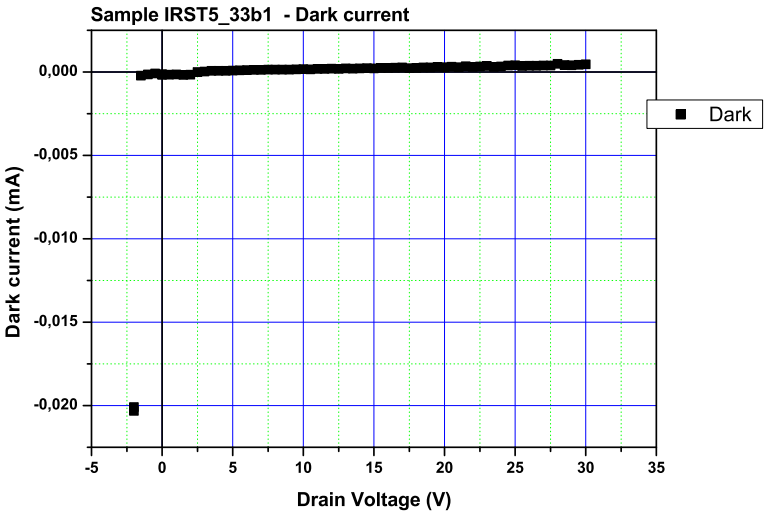

(a)

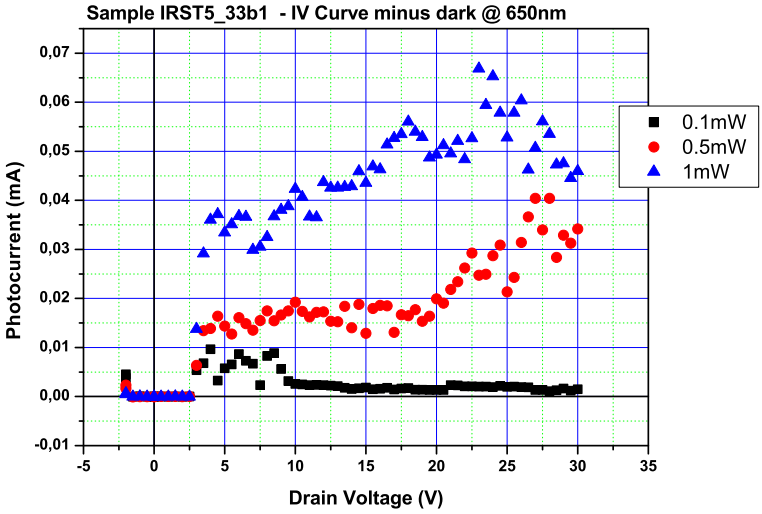

(b)

Figure 5.22: Dark current (a) and photocurrent (b) (the light wavelength is 650nm) of Sample IRST5-33b1.

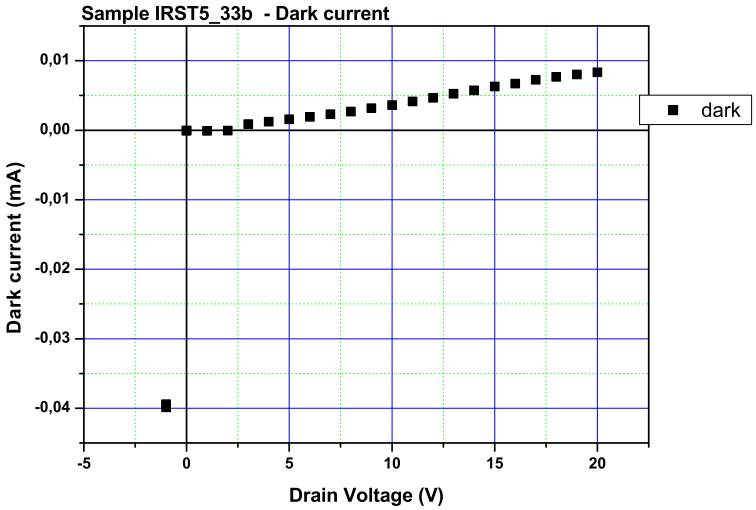

(a)

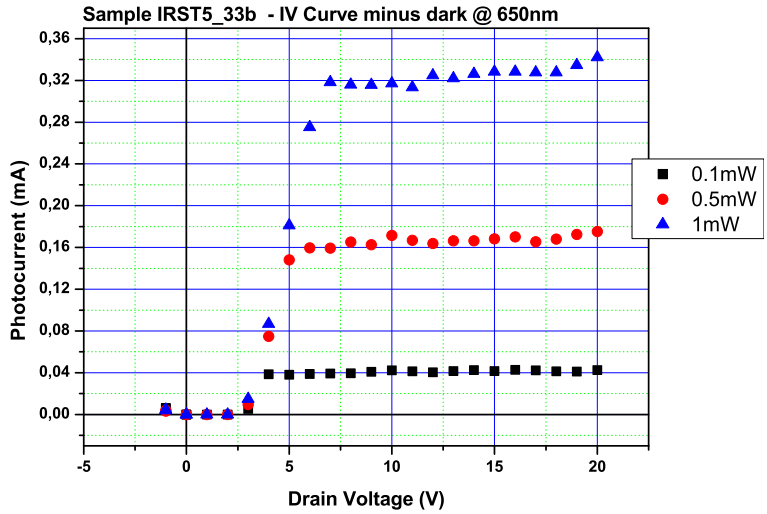

(b)

Figure 5.23: Dark current (a) and photocurrent (b) (the light wavelength is 650nm) of Sample IRST5-33b.

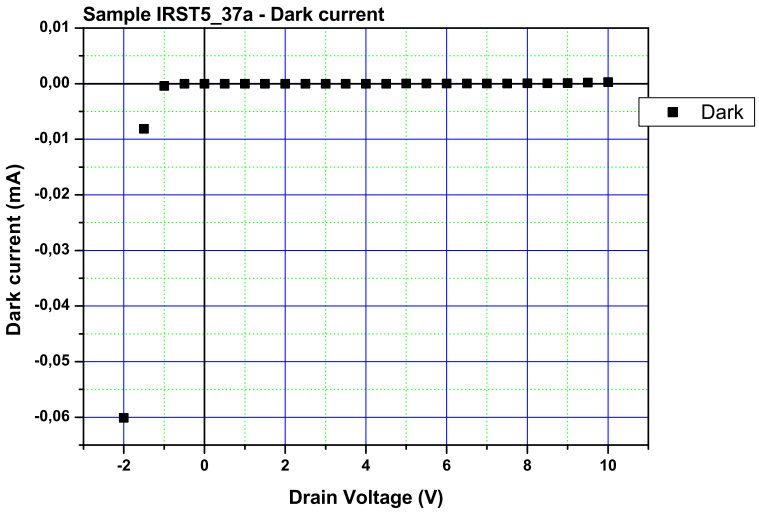

(a)

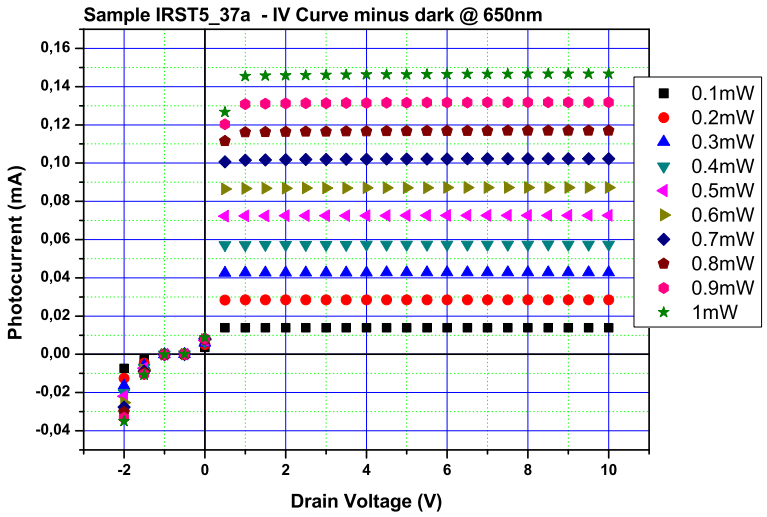

(b)

Figure 5.24: Dark current (a) and photocurrent (b) (the light wavelength is 650nm) of Sample IRST5-37a.

5.2.2 Capacitance

Capacitance versus voltage measurements provide a wealth of information about device and material characteristics. Capacitance-voltage (C-V) testing is widely used to determine semiconductor parameters, particularly in Metal Oxide Semiconductor Capacitor (MOSCAP) and Metal-Oxide-Semiconductor Field-Effect Transistor (MOSFET) structures. However, other types of semiconductor devices and technologies can also be characterized with C-V measurements, including Bipolar Junction Transistors (BJT), Junction gate Field-Effect Transistors (JFET), III-V compound devices, photovoltaic cells, Micro Electro-Mechanical Systems (MEMS) devices, photodiodes, carbon nanotubes, and many others. The fundamental nature of these measurements makes them useful in a wide range of applications and disciplines. They are used in the research labs of universities and semiconductor manufacturers to evaluate new materials, processes, devices, and circuits. C-V measurements are extremely important to product and yield enhancement engineers, who are responsible for improving processes and device performance. Reliability engineers use these measurements to qualify material suppliers, monitor process parameters, and analyze failure mechanisms. With appropriate methodologies, instrumentation, and software, a multitude of semiconductor device and material parameters can be derived. This information is used all along the production chain beginning with evaluation of epitaxially grown crystals, including parameters such as average doping concentration, doping profiles, and carrier lifetimes. In wafer processes, C-V measurements can reveal oxide thickness, oxide charges, mobile ions (contamination), and interface trap density. These measurements continue to be used after other process steps, such as lithography, etching, cleaning, dielectric and polysilicon depositions, and metallization. After devices are fully fabricated on the wafer, C-V is used to characterize threshold voltages and other parameters during reliability and basic device testing and to model the performance of these devices.

We measured the capacitance of the structure shown in Figure 5.25, Sample IRST5-15b.

The MWCNTs layer shown in Figure 5.25 is one plate of the capacitor, and silicon nitride is the insulator. Since the substrate below the insulating layer is a semiconducting material, it is not by itself the other plate of the capacitor. In effect, the majority charge carriers become the other plate. Physically, capacitance, C, is determined from the variables in the following equation:

$$C = A\frac{k}{d} \tag{5.1}$$

where:

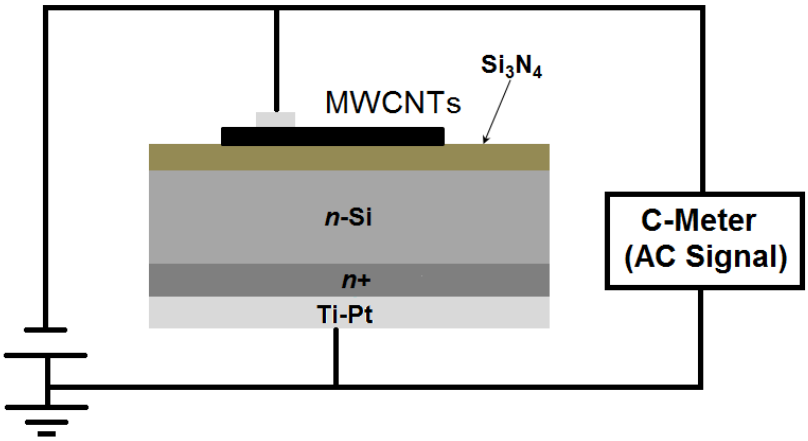

Figure 5.25: *Experimental setup of the measurement of capacity vs voltage.*

- A is the area of the capacitor;
- k is the dielectric constant of the insulator;
- d is the separation of the two plates.

Therefore, the larger A and k are, and the thinner the insulator is, the higher the capacitance will be. Typically, semiconductor capacitance values range from nanofarads to picofarads, or smaller. The procedure for taking C-V measurements involves the application of DC bias voltages across the capacitor while making the measurements with an AC signal (Figure 5.26). Commonly, AC frequencies from about 10kHz to 10MHz are used for these measurements. The bias is applied as a DC voltage sweep that drives the photodetector structure from its accumulation region into the depletion region, and then into inversion.

A strong DC bias causes majority carriers in the substrate to accumulate near the insulator interface. Since they can't get through the insulating layer, capacitance is at a maximum in the accumulation region as the charges stack up near that interface (i.e., d is at a minimum). One of the fundamental parameters that can be derived from C-V accumulation measurements is the silicon dioxide thickness. As bias voltage is decreased, majority carriers get pushed away from the oxide interface and the depletion region forms. When the bias voltage is reversed, charge carriers move the greatest distance from the oxide layer, and capacitance is at a minimum (i.e., d is at a maximum). From this inversion region capacitance, the number of majority carriers can be derived. Many other parameters can be derived from the three regions

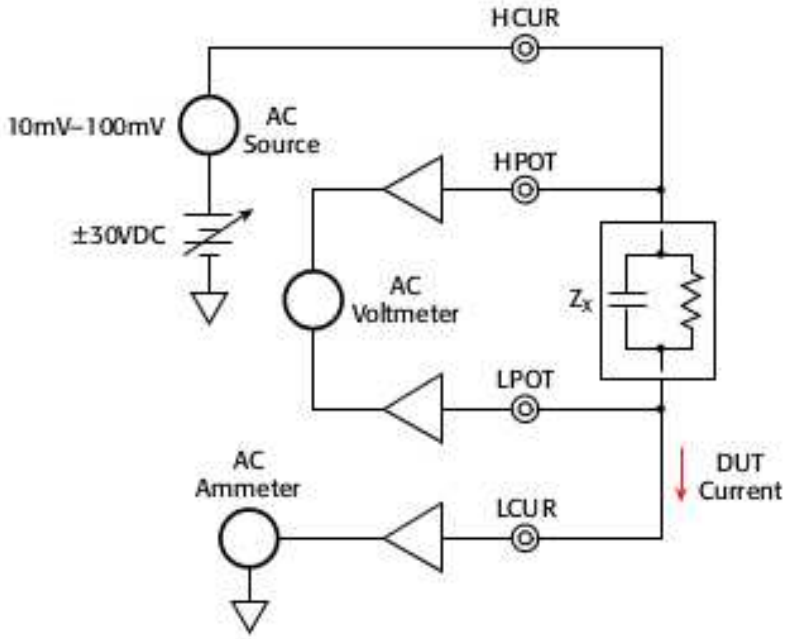

Figure 5.26: *Basic test setup for C-V measurements.*

shown in Figure 5.25 as the bias voltage is swept through them. Different AC signal frequencies can reveal additional details. Low frequencies reveal what are called quasistatic characteristics, whereas high frequency testing is more indicative of dynamic performance. Both types of C-V testing are often required.

Figure 5.26 is the block diagram of a basic C-V measurement setup. Because C-V measurements are actually made at AC frequencies, the capacitance for the device under test (DUT) is calculated with the following:

$$C_{DUT} = \frac{I_{DUT}}{2\pi f V_{ac}} \tag{5.2}$$

- I_{DUT} s the magnitude of the AC current through the DUT;
- f is the test frequency;
- V_{AC} is the magnitude and phase angle of the measured AC voltage.

In other words, the test measures the AC impedance of the DUT by applying an AC voltage and measuring the resulting AC current, AC voltage, and impedance phase angle between them. These measurements take into account

series and parallel resistance associated with the capacitance, as well as the dissipation factor (leakage).

The measurement performed on Sample IRST5-15b is shown in Figure 5.27, where it is evident the presence of the junction between the MWCNTs and the Silicon, with a threshold at around 2V confirming which is obtained by the I-V measurements.

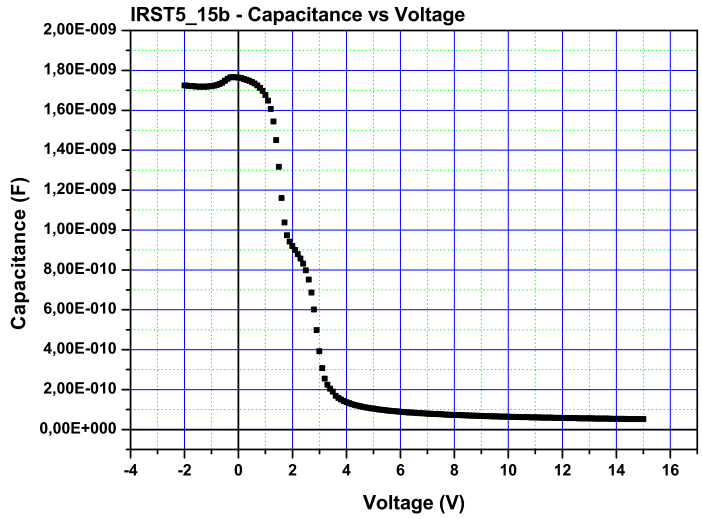

Figure 5.27: *DC bias sweep structure obtained during C-V testing.*

5.2.3 Quantum Efficiency

This section shows quantum efficiencies of samples that showed interesting photoresponses respect to the responses of substrates. Measurements of quantum efficiencies are shown in figures 5.28, 5.29, 5.30, 5.31. In particular, samples IRST5-15b and IRST5-33a show an interesting mechanism of charge multiplication, probably due to the presence of the carbon nanostructures on the substrate.

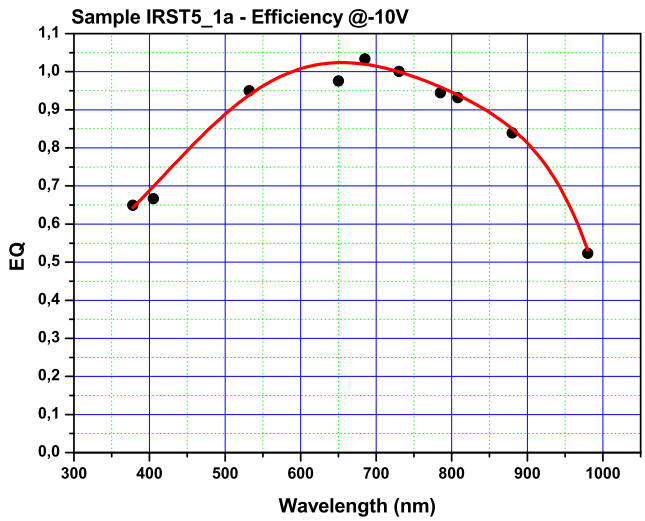

Figure 5.28: *Quantum efficiency of Sample IRST5-1a*

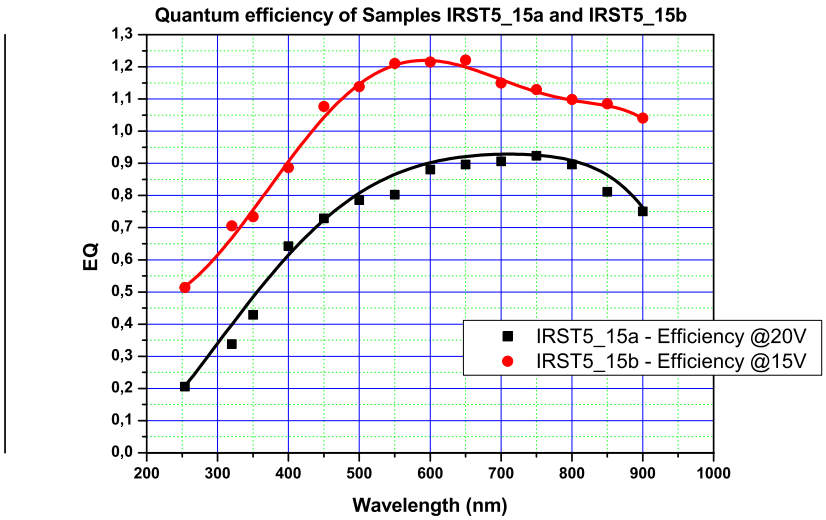

Figure 5.29: *Quantum efficiencies of Samples IRST5-15a and IRST5-15b.*

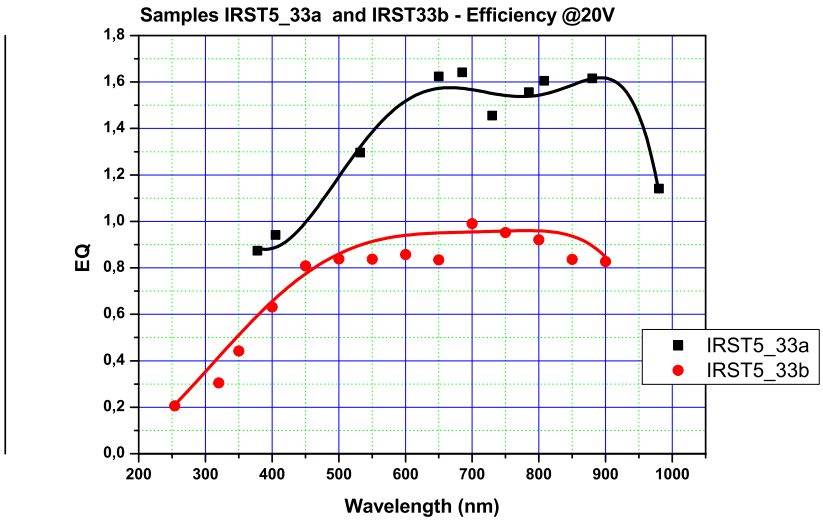

Figure 5.30: *Quantum efficiencies of Samples IRST5-33a and IRST5-33b.*

5.3 Comparison with standard solid-state photodetectors

In this section we discuss the characteristics of the most interesting Samples with MWCNTs (Samples IRST5-15a, IRST5-15b and IRST5-33a) and com-

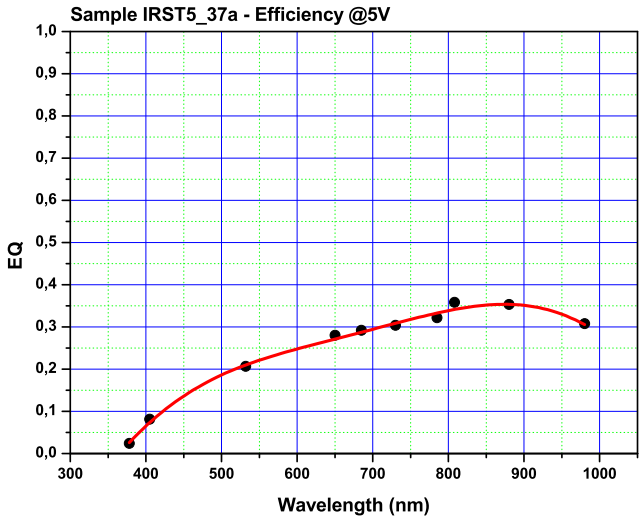

Figure 5.31: *Quantum efficiency of Sample IRST5-37a*

pare them with commercial photodetectors. Characteristics compared are dark currents and quantum efficiencies.

Dark currents comparison

In Figure 5.32 are shown the dark currents, in logarithmic scale, of Samples IRST5-15a, IRST5-15b and IRST5-33a. Also in this case, as in the case of photodetectors shown in Chapter 4, Samples with the same substrate (IRST5-15a and IRST5-15b) and the same growth parameters of MWCNTs shown strongly different dark currents. In particular, for Sample IRST5-15a we have, at the operating voltage (20V), a dark current of about 100pA, and for Sample IRST5-15b, at the operating voltage (15V), we have a dark current of about 0.01mA, which is two orders of magnitude greater. Compared with Samples shown in Chapter 4, the IRST production has showed lower dark currents.

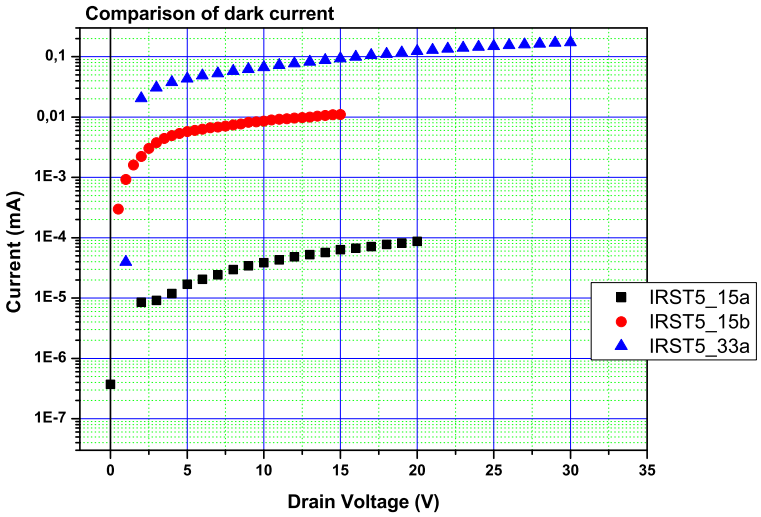

Figure 5.32: *Dark currents comparison.*

Spectral response comparition

Now we compare spectral responses of Samples with MWCNTs (Figure 5.33) with spectral responses of standard photodiodes (Figure 5.34). As already mentioned in section 2.2.2 and 2.4 the spectral response of photodiodes is expressed in spectral responsivity.

Figure 5.34 shows measured spectral dependence of various kinds of commercial photodiodes expressed in spectral responsivity. For ordinary photodiodes, the cut-off wavelength on the short wavelength side is 320nm, whereas it is 190nm for UV-enhanced Si photodiodes. In the case of silicon at room temperature, the band gap energy is 1.12eV, so the cut-off wavelength in the IR region is 1100nm. The BQ type uses a quartz window, the BK type a borosilicate glass window, and the BR type a resin-coated window. The S9219 is a Si photodiode with a visual-sensitive compensation filter.

With the IRST production were achieved surprising results in terms of spectral responses. Infact, as reported in Section 5.2.3, some samples with MWCNTs showed internal mechanisms of amplification in the spectral range from 450 to 1000 nm. Unfortunately a theoretical interpretation has not yet been found to justify this surprising phenomenon. It should also be noted that in terms of response in the ultraviolet region, these samples are comparable to the commercial photodiodes, unlike those reported in Chapter 4.

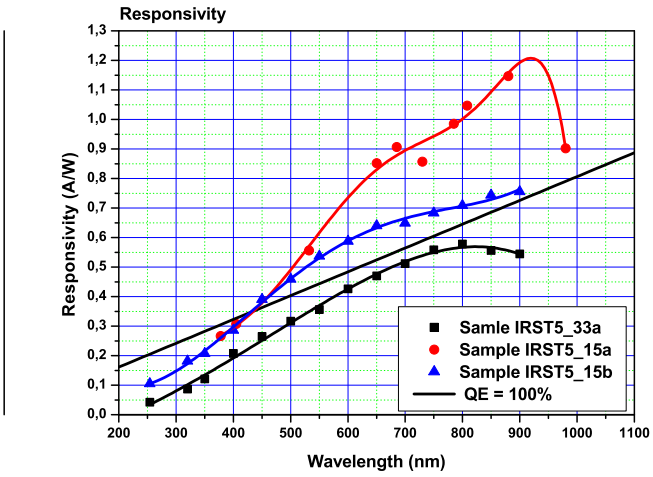

Figure 5.33: *Spectral response of Samples with carbon nanostructures. The black solid line is the quantum efficiency at 100%.*

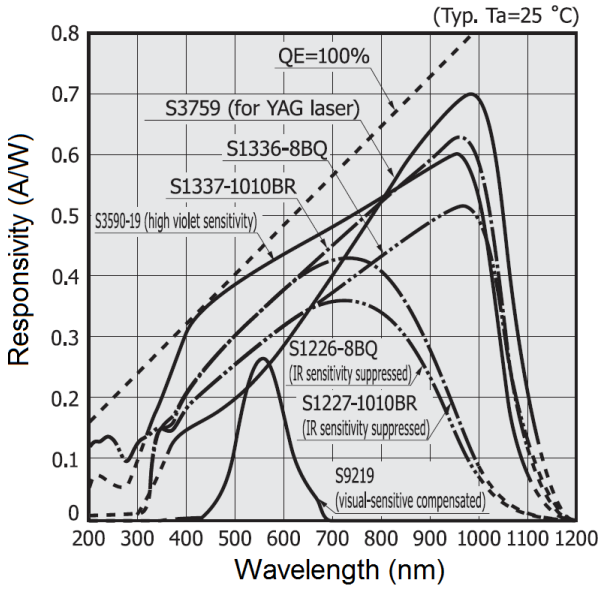

Figure 5.34: *Typical spectral response of commercial silicon photodiodes. The dashed black line is the quantum efficiency at 100%. (From Hamammatsu catalog).*

Conclusions

The purpose of this PhD thesis has been the development of a new solid-state photodetector based on the use of carbon nanotubes grown on doped silicon substrates. CNT films can be easily grown on large area creating a large photocathode with unique and precious characteristics: low cost, high quantum efficiency, high linearity, and stable at room temperature.

It has been demonstrated that the heterojunction created between a film of carbon nanotubes and silicon generates a light sensitive detector with good quantum efficiency in the visible range. In fact the CNT layer absorbs photons producing electron-hole pairs that can be separated by the CNT film and the electrical field inside the depletion zone of the heterojunction. The charge produces a photocurrent drained out by the applied voltage.

The CNT layer have been covered by an electrically conductive layer to avoid the nanotube detachment from the silicon substrate and uniformly transmit the electric field to the entire active surface.

It was found that dark current measurements are well explained by assuming that the charge transport is controlled by tunneling between carbon nanostructures and silicon. Starting from this observation, a first model has been proposed. In order to simulate the devices behavior, we started with an equivalent circuit: once the parameter values are fixed we are able to reproduce the current-voltage characteristics, both in dark conditions and under illumination for different light intensities.

After the characterization and the study of samples shown in Chapter 4, a series of substrates have been made, some with internal junctions in the order to obtain an internal amplification. The surprising result of this research has been that substrates with internal junctions and covered with CNTs do not showed mechanisms of internal charge multiplication, but simple substrates and without internal junctions have shown mechanisms of charge multiplication. This phenomenon probably is due to the presence of the film of CNTs. In this scenario the main problem has been the reproducibility of the phenomenon of charge multiplication, because samples with the same substrate and growth parameters of CNTs showed very different characteristics. At present, from the theoretical point of view, a serious study has not been done, but this discovery could open the door to a new generation of photodetectors.

Bibliography

[1] N. W. Ashcroft, N. D. Mermin. Cengage Learning Emea (1976).

[2] Charles Kittel. Introduction to Solid State Physics (Seventh ed.). New York: Wiley (1996).

[3] W. Shockley, "The Theory of p-n Junctions in Semiconductors and p-n Junction Transistors", Bell Syst. Tech. J., 28,435 (1949).

[4] W. Shockley, "Electrons and Holes in Semiconductors", D. Van Nostrand, Princeton, New Jersey, 1950.

[5] C. T. Sah, R. N. Noyce, and W. Shockley, "Carrier Generation and Recombination in p-n Junction and p-n Junction Characteristics", Proc. IRE, 45, 1228 (1957).

[6] J. L. Moll, "The Evolution of the Theory of the Current-Voltage Characteristics of p-n Junctions", Proc. IRE, 46, 1076 (1958).

[7] S. Iijima. Nature, 354, 56-58, 1991.

[8] S. Iijima and T. Ichihashi. Nature, 363, 603-605, 1993.

[9] D. S. Bethune, C. H. Kiang, M. S. Devries, G. Gorman, R. Savoy, and J. Vazquez. Nature, 363, 605-607, 1993.

[10] A. Oberlin, M. Endo, and T. J. Koyama. J. Cryst. Growth, 32:335-349, 1976.

[11] M.P. Anantram and F. L'onard. Rep. Prog. Phys. 69 (2006) 507-561.

[12] White C.T. and Todorov T.N. 1998 Nature 393 240.

[13] Radiation Detection and Measurement (2nd Edition) by Glenn F. Knoll, New York: John Wiley and Sons, 1989.

[14] M. DiDomenico, Jr. and 0. Svelto, "Solid State Photodetection Comparison between Photodiodes and Photoconductors" Proc. IEEE, 52, 136 (1964).

[15] A. Van der Ziel, Fluctuation Phenomena in Semiconductors, Academic, New York, 1959.

[16] Anderson, R. L., (1960). Germanium-gallium arsenide heterojunction, IBM J. Res. Dev. 4(3), pp. 283-287.

[17] W. Shockley, US.Patent 2,569,347 (1951).

[18] R. L. Anderson, "Experiments on Ge-GaAs Heterojunctions", Solid-state Electron., 5,341 (1962).

[19] S. M. Sze, K. K. Ng, "Physics of Semiconductor Devices" John Wiley & Sons, Inc. (2007).

[20] B. E. A. Saleh, M. C. Teich, "FUNDAMENTALS OF PHOTONICS", John Wiley & Sons, Inc. (1991).

[21] Golovin, V. et al. Patent of Russia, 1644708 (1989).

[22] R. Saito, G. Dresselhaus, M.S. Dresselhaus, Physical Properties of Carbon Nanotubes, Imperial College Press, 2003.

[23] R. Gao, Z. Pan, and Z. L. Wang, Appl. Phys. Lett. 78, 1757 2001.

[24] M. Shiraishi and M. Ata, Carbon 39, 1913 2001.

[25] S. Reich, C. Thomsen, J. Maultzsch, Carbon Nanotubes: Basic Concepts and Physical Properties, Wiley-VCH, 2003.

[26] C. Aramo et al. Innovative carbon nanotube-silicon large area photodetector, 2012 JINST 7 P08013.

[27] C. Aramo et al.Progress in the realization of a silicon-CNT photodetector, Nuclear Instruments and Methods in Physics Research A 695 (2012) 150-153.

[28] I.M. Xu, Infrared Phys. Technol. 42 (2001) 485.

[29] M.E. Itkis, Science 312 (2006) 413.

[30] Shaoxin Lu, et al., Nanotechnology 17 (2006) 1843.

[31] Boivin L. P. 1993 Automated absolute and relative spectral linearity measurements on photovoltaic detectors, Metrologia 30 355-60.

[32] Fischer J. and Fu L. 1993 Photodiode nonlinearity measurement with an intensity stabilized laser as a radiation source, Appl. Opt. 32 4187-90.

[33] Kubarsepp T., Haapalinna A., Karha P. and Ikonen E. 1998 Nonlinearity measurements of silicon photodetectors, Appl. Opt. 37 2716-22.

[34] Budde W. 1983 Optical radiation measurements Physical Detectors of Optical Radiation vol 4 (New York: Academic) pp 247-61.

[35] I.A. Levitsky, W.B. Euler, Appl. Phys. Lett. 83 (9) (2003) 1857.

[36] M. Ambrosio et al, Nuclear Instruments and Methods in Physics Research A 617 (2010) 378-380.

[37] A. Ambrosio et al,Nuclear Instruments and Methods in Physics Research A 589 (2008) 398-403.

[38] M. Ambrosio et al, Nuclear Instruments and Methods in Physics Research A 610 (2009) 1-10.

[39] N.G. Tarr, D.L. Pulfrey and D.S. Camporese, An analytic model for the MIS tunnel junction, IEEE Trans. Electron Dev. 30 (2005) 1760.

[40] A. Tinti et al., Electrical analysis of carbon nanostructures/silicon heterojunctions designed for radiation detection, Nucl. Instrum. Meth. A 629 (2001) 377.

[41] T.F. Kuo, M.B. Tzolov, D.A. Straus and J. Xu, Electron transport characteristics of the carbon nanotubes/Si heterodimensional heterostructure, Appl. Phys. Lett. 92 (2008) 212107.

[42] M. Passacantando et al., Photoconductivity in defective carbon nanotube sheets under ultraviolet-visible-near infrared radiation, Appl. Phys. Lett. 93 (2008) 051911.

[43] J. W. Elam, D.A. Baker, A.B.F. Martinson, M. J. Pellin, J. T. Hupp, "Atomic layer deposition of indium tin oxide thin films using non halogenated precursors", J. Phys. Chem. C 2008, 112, 1938-1945.

[44] F. Kurdesau, G. Khripunov, A.F. da Cunha, M. Kaelin, A.N. Tiwari, "Comparative study of ITO layers deposited by DC and RF magnetron sputtering at room temperature", J. Non-Cryst. Solids, 352 (2006), 1466-1470.

[45] S. Lau , N. Kaiser, A. o ller, . Go tzelmann, H. Lauth, H. Bernitzki, "Room-temperature deposition of indium tin oxide thin films with plasma ion-assisted evaporation", Thin Solid Films 335 (1998) 1-5.

[46] H. Kim, C.M. Gilmore, A. Piquè, J.S. Horwitz, H. Mattoussi, H. Murata, Z.H. Kafafi, D.B. Chrisey, "Electrical, optical, and structural properties of indium-tin-oxide thin films for organic light-emitting devices", J. Appl. Phys., 86, 6451 (1999).

[47] A.R. Riben, D.L. Feucht, Int. J. Electron. 20 (1966) 583.

[48] R.J. Nemanich, M.J. Thompson, in: B.L. Sharma (Ed.), Metal Semiconductor Schottky Barrier Junctions and Their Applications, Plenum, New York, 1984.

[49] D. Donoval, M. Barus, M. Zdimal, Solid State Electron. 34 (1991) 1365.

[50] H. Matsuura, H. Okushi, in: J. Kanicki (Ed.), Amorphous and Microcrystalline Semiconductor Devices, Artech House, Boston, 1992.

[51] A.J. Harris, R.S. Walker, R. Sneddon, A.J. Harris, R.S. Walker, R. Sneddon, J. Appl. Phys. 51 (1980) 4287.

[52] P. Rosales-Quintero, A. Torres-Jacome, F.J. De la Hidalga-Wade, C. Zuniga-Islas, W. Calleja-Arriaga, C. Reyes-Betanzo, Superficies Vac. 21 (2008) 1.

[53] A.M. Mancini, P. Pierini, A. Valentini, L. Vasanelli, A. Quirini, Thin Solid Films 124 (1985) 85.

[54] P. Castrucci, M. Scarselli, M. De Crescenzi, M. A. El Khakani, F. Rosei, N. Braidy, and J. H. Yi, Appl. Phys. Lett. 85, 3857 (2004).

[55] D. A. Stewart and F. Léonard, Phys. Rev. Lett. 93, 107401 (2004).

[56] M. S. Fuhrer, J. Nygard, L. Shih, M. Forero, Y.-G. Yoon, M. S. C. Mazzoni, H. J. Choi, J. Ihm, M. Steven, G. Louie, A. Zettl, and P. L. McEuen, Science 288, 494 (2000).

[57] S. Lu and B. Panchapakesan, Nanotechnology 17, 1843 (2006).

[58] D. H. Lien, W. K. Hsu, H. W. Zan, N. H. Tai, and C. H. Tsai, Adv. Mater. (Weinheim, Ger.) 18, 98 (2006).

[59] C. A. Merchant and N. Markovic, Appl. Phys. Lett. 92, 243510 (2008).